First Principle Studies on Oxidation of Al_{13} Anion Cluster and Hydrogen Desorption from Hydrogenated Si(100) Surface

YUAN, Qinghong

A Thesis Submitted in Partial Fulfillment
of the Requirements for the Degree of
Doctor of Philosophy
in
Chemistry

The Chinese University of Hong Kong
October 2009

ProQuest LLC
789 East Eisenhower Parkway
P.O. Box 1346
Ann Arbor, MI 48106-1346

Thesis/Assessment Committee

Professor Steve C.F. Au-Yeung (Chair)
Professor Zhifeng Liu (Supervisor)
Professor Bo Zheng (Committee Member)
Professor Zhenyang Lin (External Examiner)
Professor Jinlong Yang (External Examiner)

論文評審委員會

歐陽植勳教授（主席）
劉志峰教授（论文导师）
郑波教授（委员）
林振陽教授（校外委员）
楊金龍教授（校外委员）

Abstract of thesis entitled:

First Principle Studies on Oxidation of Al_{13} Anion Cluster and Hydrogen Desorption from Hydrogenated Si(100) Surface

Submitted by Qinghong Yuan

for the Doctoral degree of Philosophy in Chemistry

at The Chinese University of Hong Kong in October 2009

Reactions on solid surfaces play a crucial role in many technologically important areas such as corrosion, adhesion, synthesis of new materials and heterogeneous catalysis. Theoretical studies on chemical reactions at surfaces can provide much useful information to understand and control these chemical processes. The present project is devoted to explore chemical reactions occurred on the aluminum cluster of Al_{13}^- and on the Si(100) surface by first principle calculations, using Gaussian 03 and Vienna Ab Initio Simulation Package (VASP).

Metal atom clusters are nanoscale intermediates between metal atoms and the bulk metal. Al_{13}^- can be regarded as a cluster model for Al(111) due to its special electronic and geometric structures. The reaction between Al_{13}^- and O_2 was explored by various DFT methods such as BLYP, PW91, PBE, B3LYP and BHHLYP and post-HF methods such as CCSD and QCISD(T). The calculation results demonstrated that the reaction was exothermic and thermodynamically quite favorable, and the reason for the stability of Al_{13}^- towards oxygen exposure was kinetic, due to the presence of a reaction barrier. True to the expectation of Al_{13}^- as a molecular model for the Al surface, the identification of this barrier resolved a long standing

puzzle in the initial chemisorption of O_2 on Al(111): a barrier was identified in experiment but not in any theoretical calculations on the ground state potential surface.

The Al_{13}^-+HX reactions, with HX being either HCl or HI, are explored by first principle calculations and two importance dynamic factors are identified. Firstly, there was a barrier to the dissociative adsorption of HX on the surface of an Al_{13}^- cluster, which involved charge transfer from Al_{13}^-. Secondly, the H atom could be bonded to the cluster in multiple ways, similar to the top, bridge and hollow adsorption sites on Al(111) surface. With a large amount of energy (>40 kcal/mol) deposited during the formation of $Al_{13}HX^-$, the H atom could easily migrate among these sites, similar to the diffusion of H on metal surfaces. The two dynamic factors were therefore important considerations in the formation and dissociation of $Al_{13}HX^-$. And moreover, these dynamic factors make Al_{13}^- a fascinating model to probe the dynamic aspect of surface reactions, which should be an important consideration in the reactivity of other metal clusters.

Hydrogen desorption mechanisms on hydrogenated silicon surface such as H/Si(100)-1×1, H/Si(100)-2×1 and H/Si(100)-3×1 surfaces have been explored by theoretical calculations with slab models. Similar desorption mechanisms have been identified for three hydrogenated surfaces and the calculated barriers were in agreement with experimental values. More interestingly, a common bridge structure has been identified as an intermediate. Its unique electronic structure is analyzed in detail. The identification of such a structure provides an alternative account for previous experimental results on STM tip-induced desorption.

香港中文大學

化學課程哲學博士學位

論文摘要

Al_{13} 金屬陰離子團簇氧化及氫化矽表面脫氫反應的理論研究

袁清红

二零零九年七月

固體表面發生的化學反應在許多科技領域有著非常重要的作用。例如腐蝕，粘附，新材料的合成以及異相催化都與固體表面的化學過程相關。對這類表面化學過程的理論研究能夠加深人們對表面化學反應的理解，從而更好的控制表面反應。本論文致力於運用第一性原理的計算，利用 Gaussian 03 和 VASP 等軟件，研究金屬團簇和半導體矽上的一些表面化學過程。

金屬團簇是介於金屬原子與大塊金屬之間的納米粒子。Al_{13}^-團簇有著非常特殊的電子和幾何結構，因而可被看作是 Al(111)表面的簇模型。運用密度泛函（如 BLYP, PW91, PBE, B3LYP 以及 BHHLYP）以及高精度的計算方法（如 CCSD，QCISD(T)）對 Al_{13}^-與 O_2 的化學反應進行考察，結果表明該反應在熱力學上是非常有利的。而 Al_{13}^-之所以對 O_2 表現出惰性是受動力學能壘的控制。這一能壘的確定解決了長期以來關於 O_2 在 Al(111)表面吸附時理論計算和實驗得出不一致結論的矛盾：實驗上觀測到 O_2 在 Al(111)表面的吸附存在一個能壘，但基於基態的理論計算卻沒有得到任何能壘。

对于 Al_{13}^-和鹵化氫 HX（X=Cl,I）的化學反應，我們的理論計算得出兩個非常重要的動力學因素。首先，HX 在 Al_{13}^-表面的化學吸附存在一個能壘，該能壘

的出現與反應過程中的電荷轉移相關。另外，與 H 在 Al(111)表面的化學吸附過程類似， H 原子也能在 Al_{13}^-金屬團簇表面的頂位，橋位以及穴位進行吸附。並且，由於吸附過程放出大量的熱（大約 40kcal/mol），反應生成的中間體產物 $Al_{13}HX^-$中的 H 原子可在不同的吸附位上發生熱移動，這與 H 在 Al(111)表面的擴散行為類似。吸附能壘以及 H 原子在 Al_{13}^-團簇上擴散這兩個動力學因素對於 Al_{13}^-+HX 反應中間體的生成以及解離有著非常大的影響。Al_{13}^-金屬團簇的這些動力學行為使得其成為一種非常有趣的表面模型，該模型上發生的化學熱力學及動力學過程可以類比到其他金屬表面。

運用週期性平板模型，我們也考察了氫氣在不同的氫化矽表面（如 3×1，2×1，1×1 表面）上的脫氫情況。結果表明氫氣在這三種表面上有著非常相似的脫附機理，並且計算得出的能壘與實驗吻合。尤為有趣的是，我們發現了氫氣在三種表面上脫附時需要經歷一個相同的中間體。這個中間體有著非常特殊的電子結構，可以解釋 STM 針尖電流激發導致的一些實驗現象，而這些實驗現象在此之前沒有一個非常合理的解釋。我們的計算提供了另外一個視角去解釋這種由 STM 針尖電場引起的激發。

ACKNOWLEDGEMENTS

I am deeply grateful to my supervisor Prof. Liu Zhifeng, Department of Chemistry in the Chinese University of Hong Kong (CUHK) for his kindly guidance and support in my research and in the writing of this thesis. During the past four years, Prof. Liu has given me a lot of chance to promote myself and spent much effort on my paper and thesis writing.

Special thanks are given to Prof. Sun Deyan(Physics Department, East China Normal University), Dr. Zheng Wenxu(South China Agricultural University), Dr. Wang Xin(Chemistry Department, Sichuan University), Dr. Ren Yi(Chemistry Department, Sichuan University), and Dr. Wang Kedong(Physics Department, The Chinese University of HongKong), for their help and discussion.

Thanks are also given to my colleagues in room 225A, Science Center, CUHK, Ms Chan Ka-wai, Mr Liu Jianwen, Ms Zhang Qiuju, Ms Zhanghan, Ms Liu Jing, Mr Chen Qiubo and Mr Ng Kwok Hung, for their friendship and discussion.

I have to thank the staffs from Department of Chemistry of CUHK, for their help. Special thanks are given to Mr. WOO Ka-Fai for his technical support and managing the High-Performance Calculation Cluster.

Finally, I would like to thank my family members, for their support and love.

TABLE OF CONTENTS

CHAPTER ONE

Research Background and Methodology

CHAPTER TWO

Theoretical study on Al_{13}^- + O_2 reaction and its comparison with the chemisorption of O_2 on Al(111)

CHAPTER THREE

Dynamic factors in the reactions between the magic cluster Al_{13}^- and HCl/HI

CHAPTER FOUR

New insights on hydrogen desorption dynamics from hydrogenated Si(100) surface

LIST OF FIGURES

LIST OF TABLES

Chapter One

Research Background and Methodology

1.1 Research Background

Solid surface chemistry has been played a crucial role in many technologically important areas such as corrosion, adhesion, synthesis of new materials, electrochemistry and heterogeneous catalysis[1-4]. Corrosion, which is caused by chemical reactions at surfaces, is a major problem in everyday life and damage caused by corrosion can be reduced by adjusting the composition of the surface[1]. Synthesis of new materials, especially the nanophase materials, is closely related with the property of the surface[2]. The development of electrochemistry is also influenced by surface chemistry, for example, the design of surfaces is a central research area in the field of electrochemical biosensors[3]. Heterogeneous catalysis plays a vital role in many industrial operations, such as the production of artificial fertilizers. And the reaction mechanism as well as the aging and poisoning of catalysts are all related to surface conditions[4]. The semiconductor industry is another area that depends on the knowledge of surface chemistry.

With the development of scanning tunneling microscope (STM), modern surface chemistry mainly focuses on the atomic level investigation of the phenomena and reaction processes occurred on the surface or interface[5-7]. It is well known that the nature of the solid surface is greatly different from that of the solid bulk. The reason is that the symmetry and crystal environment where the surface atoms experienced in bulk are suddenly destructed by the cutting. Thus a lot of special physical and chemical properties were introduced to the surface. Aluminum and silicon are the two common and important metal and semiconductor materials respectively. Studies on the two surfaces have been lasted for several decades and obtained a lot of achievements.

1.1.1 Al(111) surface and Al_{13}^- cluster

Aluminum is the most abundant metal element in the earth crust. It has numerous applications in the home and industry, and is a familiar metal to nearly everyone. Al(111) surface is the most simple metal surface. The electronic structure of Al(111) involves only sp bands, and its geometric structure, cut from a face-center-cubic lattice, is fairly simple, with little surface reconstruction. A lot of experimental and theoretical studies have been carried out on the adsorption of small molecules, such as O_2, H_2O, H_2, CH_3OH, CH_3I, NH_3 et al., on Al(111) surface[8]. In all these surface reactions, the interaction with oxygen has attracted a large amount of experimental[9] and theoretical work[10-14], due to its representation of a model system for the oxidation of metal surfaces.

1.1.1.1 Oxidation of Al(111) surface

It is known that aluminum surface is readily oxidized and a few atomic layers of surface oxide are effective in passivating the surface to avoid further oxidation, which explains the corrosion resistance of aluminum[15]. The oxide film is also chemically and thermally stable, and has already been engineered to form decorative and protective coatings on many consumable products.

Experimentally, X-ray photoelectron spectroscopy (XPS) and high resolution electron energy loss spectroscopy (HREELS)[16] showed the existence of the molecular chemisorption state. In addition, scanning tunneling microscopy (STM)[17-18] revealed the adsorption sites are mostly in fcc hollow sites. Molecular beam scattering identified the initial adsorption of oxygen as an activated process[8-9]. The initial sticking probability of O_2 on Al(111) is very low ($\sim 10^{-2}$) at low O_2 incident energy (0.024 eV). As the incident energy increases, so does the sticking probability, which reaches a constant value around 0.9 for incident energy above 0.6 eV. One simple explanation of this sticking behavior could have been the existence of an activation barrier of about 0.5eV for dissociation in the entrance channel. But unfortunately, such an explanation has found no theoretical support[10,19,20].

Theoretical calculations have so far failed in reproducing such a barrier, and there have been some suggestions that nonadiabatic processes provide the basic explanation for this failure[21-24].

One candidate is harpooning[25,26], where an electron tunneling from Al surface to $2p\pi^*$ orbital of O_2 could take place before O_2 hits the surface and the O_2-Al bonding interaction sets in. A more reactive O_2^- or even O_2^{2-}, which would then react with Al(111), can be produced,. This is similar to the harpooning model system of Cl_2 on K[24,27], where such an overlap effect as harpooning occurs relatively far from the surface[21-24]. The adiabatic electron affinity level of Cl_2 is actually 0.1 eV below the Fermi level of potassium, and the hole is there at infinite separation, while tunneling of an electron to this hole could take place when Cl_2 is 5–10 Å away from the surface[27]. In contrast, the O_2 electron affinity is much lower than Cl_2, and the work function of Al(111) is higher than K. When O_2 is 3.0 Å above Al(111), the $2p\pi^*$ peak of O_2 is close to but still above the Fermi level[11]. In other words, it is still not fully justifiable to talk about a hole state. This makes the harpooning mechanism impossible for O_2 /Al(111) system.

Another nonadiabatic possibility is a spin-flip process[28]. The ground state of the free O_2 molecule is a spin-triplet state with half-filled $2p\pi^*$ molecular-orbital resonance. Chemisorbed oxygen on aluminum is in a fully spin-compensated state, i.e., a spin-singlet state. Thus, the oxygen molecule experiences a triplet-to-singlet spin conversion along the reaction path. The important issues are how effective the triplet-to-singlet transition is and where it occurs. However, this simple idea as an explanation of the sticking behavior finds no theoretical support.

In this thesis, we prove that it is the self-interaction error (SIE) which caused by the deficiency of DFT functional that results in the failure. And details of the results are introduced in Chapter Two.

1.1.1.2 Al_{13}^- cluster and its reactivity

Al_{13}^- is a well-known magic cluster. It has a highly symmetric icosahedral structure, with one central atom and 12 equivalent Al atoms forming 20 equilateral triangle[29,30]. While the central Al atom is situated in a bonding environment similar to the cuboctahedral geometry in the bulk aluminium, each triangle resembles the surface structure of Al(111), making Al_{13}^- an interesting molecular model for both the Al bulk and the Al surface.(see Figure 1.1) The electronic structure of Al_{13}^- is also remarkable. With its nearly spherical geometry, the atomic cores in Al_{13}^-, including both the metal nuclei and inner shell electrons, produce a spherical jellium potential. The 40 valence electrons in Al_{13}^- can be filled as $1s^2 1p^6 1d^{10} 2s^2 1f^{14} 2p^6$, in shell closure, which makes it "magic" with remarkable stability[31,32].

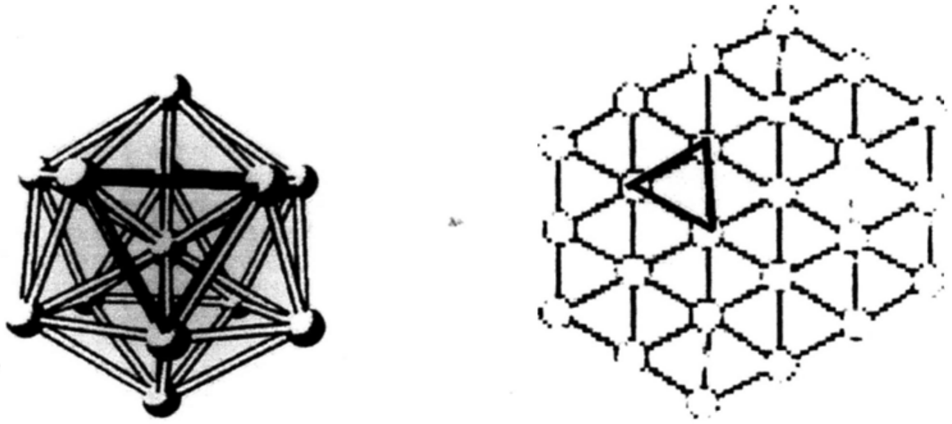

Al_{13}^- cluster **Al(111) surface**

Figure 1.1 Geometric structure of Al_{13}^- cluster and Al(111) surface.

The reactivity of Al_{13}^- is also unique due to its special geometric and electronic structure. Several typical reactions, such as Al_n^-+O_2, Al_{13}^-+Cl_2, Al_{13}^-+HCl and Al_n^-+HI will be reviewed in the following paragraphs.

The best known reaction was the interaction of O_2 with Al_n^-(n=3~40) clusters. When aluminium cluster anions Al_n^- are exposed to oxygen, cluster anions with an odd number of aluminium atoms react significantly slower with O_2 than those with an even number of aluminium atoms, while Al_{13}^- cluster displays "magic" features in the oxidation process[33,34]. The reason for this so called "odd/even" effect is attributed to the spin conservation rule[35]. Take Al_{13}^- and Al_{14}^- as an example, the spin multiplicity of the ground state of the Al_{13}^- cluster is a singlet, while the Al_{14}^- has a doublet ground state due to the unpaired electron. Since the ground state of oxygen is triplet, the initial adsorption adduct $[Al_{13}.O_2]^-$ is formed in triplet state and $[Al_{14}.O_2]^-$ is in a double state. Because Al_9^- and Al_2O, the final fragment for $[Al_{13}.O_2]^-$ (experimental results), are both singlets, there should be a spin-flip for $[Al_{13}.O_2]^-$, which may have a low probability in this case. In the case of Al_{14}^-, however, no such spin transition needs to occur since the initially formed $[Al_{14}.O_2]^-$ can react without spin restrictions to form the products Al_{10}^- and Al_2O via $Al_{14}O_2^-$. Although odd-numbered aluminum anion clusters react with triplet oxygen more slowly than even-numbered clusters due to the spin conservation rule, the particularly stable system Al_{13}^- reacts with oxygen even more slowly than other odd-numbered clusters. This is due to the "double magic" (icosahedral geometry and jellium-like electronic shell) character of Al_{13}^-. Therefore, both factors (barrier + spin flip) may be responsible for the slow reaction rate for Al_{13}^-.

In contrast to triplet oxygen, Cl_2 has a higher reactivity to Al_{13}^-. Upon exposing Al_{13}^- anions to a chlorine atmosphere, new signals, attributed mainly to Al_{11}^-, Al_9^-, and Al_7^- were observed after several tens of seconds[36]. These are due to the stepwise reaction sequence shown in Figure 1.2. In the first step, oxidation of the Al_{13}^- cluster surface proceeds to form the intermediate product $[Al_{13}Cl_2]^{-*}$. The large adsorption heats leads to vibrational and rotational excitation energy trapped in the $[Al_{13}Cl_2]^{-*}$ cluster that cannot be removed by collisions at pressures around 10^{-8} mbar. This, in turn, results in the fragmentation of $[Al_{13}Cl_2]^{-*}$ into $Al_{12}Cl^-$ and AlCl. In the next step, $Al_{12}Cl^{-*}$ is also fragmented, ejecting AlCl once again and leaving Al_{11}^-. In principle, the corresponding reactions of Al_{11}^- and Al_9^- are taking place in the same way. As presented in Figure 1.2, the reaction path for the interaction of Al_{13}^{-} cluster with chlorine, resulting in the release of AlCl as the main product, is a plausible mode for the corresponding reaction of bulk aluminium metal with chlorine.

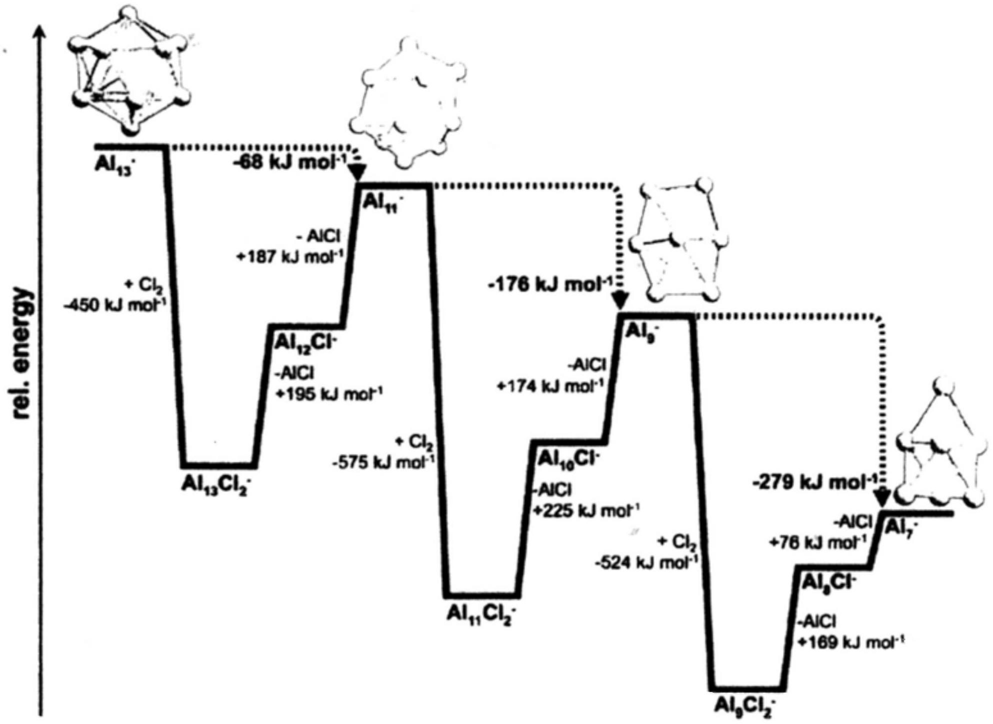

Figure 1.2 Schematic energy diagram for the cluster degradation; the energy values are given in kJ.mol^{-1}. In the first step, chlorine reacts with the surface of the Al_{13}^{-} cluster to form an $Al_{13}Cl_2^{-}$ cluster, which cannot be detected in the experiment because of its short lifetime. In the second step, the spontaneous fragmentation of $Al_{13}Cl_2^{-}$ leads to the release of AlCl and the formation of $Al_{12}Cl^{-}$*. Subsequent release of AlCl leads to Al_{11}^{-}. The degradations of Al_{11}^{-} and Al_{9}^{-} proceed in the same manner. Data copy from reference [36].

Being distinct from the interaction of Cl_2 with Al_{13}^{-}, Burgert R. et al. found that Al_{13}^{-} ions cluster did not react spontaneously with HCl[37]. However, when the kinetic energy of Al_{13}^{-} was increased by applying a radio frequency (RF) pulse, new signals, which were assigned as $Al_{12}H^{-}$, $Al_{12}Cl^{-}$, $Al_{11}H_2^{-}$, and Al_{11}^{-} (see mass spectrum in Figure 1.3), occurred. When only short RF pulses (~5 s) were applied, the formation of $Al_{12}H^-$ (see Figure 1.3(b)) was observed, whereas when slightly longer pulses (~15 s) were applied, Al_{11}^- also came clearly into view (see Figure 1.3(c)). When still more energy was supplied (through longer pulse lengths of up to 40 s), all of the reaction products appeared (see Figure 1.3(d)). The proposed reaction mechanism of Al_{13}^- plus HCl could therefore be subdivided into two branches (see scheme 1.1). The formation of an $[Al_{13}HCl^-]$ complex was postulated to be the first step during the reaction of Al_{13}^- with HCl. Because the exothermicity of the $[Al_{13}HCl^-]^*$ intermediate was so large, it was highly rotationally and vibrationally excited, and thus had a very short lifetime with respect to either dissociation back to the reactants or the dissociation to $Al_{12}H^-$+AlCl. Since the dissociation to $Al_{12}H^-$ and AlCl was calculated to be endothermic by +217 kJ mol^{-1}[37], this event proceeded only if additional energy was supplied, e.g., by RF excitation. If no additional energy was supplied, $[Al_{13}HCl^-]^*$ could only decompose back to the reactants, Al_{13}^- and HCl. This was the reason why Al_{13}^- ions appeared to be inert in an HCl atmosphere unless excitation was provided. However, our calculations demonstrate that it is the dynamic reasons that account for the inertion of Al_{13}^- in HCl atmosphere without RF. And we will give detailed explanations in chapter Three.

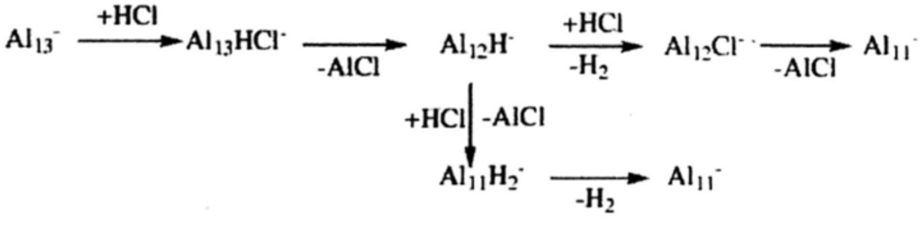

Schem 1.1 Reaction mechanism for Al_{13}^- + HCl.

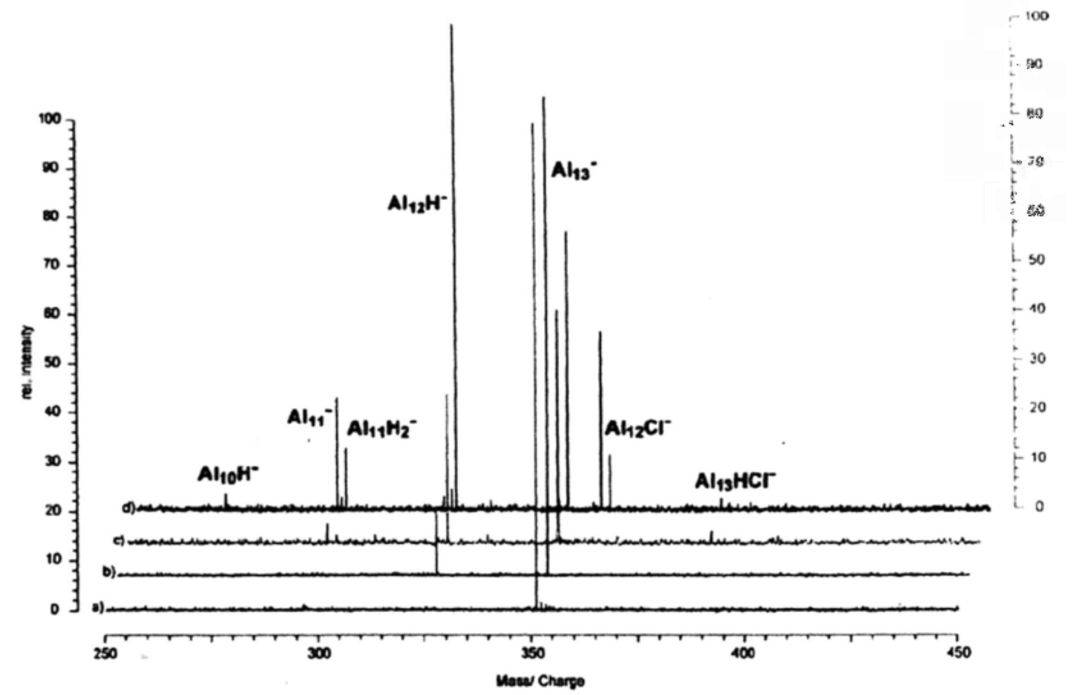

Figure 1.3 FT-ICR mass spectra for HCl reacting with Al_{13}^-. After laser desorption ionization of solid $LiAlH_4$, Al_n^- clusters are generated. Al_{13}^- is cooled via argon collisions, isolated, and exposed to an HCl atmosphere at ~10^{-8} mbar. (a) Without external energy supplied (RF excitation), no reaction is observed. (b) When a little energy is supplied (irradiation with RF pulse length ~5 s), $Al_{12}H^-$ is found as a reaction product. (c,d) For longer RF pulse lengths, all reaction products emerge. $Al_{13}HCl^-$ is observed only in very small amounts. Data copy from reference [37].

Reactivity of Al_{13}^- clusters with HI has also been explored[38,39]. When Al_n^- clusters is leaked to react with HI gas introduced through a flow-controlled reactant gas inlet, most of the clusters including Al_{13}^- were etched and the main product was $Al_{13}I^-$. This is surprising since no $Al_{13}Cl^-$ was identified in the Al_{13}^-+HCl reaction. Moreover, the $Al_{13}I^-$ was also regarded as a "magic" cluster, due to the special stability to oxygen exposure. The minimum energy structure calculated for $Al_{13}I^-$ shows that the ground state corresponds to an almost perfect icosahedral Al_{13}^-, with the iodine atom occupying the on-top site. Remarkably, the cluster's extra electron is localized on the Al_{13} cluster with an appreciable density at the vertex directly opposite from I atom. The reason is that the stability of the Al_{13}^- electronic shells means high electron affinity of neutral Al_{13} comparable to that of chlorine and fluorine atoms, and Al_{13}^- indeed behaves like a super-halide atom in bonding with iodine.

1.1.2 Hydrogenated silicon surface and hydrogen desorption

1.1.2.1 Si(100) surface and its reconstruction

Silicon crystals have the diamond structure, each silicon atom is sp^3 hybridized and bonded to four nearest neighbors in tetrahedral coordination. When the crystal is cut along (100) direction, each surface silicon atom has two single dangling bonds and the surface is not stable. The surface energy can be lowered by reducing the number of dangling bonds by rebonding, and this leads to a wide variety of surface reconstructions on silicon surfaces. These dangling bonds are the source of the surface chemical activity of silicon surface.

The commonly accepted model for the reconstructed Si(100) surface is the dimer model. The first model of this kind was proposed by Schlier and Farnsworth on the basis of their observation of a (2×1) LEED pattern[40]. In this model, the density of dangling bonds is decreased by 50% by creation of dimers, where each surface silicon atom bonds to a neighboring atom along the (100) direction using one of its dangling bonds, as shown in Figure 1.4. This original model was modified by Levine[41], and later by Chadi[42], who proposed that the dimers could be asymmetric.

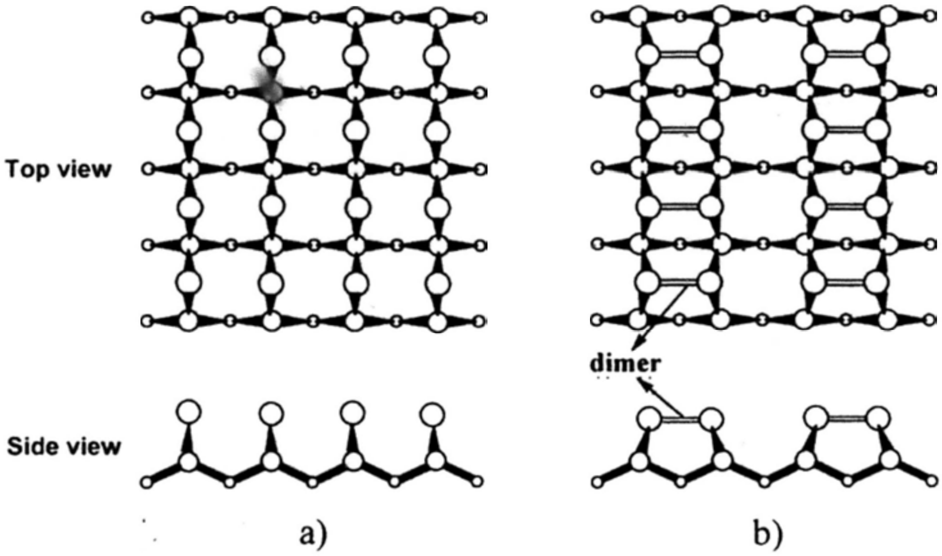

Figure 1.4 Top and side view of (a) non-reconstructed silicon surface and (b) reconstructed surface.

Depending on the relative ordering of the buckled dimers, different configurations are obtained. (2×1) structures are expected for symmetric dimers, which means that all dimers buckling in the same direction. However, the additional lattice strain introduced by dimer buckling caused the adjacent dimers in a row to buckle in opposite directions. If neighboring dimer rows buckle in the same direction, a local p(2×2) structure shown in Figure 1.5 a) is obtained, whereas a local c(4×2) structure(see Figure 1.5 b)) is obtained when neighboring dimer rows buckle in opposite directions. Recent calculations[43-46] have shown that the surface energy can be further lowered when the buckling orietation alternates along a row[44-46], and thus the c(4×2) structure was found to be the most favorable reconstructed surface.

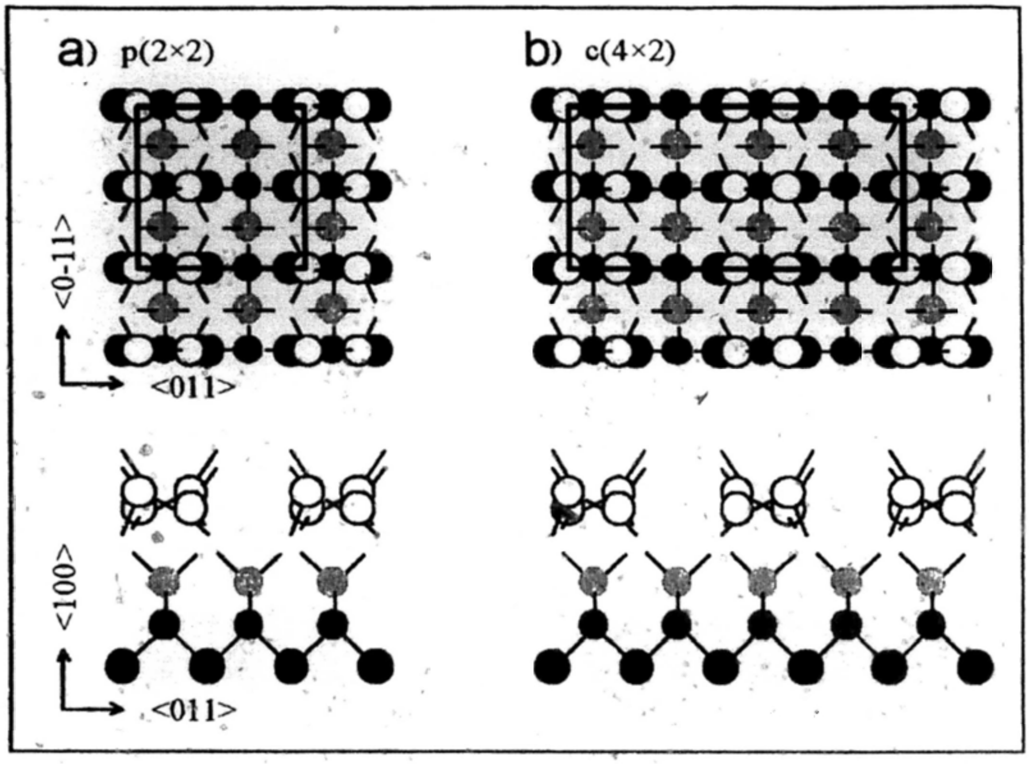

Figure 1.5 Top and side view of Si(100)- 2×1 surfaces with asymmetric Si-Si dimer. a) p(2×2) structure, b) c(4×2) structure.

1.1.2.2 Hydrogenated Si(100) surfaces and hydrogen desorption from H/Si(100) surfaces

With the addition of H atoms onto Si(100), the hydrogenated silicon surface (H/Si(100)) could be formed with a 2 × 1, 3 × 1, or 1 × 1 periodic structure (Figure 1.6). Adsorption of atomic hydrogen on the Si-Si dimer dangling bonds leads to the formation of the monohydride H/Si(100)-2×1 surface. Further H addition breaks the Si-Si dimer bond and each surface Si is bonded with two H atoms, forming a (1 × 1) dihydride surface. For a (3 × 1) phase, the structure is recognized to consist of alternating monohydride and dihydride species.

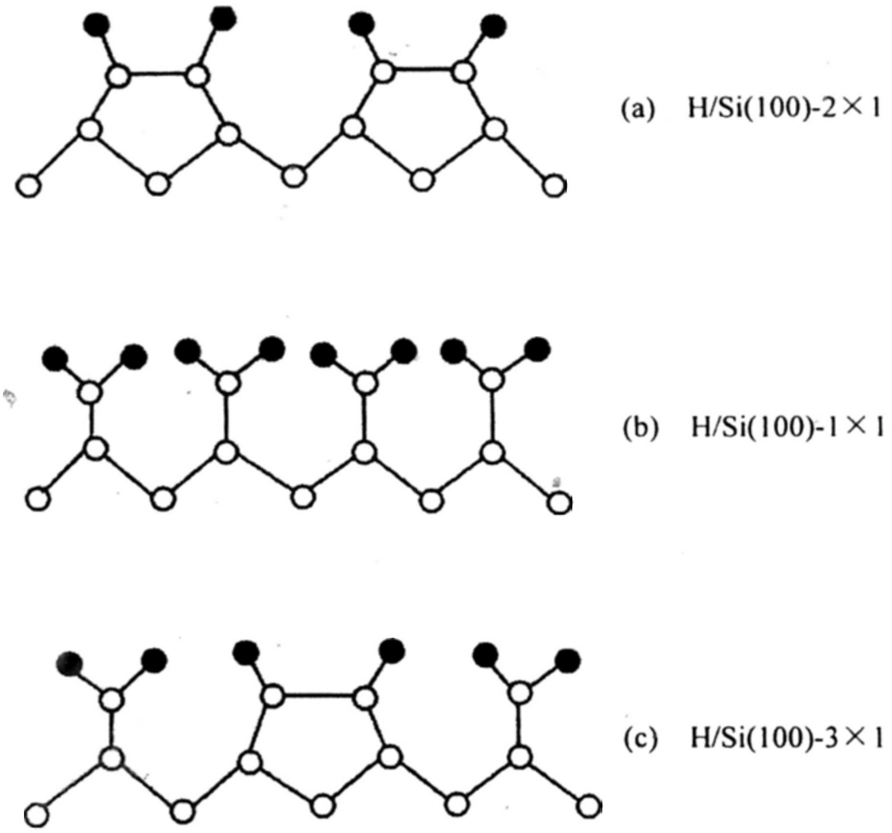

Figure 1.6 Schematic illustration of the structure of the ordered H/Si(100) surface phases: (a) H/Si(100)2×1. monohydride, (b) H/Si(100)1×1 dihydride, (c) H/Si(100)3×1- monohydride plus dihydride. The open circles denote Si atoms and solid circle represent H atoms.

Hydrogen desorption from the H/Si(100) surfaces, especially H/Si(100)-2×1 surface, has long been an active area of research[47-50]. On one hand, H/Si(100) surface is a fundamental model system to study adsorption and desorption on covalent surfaces. On the other hand, hydrogen desorption from H/Si(100) surface has its own characteristics. Firstly, hydrogen desorption from H/Si(100)-2×1 surface is first order reaction[52], which is in contrast to hydrogen desorption from metal surfaces where a second order desorption kinetics is determined. Secondly, a contradictory conclusion is drawn between adsorption and desorption kinetics. The very low sticking probability for H_2 adsorption on bare Si surfaces observed by experiment suggested an extremely large barrier for the adsorption process[51]. From traditional models of dynamics, one assumes that adsorption and desorption happen through the same pathway. Hence, if H_2 desorbs via a pathway with a substantial adsorption barrier, there should be an excess of energy in the desorbing molecule, as evidence that the desorbing H_2 came down off of a large adsorption barrier. However, REMPI measurements[54] of internal state distributions combined with time-of-flight measurements show that desorbing H_2 molecules do not possess any translational energy, demonstrating no large barrier is surmounted in the adsorption process, and this apparent violation of microscopic reversibility presents a "barrier puzzle"[53-55].

A lot of theoretical and experimental work have been carried out to reveal the veil of the desorption mechanism[56-59].

For hydrogen desorption from H/Si(100)- 2×1 surface, the most popular mechanisms are intra-dimer and inter-dimer mechanism. The firstly proposed mechanism is the intra-dimer mechanism, which involves the hydrogen desorption from the same Si-Si dimer.(see Figure 1.7 H4* and H2*) For a long time the intra-dimer desorption mechanism is the exclusive mechanism. It was favored because, first of all, with paired hydrogen atoms on one silicon dimer it led directly to the energetically lowest binding state. Secondly the paired state provides a straightforward explanation of the observed first-order desorption kinetics. Many calculations based on quantum chemical methods using small clusters have been carried out on intra-dimer desorption, unfortunately with significantly large desorption barrier[59,64]. But results from DFT slab-calculations using GGA exchange-correlation energy-functionals showed that activation energies are consistent with the experimental value[61-63]. There are also some experimental evidences that the desorbing molecules follow a reaction pathway via intra-dimer transition state. Combined with temperature-programmed desorption (TPD), the early STM experiment taken by Boland in 1991 indicated the intra-dimer desorbed silicon dimmer[60]. But the biggest challenge is the barrier puzzle[53-55].

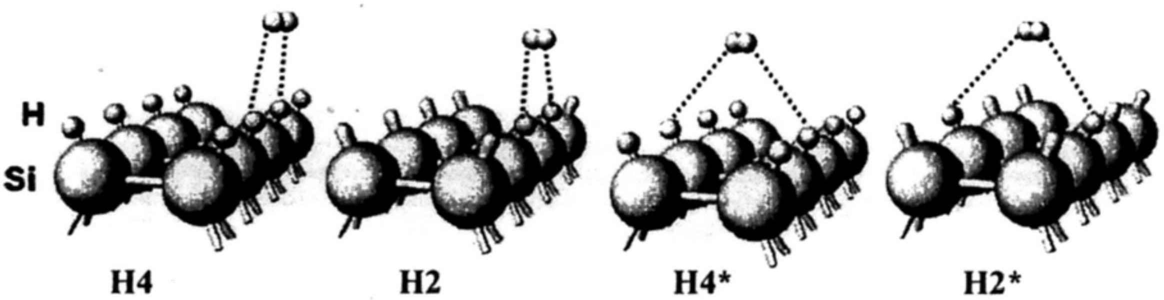

Figure 1.7 Sketch of desorption pathways for intra-dimer and inter-dimer mechanism. H4 represents inter-dimer desorption through where the two neighbor Si-Si dimers are covered with 4 H atoms. H2 represents inter-dimer desorption after the H4 desorption. H4* represents intra-dimer desorption through where the two neighbor Si-Si dimers are covered with 4 H atoms. H2* represents inter-dimer desorption after the H4* desorption.

The barrier puzzle was finally settled down in 2000's when Pehlke calculated the barrier for inter-dimer H4 and H2 desorption (see Figure 1.7 H4 and H2) and indicated that inter-dimer desorption is more favorable than that of intra-dimer desorption[64]. The main point of the inter-dimer mechanism is, at high coverage H_2 desorbed through H4 mechanism; at low coverage the H2 mechanism dominates.

The calculated PES for inter-dimer H4 desorption path indicated the inter-dimer desorption was more favorable than intra-dimer desorption, moreover, the PES for inter-dimer H4 desorption explained the translational cool desorbed H_2 very well due to the absence of desorption barrier. In addition, the calculated inter-dimer H2 PES revealed a desorption barrier, which supported the presence of H_2 adsorption barrier[57,65]. This is a big breakthrough in the H_2 desorption mechanism investigation.

There is also experimental evidence on the inter-dimer desorption mechanism. The combination of single-shot laser induced thermal desorption (LITD) with STM has been recently introduced to explore hydrogen desorption[66]. The very fast heating and subsequent cooling of the surface due to thermal energy deposition by means of a single nanosecond laser pulse allows to freeze-in the processes dominant at high temperature. The STM images taken directly after the adsorption process showed a clear predominance of two hydrogen atoms at two neighboring dimers, which confirmed the interdimer desorption pathway.

It has been suggested that several desorption mechanisms might have been active under the experimental conditions, and that desorption via steps or defects (both with a lower desorption energy barrier) might have contributed to the experimental yield[65].

The STM-tip induced hydrogen desorption is another type of desorption which has recently received a lot of attention[67,68]. It has been found that, using voltage pulses, bonds can be broken by STM-tip through generating strong electronic fields.

When the energy of the incident electrons in the STM tip exceeds the threshold of Si-H bond electronic excitation, which is about 6 eV, an single electron is excited from the bonding Si-H σ bonding to the corresponding antibonding σ* orbital and thus leading to local bond-breaking. Furthermore, the single dangling bonds induced by single dangling H atoms desorption have been shown by STM image. Substitution of H by D was found to produce a decrease of desorption yield by a factor of 50, which was shown to be caused by the existence of excitation-quenching channels and the mass difference of the atom on excited state.

When the energy of incoming electrons is below the threshold for electronic excitation, for example, 3 eV, and the current is sufficiently high, H desorption can still be observed in spite of the lower yield. The possible reason is multiple-vibrational excitation of the Si-H bond, which is due to the very high current density in the tunneling regime and the long Si-H vibrational lifetime. In addition, the isotope effect can be observed in the multiple-vibrational excitation, which was regarded to be caused by the vibrational lifetime. The vibrational lifetime of the Si-H stretch mode on Si(100) was very long but the vibrational frequency of the Si-D stretch was times lower. Therefore, the desorption rate for H was several times slower than that of D desorption.

1.2 Methodology

1.2.1 Schrödinger equation and Born-Oppenheimer approximation

Schrödinger equation, formulated by the Austrian physicist Erwin Schrödinger in

1926, is the basis for quantum chemistry. The first postulated Schrödinger equation is time-dependent[69]

$$-i\hbar\frac{\partial\Psi(x,t)}{\partial t}=\hat{\mathrm{H}}\Psi(x,t) \qquad (1.1)$$

where Ψ(x,t) is the wave function correlated with time and space, and $\hat{\mathrm{H}}$ is the Hamiltonian of the system:

$$\hat{\mathrm{H}}=-\frac{\hbar^2}{2m}\nabla_q^2+V(x,t) \qquad (1.2)$$

Here, the first term describe the kinetic energy of the electrons and nuclei, where the Laplacian operator Δ_q is defined as a sum of differential operators (in Cartesian coordinates)

$$\nabla_q^2=\frac{\partial^2}{\partial x_q^2}+\frac{\partial^2}{\partial y_q^2}+\frac{\partial^2}{\partial z_q^2} \qquad (1.3)$$

The second term in equation (1.2) defines the time-dependent potential part of the Hamiltonian. In most chemical systems, the potential energy is time-independent and the wave function can be separated into time and space parts

$$\Psi(x,t)=\psi(x)f(t) \qquad (1.4)$$

making the time-dependent Schrödinger equation to be simplified as

$$-i\hbar\psi(x)\frac{\partial f(t)}{\partial t}=-\frac{\hbar^2}{2m}f(t)\frac{\partial^2\psi(x)}{\partial x^2}+V(x)f(t)\psi(x) \qquad (1.5)$$

This equation can be finally simplified as time-independent Schrödinger equation[70,71]

$$\hat{\mathrm{H}}\Psi=E\,\Psi \qquad (1.6)$$

where the Hamiltonian $\hat{\mathrm{H}}$ is:

$$\hat{\mathrm{H}}=-\sum_{i=1}^{N}\frac{1}{2}\nabla_i^2-\sum_{A=1}^{M}\frac{1}{2M_A}\nabla_A^2-\sum_{i=1}^{N}\sum_{A=1}^{M}\frac{Z_A}{r_{iA}}+\sum_{i=1}^{N}\sum_{j>i}^{N}\frac{1}{r_{ij}}+\sum_{A=1}^{N}\sum_{B>A}^{M}\frac{Z_AZ_B}{R_{AB}} \qquad (1.7)$$

In which, M_A is the ratio of the mass of nucleus A to the mass of an electron, and Z_A is the atomic number of nucleus A. The first two terms describe the kinetic energy of the electrons and nuclei respectively; the remaining three terms define the potential part of the Hamiltonian and represent the attractive electrostatic interaction between the nuclei and the electrons, the repulsive potential due to the electron-electron and nucleus-nucleus interactions, respectively.

The time-independent Schrödinger equation (1.6) is widely used in quantum chemistry. In principle, the exact equation can be written for any system. But in practice, the exact solution is impossible for most systems and approximations are highly demanded. The most famous approximation is Born-Oppenheimer approximation. Since nuclei are much heavier than electrons, they move much slower than the electrons. Hence, to a good approximation, one can consider the electrons in a molecule to be moving in the field of fixed nuclei. Within this approximation, the second term of equation (1.7) can be neglected and the last term of equation (1.7) can be considered to be constant. Thus, the complete Hamiltonian given in equation (1.7) reduces to the so-called electronic Hamiltonian

$$\hat{\mathrm{H}}_{\mathrm{elec}} = -\sum_{i=1}^{N}\frac{1}{2}\nabla_i^2 - \sum_{i=1}^{N}\sum_{A=1}^{M}\frac{Z_A}{r_{iA}} + \sum_{i=1}^{N}\sum_{j>i}^{N}\frac{1}{r_{ij}} \qquad (1.8)$$

Until now, the central problem for quantum chemistry is to solve the Schrödinger equation involving the electronic Hamiltonian:

$$\hat{\mathrm{H}}_{\mathrm{elec}}\Psi_{\mathrm{elec}} = E_{\mathrm{elec}}\Psi_{\mathrm{elec}} \qquad (1.9)$$

The total energy, $E_{tot,}$ for the system is the sum of E_{elec} and the potential energy of the nuclei E_{nul}.

$$\mathrm{E}_{\mathrm{tot}} = \mathrm{E}_{\mathrm{elec}} + \mathrm{E}_{\mathrm{nul}} \qquad (1.10)$$

$$\mathrm{E}_{nul} = \sum_{\mathrm{A,B}} \frac{\mathrm{Z_A Z_B}}{|R_{\mathrm{A}} - R_{\mathrm{B}}|} \qquad (1.11)$$

The following problem is how to solve Schrödinger equation involving the electronic Hamiltonian.

1.2.2 Hartree-Fock (HF) approximation

To solve the equation (1.9), the electronic wave function Ψ_{elec} should be defined at first. It is impossible to search through all acceptable N-electron wave functions. We need to define a suitable subset, which offers a physically reasonable approximation to the exact wave function. The subset should be orthogonal, normalized and anti-symmetric according to Pauli principle. In the Hartree-Fock scheme the simplest, yet physically sound approximation is Slater determinants, Φ_{SD}.

$$\Psi_0 \approx \Phi_{SD} = \frac{1}{\sqrt{N!}} \begin{vmatrix} \chi_1(\vec{x}_1) & \chi_2(\vec{x}_1) & \cdots & \chi_N(\vec{x}_1) \\ \chi_1(\vec{x}_2) & \chi_2(\vec{x}_2) & \cdots & \chi_N(\vec{x}_2) \\ \cdots & \cdots & \cdots & \cdots \\ \chi_1(\vec{x}_N) & \chi_2(\vec{x}_N) & \cdots & \chi_N(\vec{x}_2) \end{vmatrix} \qquad (1.12)$$

$$= \frac{1}{\sqrt{N!}} \det\{\chi_1(\vec{x}_1)\chi_2(\vec{x}_2)\ldots\chi_N(\vec{x}_N)\}$$

Where the one-electron functions $\chi_i(\vec{x}_i)$ are called spin orbitals, and are composed of a spatial $\phi_i(\vec{r})$ and one of the two spin functions, α(s) or β(s).

Using the Slater determinant and variation principle, the best spin orbitals are those which minimize the electronic energy. By minimizing $\mathrm{E}_{\mathrm{elec}}$ with respect to the choice of spin orbitals, the HF energy is given by

$$E_{HF} = \left\langle \Phi_{SD} \middle| \hat{H} \middle| \Phi_{SD} \right\rangle = \sum_{i}^{N} (i\,|\,\hat{h}\,|\,i) + \frac{1}{2}\sum_{i}^{N}\sum_{j}^{N} (ii\,|\,jj) - (ij\,|\,ji) \qquad (1.13)$$

where

$$(i\,|\,\hat{h}\,|\,i) = \int \chi_i^*(\vec{x}_1)\left\{-\frac{1}{2}\nabla^2 - \sum_A^M \frac{Z_A}{r_{1A}}\right\}\chi_i(\vec{x}_1)d\vec{x}_1 \qquad (1.14)$$

defines the contribution due to the kinetic energy and the electron-nucleus attraction

and

$$(ii\,|\,jj) = \iint \left|\chi_i(\vec{x}_1)\right|^2 \frac{1}{r_{12}} \left|\chi_j(\vec{x}_2)\right|^2 d\vec{x}_1 d\vec{x}_2 \qquad (1.15)$$

$$(ij\,|\,ji) = \iint \chi_i(\vec{x}_1)\chi_j^*(\vec{x}_1)\frac{1}{r_{12}}\chi_i(\vec{x}_2)\chi_i(\vec{x}_2)d\vec{x}_1 d\vec{x}_2 \qquad (1.16)$$

are Coulomb and exchange intergrals, respectively, which represent the interaction between two electrons.

E_{HF} from equation (1.13) is a functional of the spin orbitals, $E_{HF} = E[\{\chi_i\}]$ and the HF derivation finally results into a set of one-electron Hartree-Fock equations

$$\hat{f}\chi_i = \varepsilon_i \chi_i, \ i=1,2,\ldots,N. \qquad (1.17)$$

in which the Fock operator $\hat{f}$ is an effective one-electron operator defined as

$$\hat{f}(\mathrm{i}) = -\frac{1}{2}\nabla_i^2 - \sum_A^M \frac{Z_A}{r_{iA}} + V_{HF}(i) \qquad (1.18)$$

$V_{HF}(i)$ is the Hartree-Fock potential. It is the average repulsive potential experienced by all electrons. So far, the complicated two-electron operator $1/r_{ij}$ in the Hamiltonian is replaced by the simple one-electron operator $V_{HF}(i)$ where the electron-electron repulsion is taken into account only in an average way. $V_{HF}(i)$ has the following two components:

$$V_{HF}(\mathrm{i}) = \sum_j^N \left(\hat{J}_j(\vec{x}_1) - \hat{K}_j(\vec{x}_1)\right) \qquad (1.19)$$

The coulomb operator $\hat{J}$, which represents the potential that an electron at position $\vec{x}_1$ experiences due to the average charge distribution of another electron in spin orbital

χ_j, is defined as:

$$\hat{J}_j(\vec{x}_1) = \int \left|\chi_j(\vec{x}_2)\right|^2 \frac{1}{r_{12}} d\vec{x}_2 \qquad (1.20)$$

The exchange operator $\hat{K}$ has no classical interpretation and can only be defined through its effect when operating on a spin orbital:

$$\hat{K}_j(\vec{x}_1)\chi_i(\vec{x}_1) = \int \chi_j^{*}(\vec{x}_2)\frac{1}{r_{12}}\chi_i(\vec{x}_2)d\vec{x}_2\chi_j(\vec{x}_1) \qquad (1.21)$$

In the case i=j, the coulomb operator, $\hat{J}$, describes the coulomb interaction of the charge distribution with itself. Such a self-interaction is physical nonsense. Actually, in HF approximation, the self-interaction problem is solved by the exchange operator, $\hat{K}$, when i=j, the coulomb term is equal to negative exchange term and thus canceled each other.

The essence of HF approximation is to transform the N-electron problem to 1-electron problem and treat the electron-electron repulsion in an average way[72,73]. As $V_{HF}(i)$ potential depends on the spin orbitals of the other electron, the HF equations (Equation (1.18)) should be solved by self-consistent-field (SCF) procedure. The solution of the this equations yields a set of orthogonal HF spin orbitals, $\{\chi_i\}$, with orbital energies $\{\varepsilon_i\}$. It should be noted that, the HF energy, E^{HF}, is not equal to the summation of all the occupied orbitals energies, $\sum_i \varepsilon_i$, instead of this,

$$E^{HF} = \sum_i \varepsilon_i - \frac{1}{2}\sum_{i,j}\int dx_1 \chi_i^{*}(x_1)[J_i(x_1) - K_i(x_1)]\chi_i(x_1) \qquad (1.22)$$

And the wave function is the Slater determinant formed by the occupied spin orbitals:

$$\Phi^{HF} = |\chi_i(x_1)\chi_j(x_2)...\chi_k(x_N)\rangle \qquad (1.23)$$

One of the limitations of HF calculations is that they do not include electron correlation. This means that HF takes into account the average effect of electron repulsion, but not the explicit electron-electron interaction. Within HF theory the probability of finding two electrons with different spin (electrons with same spin are forbidden due to the anti-symmetry of the Slater Determinant) at the same location is not zero. This is not physically true, but it is the consequence of the central field approximation, which defines the HF method.

The correlation energy, E_{corr}, is defined as the energy difference between the exact energy, ξ_0, and the Hartree-Fock limit, E_0^{HF},

$$E_{corr} = \xi_0 - E_0^{HF} \qquad (1.24)$$

An important part in ab initio computational chemistry is the calculation of the correlation energy, E_{corr}. All the methods aimed at improving E^{HF} are called the post-HF methods.

1.2.3 Post-HF approximation

The conceptually simplest way to obtain the correlation energy is by configuration intereaction (CI) calculations. The basic idea is to expand the exact wave function as a linear combination of N-electron trial functions (Slater determinant) and use the linear variational method. The sets of possible determinants include ground state $|\psi_0\rangle$, singly excited determinants $|\psi_a^r\rangle$ (which differs from $|\psi_0\rangle$ in having the spin orbital χ_a replaced by χ_r), doubly excited determinants $|\psi_{ab}^{rs}\rangle$, etc, up to and including N-excited determinants.

$$|\Phi_0\rangle = c_0|\psi_0\rangle + \sum_{ar} c_a^r |\psi_a^r\rangle + \sum_{\substack{a<b \\ r<s}} c_{ab}^{rs} |\psi_{ab}^{rs}\rangle + \sum_{\substack{a<b<c \\ r<s<t}} c_{abc}^{rst} |\psi_{abc}^{rst}\rangle + \ldots \qquad (1.25)$$

Configuration interaction calculations are classified by the number of excitations used to make each determinant. If only singly excited determinants are included, it is called a configuration interaction single-excitation (CIS) calculation. CIS calculations give an approximation to the excited states of the molecule, but do not change the ground-state energy. Single and double excitation (CISD) calculations yield a ground-state energy that has been corrected for correlation energy E_{corr}

$$E_{corr} = \sum_{\substack{a<b \\ r<s}} c_{ab}^{rs} \langle \psi_0 | H | \psi_{ab}^{rs} \rangle \qquad (1.26)$$

Triple-excitation (CISDT) and quadruple-excitation (CISDTQ) calculations are done only when very-high-accuracy results are desired. The configuration interaction calculation with all possible excitations is called a full CI. The full CI calculation using an infinitely large basis set will give an exact quantum mechanical result. However, full CI calculations are very rarely done due to the immense amount of computer power required.

Another way to get the correlation energy is to use Møller-Plesset perturbation theory, in which correlation is added as a perturbation from the Hartree-Fock wave function. In mapping the HF wave function onto a perturbation theory formulation, HF becomes a first-order perturbation. Thus, a minimal amount of correlation is added by using the second order MP2 method. Third-order (MP3) and fourth-order (MP4) calculations are also common. The accuracy of an MP4 calculation is roughly equivalent to the accuracy of a CISD calculation.

Coupled cluster calculations are similar to configuration interaction calculations in that the wave function is a linear combination of many determinants. There are various orders of the CC expansion, called CCSD, CCSDT, and so on. The accuracy of these two methods is very similar. The advantage of doing coupled cluster calculations is that it has no size consistency problem which is often appeared in CI calculations. Often, coupled-cluster results are a bit more accurate than the equivalent size configuration interaction calculation results. When all possible configurations are included, a full coupled-cluster calculation is equivalent to a full CI calculation.

There are some other post-HF methods, such as, Multi-Configurational Self-Consistent Field (MCSCF), Multi-Reference Configuration Interaction (MRCI) and Quantum Monte Carlo (QMC) methods, etc. Most of these calculations can give accurate calculation results but they are time-consuming.

1.2.4 Density functional theory (DFT) and self-interaction error (SIE)

Density functional theory (DFT) has been developed more recently than other ab initio methods. It becomes popular because it is less computationally intensive than other methods with similar accuracy. The basic concept of DFT is that the energy of a molecule can be determined from the electron density instead of a wave function. This modern DFT originated from the two famous Hohenberg-Kohn theorems proposed by Hohenberg and Kohn in 1964[74]. They proved that the ground state electronic energy is only a functional of ground state density ρ_0, which established the theoretical basis for DFT.

1.2.4.1 Kohn –Sham (KS) scheme

Although Hohenberg-Kohn theorem established the theoretical basis of DFT, a practical application of this theory was developed by Kohn and Sham who formulated a method similar in structure to the Hartree-Fock method[75]. They introduced the concept of a non-interacting reference system which has the same electron density with the real system. The ground state energy of the reference system can be written as

$$E_0 = \min_{\rho \to N}(T[\rho] + \int \rho(r) V_{Ne} dr) \qquad (1.27)$$

orbitals in the non-interacting reference system is named KS orbitals, $\left\{ \chi_i^{KS} \right\}$, determined by

$$-\frac{1}{2}\nabla^2 \chi_i^{KS} + V_S(\bar{r})\chi_i^{KS} = \varepsilon_i \chi_i^{KS} \qquad (1.28)$$

and the corresponding electron density is

$$\rho = \sum_i^N \left| \chi_i^{KS} \right|^2 \qquad (1.29)$$

kinetic energy is

$$T_s[\rho(r)] = -\frac{1}{2}\sum_i^N \langle \chi_i^{KS} \left| \nabla_i^2 \right| \chi_i^{KS} \rangle \qquad (1.30)$$

For a real interacting system, the ground state electronic energy can be written as

$$E_0 = \min_{\rho \to N}(F[\rho] + \int \rho(r) V_{Ne} dr) \qquad (1.31)$$

where

$$F[\rho(r)] = T[\rho(r)] + J[\rho(r)] + E_{ncl}[\rho(r)] \qquad (1.32)$$

Here, $T[\rho(r)]$ is the kinetic energy term, $J[\rho(r)]$ is the classical electrostatic electron-electron repulsion term and $E_{ncl}[\rho(r)]$ is the sum of other non-classical electrostatic interaction term. Because there is no way to accurately determine the true kinetic energy $T[\rho(r)]$ of the interacting system, Kohn and Sham suggested to use the exact kinetic energy $T_s[\rho(r)]$ of the non-interaction reference system with the same density as the real, interacting one $T[\rho(r)]$, while fitting the difference between $T_s[\rho(r)]$ and $T[\rho(r)]$ into exchange-correlation, E_{XC}, term. Then the real system energy can be re-written as

$$E[\rho] = T_S[\rho] + J[\rho] + E_{XC}[\rho] + \int V(r)\rho(r)dr \qquad (1.33)$$

in which E_{XC} is defined as

$$E_{XC}[\rho] = (T[\rho] - T_S[\rho]) + (E_{ee}[\rho] - J[\rho]) = T_C[\rho] + E_{ncl}[\rho] \qquad (1.34)$$

Two terms are included in E_{XC}, one is the correction term for kinetic energy, and the other term is the non-classical electrostatic contributions.

So far so good, but before we are in business with this concept we need to define V_S (r) that it exactly has the same density as our real system. Kohn and Sham proved that the reference system and real system had the same electron density if the $V_S(r)$ satisfied the following equation

$$V_S(r) \equiv V_{eff}(r) = \int \frac{\rho(r_2)}{r_{12}} dr_2 + V_{XC}(r_1) - \sum_A^M \frac{Z_A}{r_{1A}} \qquad (1.35)$$

in which V_{XC} is defined as

$$V_{XC} \equiv \frac{\delta E_{XC}}{\delta \rho} \qquad (1.36)$$

and

$$E_{XC} = \frac{1}{2} \iint \frac{\rho(r_1) h_{XC}(r_1; r_2)}{r_{12}} dr_1 dr_2 \qquad (1.37)$$

It is very important to realize that if the exact forms of E_{XC} and V_{XC} were known (which is unfortunately not the case), the Kohn-Sham strategy would lead to the exact energy. So the *Kohn-Sham* approach is in principle exact. This is different from the Hartree-Fock model, where the approximation is introduced right from the start (the wave function is assumed to be a single Slater determinant, which therefore can never deliver the true solution). The approximation only enters when we have to decide on an explicit form of the unknown functional for the exchange-correlation energy E_{XC} and the corresponding potential V_{XC}. The central goal of modern density functional theory is therefore to find better and better approximations to these two quantities. The currently developed schemes to approximate the exchange-correlation functional, $E_{XC}(\rho)$, are mainly three types: local density approximation (LDA), generalized gradient approximation (GGA), and hybrid functionals.

1.2.4.2 Local density approximation (LDA)

The simplest way to approximate the $E_{XC}(\rho)$ is local density approximation, which is based on the hypothesis of uniform electron gas[76]. The reason why the uniform electron gas has a prominent place in DFT is that it is the only system for which we know the form of the exchange and correlation energy functionals exactly. In this model, the $E_{XC}(\rho)$ can be written as:

$$E_{XC}^{LDA}[\rho] = \int \rho(r)\varepsilon_{XC}(\rho(r))dr \qquad (1.38)$$

Here, $\varepsilon_{XC}(\rho(r))$ is the exchange-correlation energy per article of a uniform electron gas of density $\rho(r)$. This energy per particle is weighted with the probability $\rho(r)$ that there is an electron at this position in space. The quantity $\varepsilon_{XC}(\rho(r))$ can be further split into exchange and correlation contributions,

$$\varepsilon_{XC}(\rho(r)) = \varepsilon_X(\rho(r)) + \varepsilon_C(\rho(r)) \qquad (1.39)$$

The exchange part, ε_X, which represents the exchange energy of an electron in a uniform electron gas of a particular density is , apart from the pre-factor, equal to the form found by Slater in his approximation of the Hartree-Fock exchange and was originally derived by Bloch and Dirac in the later 1920's[77]:

$$\varepsilon_X = -\frac{3}{4}\sqrt[3]{\frac{3\rho(r)}{\pi}} \qquad (1.40)$$

Inserting equation (1.40) into equation (1.38), we will get

$$E_X[\rho] \cong C_X \int \rho(\bar{r}_1)^{\frac{4}{3}} d\bar{r}_1 \qquad (1.41)$$

It can be seen that the exchange energy is only dependent on the electron density of position r, and thus the approximation is called local density approximation. For the correlation part, ε_C, the most widely used one is developed by Vosko, Wilk, and Nusair in 1980, while the most recent and probably also most accurate one has been given by Perdew and Wang in 1992. The currently popular LDA are SVWN and VWN5.

Actually, the electron density is not uniform and localized in real system. So the LDA can only give good geometry and vibration frequency but is not sufficient for energy calculation. So it is necessary to introduce the concept of gradient correction.

1.2.4.3 Generalized gradient approximation (GGA)

Functionals that include the gradients of the charge density are known as generalized gradient approximations (GGA). The E_{XC} in GGA can be written as

$$E_{XC}^{GGA}[\rho] = \int \rho(r)\varepsilon_{xc}[\rho(r)]dr + \int F_{XC}[\rho(r), \nabla\rho(r)]dr \qquad (1.42)$$

Similar to LDA, E_{XC}^{GGA} is usually split into its exchange and correlation contributions

$$E_{XC}^{GGA} = E_X^{GGA} + E_C^{GGA} \qquad (1.43)$$

The proposed exchange functionals are mainly divided into two types, the first one is developed by Becke in 1988 (abbreviated simply as B), the second class functionals are developed by Becke, 1986 (B86), Perdew, 1986 (P), and PBE. The correlation functionals are mainly P86, PW91, LYP, et. Al[78].

In principle, each exchange functional could be combined with any of the correlation functionals, but only a few combinations are currently in use. The currently used GGA are: PW91 exchange functional combined with PW91 correlation functional; B88 exchange functional together with LYP correlation functional.

1.2.4.4 Hybrid functionals

Although GGA made a large improvement on energy calculations, it is still not sufficient to get reliable thermodynamic data for a chemical reaction.

From equation (1.34), we can find the E_{XC} includes not only the no-classical electrostatic contribution but also the correction term for kinetic energy. Only the correction term for kinetic energy is incorporated into the coupling-strength integrated exchange-correlation hole h_{XC} can the E_{XC} become more accurate. Using the adiabatic connection, the h_{XC} which include correction term for kinetic energy can be defined as:

$$\bar{h}_{XC}(r_1;r_2) \equiv \int_0^1 h_{XC}^{\lambda}(r_1;r_2)d\lambda \qquad (1.44)$$

λ is the coupling strength parameter, for $\lambda = 0$, the system is a non-interacting reference system, while $\lambda = 1$ is for the real system. $0 < \lambda < 1$ is for system which has part interaction, and the corresponding E_{XC} is

$$E_{XC} = \int_0^1 E_{ncl}^{\lambda} d\lambda \qquad (1.45)$$

where E_{ncl}^{λ} corresponds to the pure potential energy contributions, dependent on λ. Equation (1.45) gave the true exchange-correlation energy and we know its value for $\lambda = 0$ exactly and have pretty good approximation for $\lambda = 1$. But the E_{ncl}^{λ} for intermediate value of λ is not available and we must try to find approximations to this integral λ. The simplest approximation to solve equation (1.45) is to assume that E_{ncl}^{λ} is a linear function in , which leads to

$$E_{XC}^{HH} = \frac{1}{2} E_{XC}^{\lambda=0} + \frac{1}{2} E_{XC}^{\lambda=1} \qquad (1.46)$$

This is the so-called half-and-half (HH) scheme, which represents combination of 'exact' exchange and density functional exchange-correlation as introduced by Becke in 1993a[79]. This approach showed a promising performance. To further improve the E_{XC}, the next step taken by Becke, 1993b was to introduce semi-empirical coefficients to determine the weights of the various components in this scheme leading to the following extension of equation

$$E_{XC}^{B3} = E_{XC}^{LSD} + a(E_{XC}^{\lambda=0} - E_{X}^{LSD}) + b\Delta E_{X}^{B88} + c\Delta E_{C}^{PW91} \qquad (1.47)$$

This is the important three-parameter fit Becke scheme, and in which a=0.20, b=0.72, c=0.81[80]. Currently, the most popular hybrid functionals is known as B3LYP and was suggested by Stephens et al., 1994[81]. In B3LYP, the PW91 correlation functional is replaced by the LYP functional. The values of the three parameters were directly taken from Becke's original paper. Thus the B3LYP exchange-correlation energy expression is

$$E_{XC}^{B3LYP} = (1-a)E_{X}^{LSD} + aE_{XC}^{\lambda=0} + b\Delta E_{X}^{B88} + cE_{C}^{LYP} + (1-c)E_{C}^{LSD} \qquad (1.48)$$

The unsigned error for B3LYP functional with respect to the G2 data base of only slightly above 2 kcal/mol was determined.

Recently, some other hybrid functionals, such as B98[82]、PBE0[83]、KMLYP[84] and X3LYP[85] had also been developed. But B3LYP is still the most popular fuctional.

1.2.4.5 Self-interaction error (SIE)

Although DFT has high computational accuracy and efficiency, it has its own limitation. One of the limitations is self-interaction error. For the case of one electron system, the energy expression in Kohn-Sham scheme is

$$E[\rho(\vec{r})] = T_S[\rho] + J[\rho] + E_{XC}[\rho] + E_{Ne}[\rho] \qquad (1.49)$$

The classical electrostatic repulsion term is

$$J[\rho] = \frac{1}{2}\iint \frac{\rho(\vec{r}_1)\rho(\vec{r}_2)}{r_{12}} d\vec{r}_1 d\vec{r}_2 \qquad (1.50)$$

For a system with one electron or less, there is no electron-electron interaction and the sum of classical electrostatic repulsion term J[ρ] and exchange-correlation term Exc[ρ] should be zero.

$$\frac{1}{2}\iint \frac{\rho(\vec{r}_1)\rho(\vec{r}_2)}{r_{12}} d\vec{r}_1 d\vec{r}_2 = -E_{XC}[\rho] \qquad (1.51)$$

We saw in equation (1.13) that by constructing the exchange term of the Hartree-Fock model indeed exactly neutralizes the unwanted portion of J[ρ]. For a one electron system equation (1.51) is satisfied and the HF scheme is therefore free of self-interaction errors. But for any realization of the Kohn-Sham density functional scheme we have to employ approximations to the exchange-correlation energy which are independent of J[ρ] and we should not expect equation (1.51) to hold. In fact, none of the currently used exchange-correlation functionals is self-interaction free and the self-interaction error is equals to $J[\rho]+E_{XC}[\rho]$.

The self-interaction plays a decisive role for some special chemical reactions, especially for dissociative behavior of some symmetric radicals, and reaction barrier for some charge-transfer reactions.

Previous studies demonstrated that the SIE error in DFT calculation is correlated with the fraction of Hartree-Fock(HF) exchange functional. Larger fraction of HF exchange functional will result in smaller SIE[86].

1.2.5 DFT based ab initio molecular dynamics (AIMD)

1.2.5.1 Car-Parrinello molecular dynamics

The genesis of the application of DFT in molecular dynamics was proposed by Car & Parrinello in 1985[87]. The basic idea of the Car-Parrinello approach is to compute the forces acting on the nuclei from electronic structure calculations that are performed "on-the-fly" as the molecular dynamics trajectory is generated. Through this approach, both the electronic structure problem and the dynamics of the atoms were solved concurrently by a set of Newton's equations. Compared with traditional approach, this theoretical breakthrough allows calculations of the fully dynamic time evolution of a structure (molecular dynamics) without resorting to a predefined potential energy surface which is used in classical molecular dynamics.

Treating the coefficients of the basis functions as dynamical variables, Car & Parrinello postulated a classical Lagrangian for the system

$$L = \sum_i \frac{1}{2}\mu \int_\Omega d^3r \left|\dot{\psi}_i(r)\right|^2 + \sum_I \frac{1}{2} M_I \dot{R}_I^{\,2} + \sum_\nu \frac{1}{2}\mu_\nu \dot{\alpha}_\nu^{\,2} - E[\{\psi_i\},\{R_I\},\{\alpha_\nu\}] \qquad (1.52)$$

$$E[\{\psi_i\},\{R_I\},\{\alpha_\nu\}]=\sum_i\int_\Omega d^3r\psi_i^*(r)[-(\frac{\hbar^2}{2m})\nabla^2]\psi_i(r)+U[n(r),\{R_I\},\{\alpha_\nu\}] \qquad (1.53)$$

Here $\{R_I\}$ indicate the nuclear coordinates and $\{\alpha_\nu\}$ are all the possible external constraints imposed on the system. The functional U contains the internuclear Coulomb repulsion and the effective electronic potential energy. And $\psi_i(r)$ are subject to the holonomic constraints:

$$\int_\Omega d^3r\psi_i^*(r,t)\psi_j(r,t)=\delta_{ij} \qquad (1.54)$$

In equation (1.52), a dot denotes the time derivative, M_I are the physical ionic masses, and μ and μ_ν are arbitrary parameters of appropriate units.

The Lagrangean in equation (1.52), will generate a dynamics for the parameters $\psi_i(r)$'s, $\{R_I\}$'s and $\{\alpha_\nu\}$'s through the equations of motion:

$$\mu\ddot{\psi}_i(r,t)=-\frac{\delta E}{\delta\psi_i^*(r,t)}+\sum_k\Lambda_{ik}\psi_k(r,t) \qquad (1.55a)$$

$$M_I\ddot{R}_I=-\frac{\partial E}{\partial R_I}+\sum_{ij}\Lambda_{ij}\frac{\partial}{\partial R_I}\langle\psi_i|\psi_j\rangle \qquad (1. 55b)$$

$$\mu_\nu\ddot{\alpha}_\nu=-\frac{\partial E}{\partial\alpha_\nu} \qquad (1. 55c)$$

where Λ_{ik} are Lagrange multipliers introduced for satisfying the constraints in equation (1.54). Here, the so-called "dynamical simulated annealing" was performed, presented by the dynamics associated with the $\psi_i(r)$'s and the $\{\alpha_\nu\}$'s. Equation (1.52) defines a potential energy E and a classical kinetic energy K given by

$$K=\sum_i\frac{1}{2}\mu\int_\Omega d^3r|\dot{\psi}_i|^2+\sum_I\frac{1}{2}M_I\dot{R}_I^2+\sum_\nu\frac{1}{2}\mu_\nu\dot{\alpha}_\nu^2 \qquad (1.56)$$

The equilibrium value <K> of the classical kinetic energy can be calculated as the temporal average over the trajectories produced by the equation of motion (equation (1.55)) and related to the temperature of the system by suitable normalization. By variation of the velocities, i.e. the $\psi_i(r)$'s, $\{R_I\}$'s and $\{\alpha_\nu\}$'s, the temperature of the system can be slowly reduced and for T→0 the equilibrium state of minimal E is reached.

1.2.5.2 Plane wave basis set

For an extended (or even infinite) system, such as bulk solid, the calculation of the one-electron wave functions is a formidable task. One possible solution in the solid-state theory is to assume the system of interest can be represented by a box of atoms which is repeated periodically in all three special directions. The periodic lattice produces a periodic potential and imposes the same periodicity on the density. Therefore, the basis set for this particular system is represented by plane wave basis set, which is different from Slater or Gaussian basis set.

The Bloch's theorem[87] states that in a periodic solid each electronic wave function can be written as the product of a periodic function and a plane wave with wave vector k[88,89]:

$$\psi_i(r,k) = e^{ikr}\mu_i(r,k) \qquad (1.57)$$

the periodic function has the periodicity of the direct lattice $\mu_i(r,k) = \mu_i(r+T,k)$ and can be written as

$$\mu_i(r,k) = \frac{1}{\sqrt{\Omega}}\sum_G c_i(G,k)e^{iGr} \qquad (1.58)$$

where the reciprocal lattice vectors G are defined by G.T=2πm for all lattice vectors T with m is being an integer number, Ω is the volume of the cell. Therefore, each electronic wave function can be written as a sum of plane waves,

$$\psi_i(r,k) = \frac{1}{\sqrt{\Omega}} \sum_G c_i(G,k) e^{i(K+G)r} \qquad (1.59)$$

Substituting the above expression of wave function to single electron Kohn-Sham equation,

$$\left\{ -\frac{\hbar^2}{2m}\Delta + V_{ext}(r) + V_H\left[n(r)\right] + V_{XC}\left[n(r)\right] \right\} \psi_{kj}(r) = \varepsilon_{kj}\psi_{kj}(r) \qquad (1.60)$$

we can get the matrix eigenvalue equation

$$\sum_{G'} \left[\frac{\hbar^2}{2m} \|k+G\|^2 \delta_{G'G} + V_{ext}(G-G') + V_H\left[G-G'\right] + V_{XC}\left[G-G'\right] \right] c_{i,k+G'} = \varepsilon_i c_{i,k+G'} \quad (1.61)$$

In practical calculations the wave functions is truncated by keeping only those plane wave vectors (k+G) with a kinetic energy lower than a given cutoff value E_{pw}

$$\frac{\hbar^2}{2m} \|k+G\|^2 \le E_{cut} \qquad (1.62)$$

Solution of the equation [1.61] proceeds by diagonalization of a Hamiltonian matrix, the size of which are determined by the choice of E_{cut} of plane-wave basis set and will be intractable large for systems that contain both valence and core electrons. To minimize the size of the plane wave basis set necessary for the calculation, the pseudopotential approximation is introduced.

1.2.5.3 Pseudopotential (PP)

The pseudopotential approximation[90,91] is based on the fact that most physical properties of solids are dependent on the valence electrons to a much greater degree than that of the tightly bound core electrons. It was possible to remove the core electrons and replace the true nuclear potential $v_{ion}(r)$ created by the core electrons and the nuclei by a weaker pseudopotential $v_{ion}^{PS}(r)$, as shown in Figure 1.8. Such pseudopotential $v_{ion}^{PS}(r)$ acts on a set of pseudo wavefunctions $\psi_{ion}^{PS}(r)$ rather than the true valence wavefunctions. The corresponding set of pseudo-wavefunctions $\psi_{ion}^{PS}(r)$ and the all-electron wavefunctions $\psi^{AE}(r)$ are identical outside a chosen cutoff radius r_c and the charge enclosed within r_c must be equal for the two wavefunctions

$$\int_0^r \left|\psi^{PS}(r)\right|^2 dr = \int_0^r \left|\psi^{AE}(r)\right|^2 dr \qquad (1.63)$$

Also the two wavefunctions are normalized

$$\int_0^\infty \left|\psi^{PS}(r)\right|^2 dr = \int_0^\infty \left|\psi^{AE}(r)\right|^2 dr = 1 \qquad (1.64)$$

This is commonly referred to as norm-conservation.

The $\psi_{ion}^{PS}(r)$ does not possess the nodal structure that causes the oscillations inside the core region and hence can be described with a reasonable number of plane-waves. In addition, the valence all-electron and pseudopotential have the same eigenvalues.

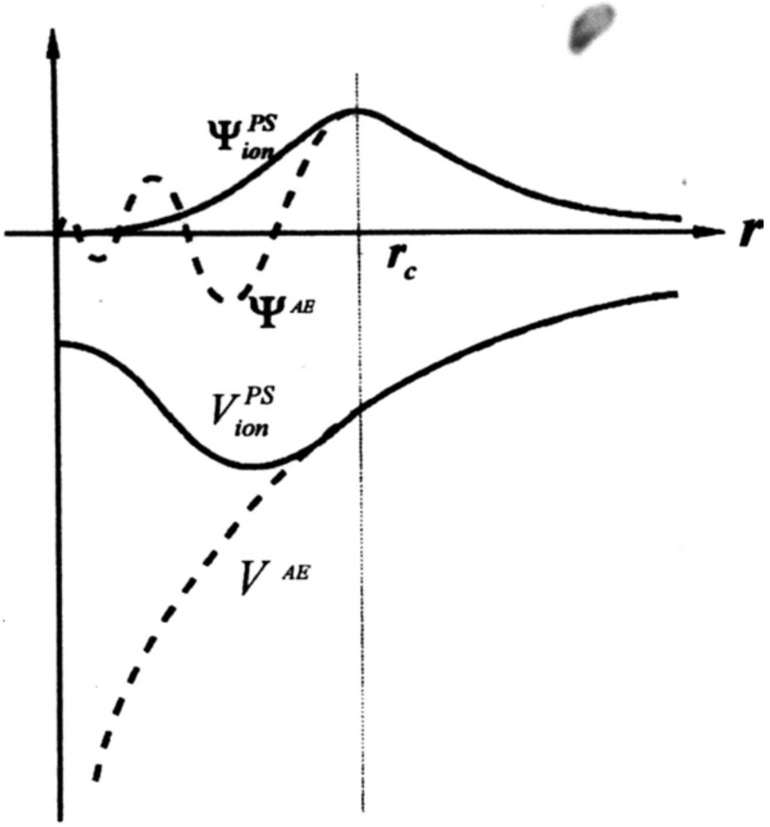

Figure 1.8 Comparison of a wavefunction in the coulomb potential of the nuclei (blue) to the one in the pseudopotential (red). The real and the pseudo wavefunction and potentials match above a certain cutoff radius r_c.

Two commonly used pseudopotentials are Vanderbilt's Ultra-Soft pseudopotential (US-PP) and Projector Augmented Wave potential (PAW).

Ultra-soft Pseudopotentials (US-PP)

US-PP was proposed by Vanderbilt in the early 1990s[92]. As the name suggests, it attains much smoother (softer) pseudo-wavefunctions and using considerably fewer plane-waves for calculations of the same accuracy. This is achieved by relaxing the norm-conservation constraint shown in equation (1.64). In this scheme the total valence density n(r) is partitioned into two parts:

ultrasoft valence wave function that do not fulfill the norm conservation criteria,

$\phi_i^{PS}(r)$, plus a core augmentation charge

$$Q_{ij}(r) = \psi_i^{AE*}(r)\psi_j^{AE}(r) - \phi_i^{PS*}(r)\phi_j^{PS}(r) \qquad (1.65)$$

The ultrasoft pseudopotential takes the form:

$$V^{PS} = V_{loc}(r) + \sum_{ijl} D_{ij}^{0} \left|\beta_i^l\right\rangle\left\langle\beta_j^l\right| \qquad (1.66)$$

the β projector functions are defined through

$$\left|\beta_j\right\rangle = \sum_i \frac{\left|\chi_i\right\rangle}{\left\langle\chi_i\middle|\phi_j\right\rangle} \qquad (1.67)$$

are strictly localized inside the cut-off region for the wave functions since the χ-functions are defined through

$$\left|\chi_i\right\rangle = (\varepsilon_i - \hat{T} - V_{loc})\left|\phi_i\right\rangle \qquad (1.68)$$

And D is defined by

$$D_{ij}^{0} = \left\langle\phi_j\middle|\chi_m\right\rangle + \varepsilon_i q_{ij} \qquad (1.69)$$

The overlap operator S:

$$\hat{S} = 1 + \sum_{ijl} q_{ij} \left|\beta_j^l\right\rangle\left\langle\beta_i^l\right| \qquad (1.70)$$

with $q_{ij} = \int_0^r Q_{ij}(r)dr$. The charge density is thus defined through

$$n(r) = \sum_n \left[\left|\phi_n(r)\right|^2 + \sum_{ijl} Q_{ij}^l(r) \left\langle\phi_n\middle|\beta_j^l\right\rangle\left\langle\beta_i^l\middle|\phi_n\right\rangle \right] \qquad (1.71)$$

The Kohn-Sham equation takes the form

$$H\left|\psi_i^{PS}\right\rangle = \varepsilon_i \hat{S}\left|\psi_i^{PS}\right\rangle \qquad (1.72)$$

Where

$$H = -\nabla^2 + V_{eff} + \sum_{ij,l} D_{ij}^l \left|\beta_j^l\right\rangle \left\langle \beta_i^l \right| \qquad (1.73)$$

And the D-function needs to be updated during the self consistent calculation according to

$$D_{ij}^l = D_{ij}^0 + \int V_{eff}(r) Q_{ij}^l dr \qquad (1.74)$$

In this scheme, the pseudo-wavefunctions are as soft as possible within the core region, which makes it possible for a drastic reduction in the cut-off kinetic energy. The material properties of complex ionic systems consisting of many different kinds of atoms are well reproduced by calculations using USPP[93].

Projector augmented wave (PAW) method

The PAW potential was introduced by Blöchl in 1994[94,95]. The basic idea of this method is to divide the wave function into three parts: atomic-like partial waves, $\{\phi_i\}$, auxiliary partial waves, $\{\tilde{\phi}_i\}$, expanded within atomic sphere regions, and auxiliary wave function, $\{\tilde{\psi}_i\}$, expanded outside the spheres (**Figure 1.9**).

$$|\psi\rangle = |\tilde{\psi}\rangle + \sum_i (|\phi_i\rangle - |\tilde{\phi}_i\rangle)\langle p_i|\tilde{\psi}\rangle \qquad (1.75)$$

The atomic-like partial waves, $\{\phi_i\}$, are pre-determined and are the solutions of the Schrödinger equations for the isolated atoms and describe correctly the nodal structure of the wave function near the nucleus. The projectoperators, p_i, are chosen such that within the atomic sphere region:

$$|\tilde{\psi}\rangle = \sum_i |\tilde{\phi}_i\rangle \langle p_i|\tilde{\psi}\rangle \qquad (1.76)$$

with $\left\langle p_i \middle| \tilde{\phi}_j \right\rangle = \delta_{ij}$.

The heart of PAW method is to transform the true wave function, $\{\psi_i\}$, with nodal structure to auxiliary wave functions, $\{\tilde{\psi}_i\}$, which are smooth and can be expanded into plane waves. Equation 1.75 can be written as

$$|\psi\rangle = T|\tilde{\psi}\rangle \qquad (1.77)$$

with linear transformation operator defined as

$$T = 1 + \sum_i (|\phi_i\rangle - |\tilde{\phi}_i\rangle)\langle p_i| \qquad (1.78)$$

The ground state energy functional, E, and other expectation values can be expressed by auxiliary wave functions, $\{\tilde{\psi}_i\}$

$$E = E[\psi_n] = E[\tilde{\psi}_n] \qquad (1.79)$$

Therefore, instead of minimization of energy with respects to the wave functions, $\{\psi_i\}$, to obtain the KS equations, the minimization of energy is get by variation of the auxiliary wave functions, $\{\tilde{\psi}_i\}$, which is computationallydemanding less.

Unlike USPP approaches, PAW method avoids the introduction of PP for the core electrons. The core electrons are decomposed in the same way as the valence electrons without the projector operators, p$_i$, and are not varied during calculation. Therefore, PAW method is an all-electron method and works with frozen-core approximation directly.

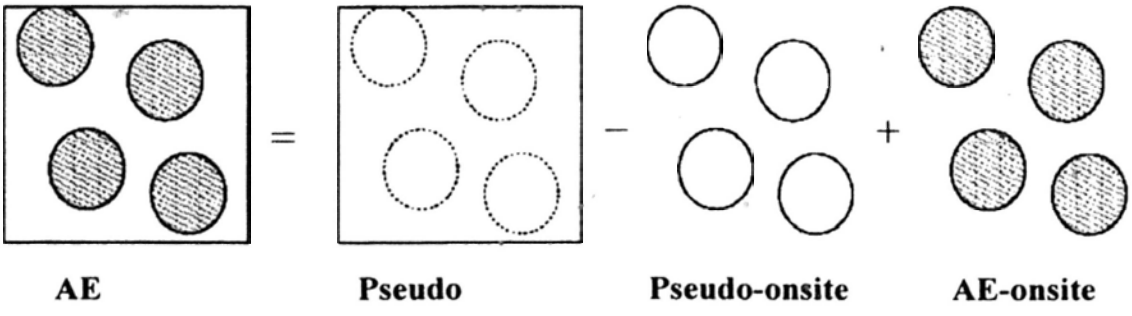

Figure 1.9 Decomposition of wave function in PAW method.

1.2.6 Transition state locating

A transition structure is mathematically defined as the geometry that has a zero derivative of energy with respect to moving every one of the nuclei and has a positive second derivative of energy for all but one geometric movement, which means that in one direction in nuclear configuration space the energy has a maximum, while in all other (orthogonal) directions the energy is a minimum. The energy of this species is needed in order to determine the energy barrier to reaction and thus the reaction rate. The geometry of a transition structure is also an important piece of information for describing the reaction mechanism.

There are a lot of techniques to search transition states and here we give only two of them which were used in our calculations.

Optimization based on initial guess

In *Gaussian* calculations one of the most popular techniques to search transition state is based on initial guess. The optimization algorithm included in *Gaussian* is the "Berny algorithm" developed by H. Bernhard Schlegel[97]. For searching transition state, this algorithm uses the forces acting on the atoms of a given structure together with the second derivative matrix (called the Hessian matrix) to predict structure with higher energy and thus optimize the molecular structure towards the maximum on the potential energy surface. As explicit calculation of the second derivative matrix is quite costly, the Berny algorithm constructs an approximate Hessian at the beginning of the optimization procedure through application of a simple valence force field, and then uses the energies and first derivatives calculated along the optimization pathway to update this approximate Hessian matrix. The success of the optimization procedure therefore depends to some degree on how well the approximate Hessian represents the true situation at a given point. Thus, the optimization will only be able to find the correct geometry if the starting geometry is sufficiently close to the transition structure geometry to make this a valid assumption.

Climbing Nudged Elastic Band (cNEB)

The nudged elastic band (NEB) method, proposed by Henkelman and Jónsson,[98] is an efficient method for finding saddle points by optimizing a number of intermediate images along the reaction path between a given reactant and a product. Each image finds the lowest energy possible while maintaining equal spacing to neighboring images. This constrained optimization is done by adding spring forces along the band between images and by projecting out the component of the force due to the potential perpendicular to the band. Although this method has been successfully applied to a lot of complex micromagnetic systems[99] it has some limitations. Since the space of two neighboring images is fixed, a lot of images are needed to find an accurate transition state, thus make the computation very expensive. In recently, a new tangent definition and a climbing image method combine to allow for the more accurate finding of saddle points using the NEB with fewer images than the original method is introduced.

The climbing Nudged Elastic Band (cNEB)[100] is based on a small modification to the NEB method in which the highest energy image is driven up to the saddle point, as shown in Figure 1.10. This image does not feel the spring forces along the band.

Instead, the true force at this image along the tangent is inverted. In this way, the image tries to maximize its energy along the band, and minimize in all other directions. When this image converges, it will be at the exact saddle point. Because the highest image is moved to the saddle point and it does not feel the spring forces, the spacing of images on either side of this image will be different. It can be important to do some minimization with the regular NEB method before this flag is turned on, both to have a good estimate of the reaction coordinate around the saddle point, and so that the highest image is close to the saddle point.

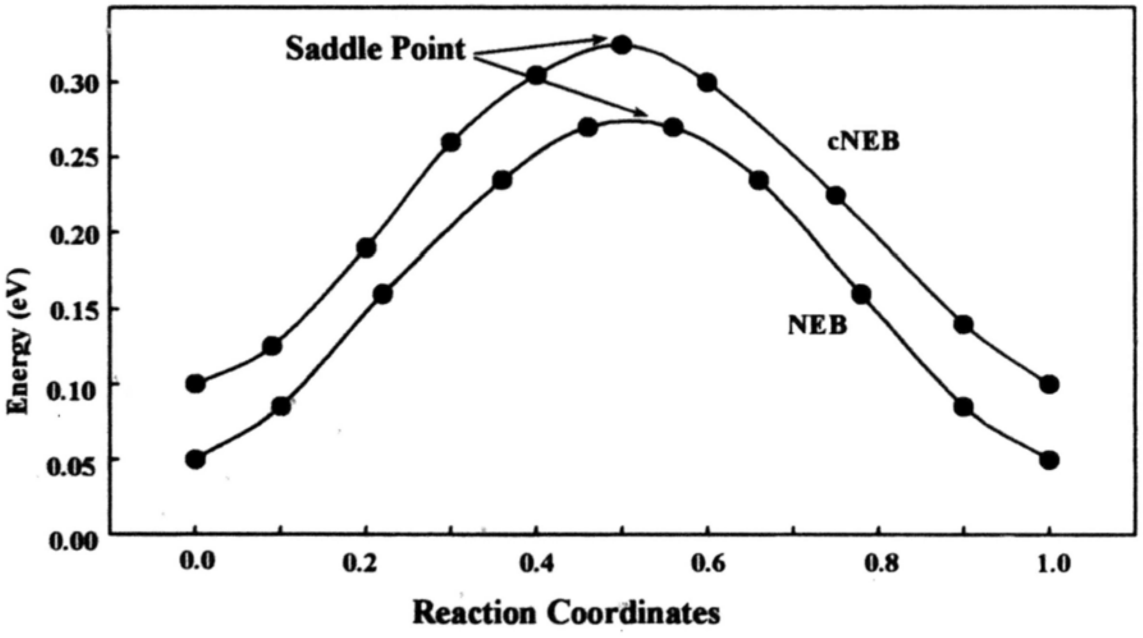

Figure 1.10 Comparison of NEB and climbing NEB (cNEB) for an *Al* adatom on an *Al(100)* surface. It demonstrates that how the climbing image calculation has shifted the position of the images by compressing the images on the left so that one image sits right at the saddle point. The figure is cited from the ref [101].

1.3 Reference

[1] Brusic V.; Frisch M.A.; Eldridge B.N.; Novak F.P.; Kaufman F.B.; Rush B.M.; Frankel G.S. *J. Electrochem.Soc.* **1991**, 138, 2253.

[2] Bent S.F. *Surf. Sci.* **2002**, 500, 879.

[3] Qhobosheane M.; Santra S.; Zhang P.; et al. *Analyst.* **2001**, 126, 1274.

[4] Coperet C.; Cgababas N.; Saint-Arroman R.P.; et al. **2003**, 42, 156.

[5] Land T.A.; Michely T.; Behm R.J.; et al. *J. Chem. Phys.* **1992**, 97, 6774.

[6] Engel T. *Surf. Sci. Rep.* **1993**, 18, 91.

[7] Avouris P, Walkup RE, Rossi AR, et al. *Surf. Sci.* **1996**, 363, 368.

[8] Chen J.G.; Basup N.G.; Surface Science. **1988**, 194, 397; Go E.P.; Thuermer K.; Reutt-Robey J.E.; Surface Science. **1999**, 437, 377; Netzer F.P.; Madey T.E.; Chem. Phys. Lett. **1982, 88**, 315; Mezhenny S.; Sorescu D.C.; Maksymovych P.; Yates J.T.; J. Am. Chem. Soc. **2002**, 124, 14202.

[9] Osterlund L.; Zoric I.; Kasemo B.; *Phys. Rev. B* **1997**, 55, 15452; Komrowski A. J.; et al., *Phys. Rev. Lett.* **2001, 8**724, 246103.

[10] Honkala K.; and Laasonen K.; *Phys. Rev. Lett.* **2000**, 84, 705.

[11] Yourdshahyan Y.; et al. *Solid State Comm.* **2001**, 117, 531; *Phys. Rev. B* **2002**, 65, 075416.

[12] Hellman A.; et al., *Surf. Sci.* **2003**, 532, 126; Ciacchi L. C.; Payne M. C.; *Phys. Rev. Lett.* **2004**, 92, 176104.

[13] Behler J.; et al., *Phys. Rev. Lett.* **2005**, 94, 036104.

[14] Behler J.; et al., Phys. Rev. Lett. 2006, 96, 079802; X. L. Fan, et al., *Phys. Rev.*

Lett. **2006**, 96, 079801.

[15] Cabrera, N. and Mott, N. F. *Rep. Prog. Phys.* **1948-49**, 12, 163.

[16] Zhukov, V.; Popova.; I and Yates, Jr. J. T. *Surf. Sci.* **1999**, 441, 251.

[17] Brune, H.; Wintterlin, J.; Behm, R. J.; and Ertl, G. *Phys. Rev. Lett.* **1992**, 68, 624; *J. Chem. Phys.* **1993,** 99, 2128.

[18] Schmid M.; Leonardelli G.; Tschelieβnig R.; Biedermann A.; Varga P.; *Surf. Sci.* **2001**, 478, L355.

[19] Yourdshahyan Y.; Razaznejad B.; Lundqvist B. I.; *Solid State Comm.* **2001**, 117, 531.; *Phys. Rev. B* **2002,** 65, 075416.

[20] Behler J.; Delley B.; Lorenz S.; Reuter K.; Scheffer M. *Phys. Rev. Lett.* **2005**, 94, 036104.

[21] B. Kasemo, E. To¨rnquist, J. K. No.rskov, and B. I. Lundqvist, *Surf. Sci.* **1979**, 89, 554.

[22] B. Kasemo, *Phys. Rev. Lett.* **1974**, 32, 1114.

[23] J. K. No.rskov, D. M. Newns, and B. I. Lundqvist, *Surf. Sci.* **1979**, 80, 179.

[24] J. Strömquist, L. Hellberg, B. Kasemo, and B. I. Lundqvist, *Surf. Sci.* **1996**, 352-354, 435.

[25] Yourdshahyan Y. *et al.*, *Phys. Rev. B* **2002**, 65, 075416.

[26] Hellman A. *et al.*, *Surf. Sci.* **2003**, 532, 126.

[27] Hellberg L.; Strömquist J.; Kasemo B.; Lundqvist B. I. *Phys. Rev. Lett.* **1995**, 74, 4742.

[28] Kato K.; Uda T.; Terakura K.; *Phys. Rev. Lett.* **1998**, 80, 2000.

[29] Rao, B. K.; Jena, P. *J. Chem. Phys.* **1999**, 111, 1890.

[30] Schultz, N. E.; Staszewska, G.; Staszewski, P.; Truhlar, D. G. *J. Phys. Chem. B* **2004**, 108, 4850.

[31] Knight, W. D.; Clemenger, K.; Deheer, W. A.; Saunders, W. A.; Chou, M. Y.; Cohen, M. L. *Phys. Rev. Lett.* **1984**, *52,* 2141-214.

[32] Martin, T. P.; Bergmann, T.; Gohlich, H.; Lange, T. *Chem. Phys. Lett.* **1990,** 172, 209.

[33] Leuchtner, R. E.; Harms, A. C.; Castleman, A. W. *J. Chem. Phys.* **1991**, *94,* 1093.

[34] Leuchtner, R. E.; Harms, A. C.; Castleman, A. W. *J. Chem. Phys.* **1989**, *91,* 2753.

[35] Gantefor, G. F.; Kiran, B.; Jena, P. Science **2008**, *319,* 438.

[36] Burgert, R.; Schnockel, H.; Olzmann, M.; Bowen, K. H. *Angew. Chem-Int. Ed.* **2006**, 45, 1476.

[37] Burgert, R.; Stokes, S. T.; Bowen, K. H.; Schnockel, H. *J. Am. Chem. Soc.* **2006,** 128, 7904.

[38] Bergeron, D. E.; Castleman, A. W.; Morisato, T.; Khanna, S. N. *Science* **2004,** 304, 84.

[39] Bergeron, D. E.; Roach, P. J.; Castleman, A. W.; Jones, N.; Khanna, S. N. *Science,* **2005**, *307,* 231.

[40] Schlier, R. E.; Farnsworth, H. E. *J. Chem. Phys.* **1959,** 30, 917.

[41] Levine, J. D. *Surf. Sci.* **1973**, 34, 90.

[42] Chadi, D. J. *Phys. Rev. Lett.* **1979**, 43, 43.

[43] Dabrowski, J.; Scheffler, M. *Appl. Surf* Sci. **1992**, 56-58, 15.

[44] Roberts, N.; Needs, R. J. *Surf. Sci.* **1990**, 236, 112.

[45] Kruger, P.; Pollmann, J. *Phys. Rev. E* **1993**, 47, 1898.

[46] Northrup, J. E. *Phys. Rev. B* **1993**, 47, 10032.

[47] Boland J. J. *Adv. Phys.* **1993**, 42, 129, and references therein.

[48] Waltenburg H. N.; Yates J. T. Jr. *Chem. Rev.* **1995**, 95, 1589, and references therein.

[49] Dürr M.; Hu Z.; Biedermann A.; Höfer U.; Heinz T. F. *Phys. Rev. Lett.* **2002, 88,** 046104.

[50] Boland J. J. *Phys. Rev. B.* **1991,** 44, 1383.

[51] Law J.T.; *J. Chem. Phys.* **1959**, 30, 1568

[52] Sinniah K.; Sherman M.G.; Lewis L.B.; et. al. *Phys. Rev. Lett.* **1989**, 62, 567.

[53] Doren D. J. *Adv. Chem. Phys.* **1996**, 95, 1.

[54] Kolasinski K.W.; et al. *Phys. Rev. Lett.* **1994**, 72, 1356

[55] A. Gross, M. Bockstedte, and M. Scheffler, *Phys. Rev. Lett.* **1997**, 79, 701.

[56] Namiki A. Progr. *Surf. Sci.* **2006, 8**1, 337.

[57] Dürra M.; Höfer U. *Surf. Sci. Rep.* **2006**, 61, 465.

[58] Wilhelm B.; Eckhard P. *Progr. Surf. Sci.* **2008**, 83, 263.

[59] Radeke M.R..; Carter E.A. *Phys. Rev. B* 1996, 54, 11803.

[60] Boland J.J. *Phys. Rev. Lett.* **1991,** 67, 1539.

[61] Vittadini A.; Selloni A. *Chem. Phys. Lett.* **1995**, 235, 334

[62] Shi J.; Kang H.C. *J. Chem. Phys.*, **2005**, 123, 034701.

[63] Dürr M.; Raschke M.B.; Höfer U. *J. Chem. Phys.* **1999**, 111, 10411; *Surf. Sci. Rep.* **2006**, 61, 46.

[64] Raghavachari K.J. *J. Chem. Phys.* **1986**, 84, 5672.

[65] Okamoto Y. *J. Phys. Chem. B* **2002**, 106, 570; Filippi C.; Healy S.B., Kratzer P.; Pehlke E., Scheffler M., *Phys. Rev. Lett.* **2002**, 89, 166102.

[66] Dürr M.; Biedermann A.; Hu Z.; Höfer U.; Heinz T. F.; *Science*, **2002**, 296, 1838.

[67] Shen T.-C.; Wang C.; Abeln G.C.; Tucker J.R.; et al. *Science*, **1995**, 268, 1590

[68] Shen T.-C.; Avouris P. *Surf. Sci.* **1997**, 390, 35.; *Chem. Phys. Lett.* **1996**, 257, 148.

[69] Schrödinger E. Ann. Physik **1926**, 79, 361.

[70] Kolos, W.; Wolmiewicz, L. *J. Chem. Phys.* **1964**, *41*, 3663.

[71] Sutcliffe, B. T. *Adv. Quantum Chem.* **1997**, *28*, 65.

[72] Szabo, A. and Lee, A. M. *Modern Quantum Chemistry* McGraw-Hill, **1982**.

[73] Levine, I. N. *Quantum Chemistry* (Prentice Hall, London, **2000,**) 5th edition.

[74] Hohenberg, P. and Kohn W. *Phys. Rev.* **1964**, *136*, 864B.

[75] Kohn, W.; Sham, L. J. Phys. Rev. A **1965**, 140, 1133.

[76] Koch, W. and Holthausen, M. C. *A Chemist's Guide to Density Functional Theory.* Second Edition, Wiley, **2001**.

[77] Dirac, P.A.M. Proc. Com. Phil. Soc. **1930**, 26, 376.

[78] Burke, K.; Perdew, J. P.; Wang, Y. In *Electronic Density Functional Theory:*

Recent Progress and New Directions; Dobson, J. F., Vignale, G., Mukunda, P. D., Eds; New York : Plenum Press, **1998**.; Perdew, J. P. In Electronic Structure of Solids; Ziesche, P., Eschrig, H., Eds.; Academie Verlag: Berlin, **1991**, pp 11.; Perdew, J. P.; Chevary, J. A.; Vosko, S. H.; Jackson, K. A.; Pederson, M. R.; Singh, D. J.; Fiolhais, C. *Phys. Rev. B* **1992**, 46, 6671.; Perdew, J. P.; Chevary, J. A.; Vosko, S. H.; Jackson, K. A.; Pederson, M. R.; Singh, D. J.; Fiolhais, C. *Phys. Rev. B,* **1993**, 48, 4978.; Perdew, J. P.; Burke, K.; Wang, Y. *Phys. Rev. B* **1996**, 54, 16533.

[79] Becke, A. D. *J. Chem. Phys.* **1993**, 98, 1372.

[80] Becke, A.D. *J. Chem. Phys.*, **1993,** 98, 5648.

[81] Stephens, P.J.; Devlin, J.F.; Chabalowski C.F. et al., *J. Phys. Chem.*, **1994,** 98, 11623.

[82] Schmider H.L.; Becke, A.D. *J. Chem. Phys.*, **1998,** 108, 9624.

[83] Burke, K.; Ernzerhof, M.; Perdew, M. *Chem. Phys. Lett.*, **1997,** 265, 115.

[84] Kang, J.K.; Musgrave, C.B. *J. Chem. Phys.*, **2001,** 115, 11040.

[85] Xu, X.; Goddard III, W.A. *J. Phys. Chem. A.* **2004,** 108(40): 8495.

[86] Zhang Y. K.; Yang W. T.; *J. Chem. Phys.* **1998,** 109, 2604.

[87] Car R.; Parrinello M. *Phys. Rev. Lett.* **1985,** 55, 2471.

[88] Kittel C. Introduction to Solid State Physics 7th edition Wiley, **1996**.

[89] Payne M. C.; Teter M. P.; Allan D. C.; Arias T. A.; Joannopoulos J. D. *Rev. Mod. Phys.* **1992,** 64, 1045.

[90] Marx D.; Hutter J. *Modern Methods and Algorithms of Quantum Chemistry*

John von Neumann Institute for Computing, NIC Series, Vol. 1, **2000.**

[91] Hellmann, H. *J. Chem. Phys.* **1935**, 3, 61.; Hellmann, H.; Kassatotschkin, W. *J. Chem. Phys.* **1936,** 4, 324.

[92] Phillips, J. C. *Phys. Rev.* **1958**, 112, 685.; Phillips, J. C.; Kleinman, L. *Phys. Rev.* **1959**, 116, 287.; Laasonnen K.; Pasquarello A.; Car R.; Lee C.; Vanderbilt D. *Phys. Rev. B* **1993**, 47, 10142.

[93] Vanderbilt, D. *Phys. Rev. B* **1990**, 41, *7892.*

[94] Kang, I. Y.; Kim, Y. S.; Chung, Y. C.; Kim, H.; Kim, D. S.; Kim, J. *J. Cera. Proc. Res.* **2002**, 3(3), 171.

[95] Blöchl, P.E. *Phys. Rev. B* **1994**, 50, 17953.

[96] Kresse, G.; Joubert, J. *Phys. Rev. B* **1999,** 59, 1758.

[97] Schlegel H.B. *J. Comp. Chem.* **1982,** 3, 214; Schlegel H.B. *in New Theoretical Concepts for Understanding Organic Reactions, Ed. J. Bertran* (Kluwer Academic, The Netherlands, **1989**) 33-53; Schlegel H.B. *in Modern Electronic Structure Theory, Ed. D. R. Yarkony* (World Scientific Publishing, Singapore, **1995**).

[98] Henkelman, G.; Jónsson, H. J. Chem. Phys. **2000**, 113, 9978.

[99] Dittrich, R.; Schrefl, T.; Suess, D.; Scholz, W.; Forster, H.; Fidler, J. *J. Magn. Magn. Mater.* **2002,** 250, 12.

[100]Henkelman, G.; Uberuaga, B. P.; Jónsson, H. *J. Chem. Phys.* **2000,** 113 , 9901.

[101]Olsen, R. A.; Kroes, G. J.; Henkelman, G.; Arnaldsson, A.; Jónsson, H. *J. Chem. Phys.* **2004,** 121, 9776.

Chapter Two

Theoretical Study on Al_{13}^{-}+O_2 Reaction and Its Comparison with the Chemisorption of O_2 on Al(111)

2.1 Introduction

The initial reaction between O_2 and Al(111) has been a much studied problem, by both experiments[1-4] and calculations[5-12]. It is a model system for understanding the metal oxidation process, which is related to technically important issues such as corrosion and heterogeneous catalysis. The electronic structure of Al(111) involves only sp bands, and its geometric structure, cut from a face-center-cubic lattice, is fairly simple, with little surface reconstruction. Experimentally, molecular beam scattering has clearly identified the reaction as an activated process[1,2]. The initial sticking probability of O_2 on Al(111) is very low ($\sim 10^{-2}$) at low O_2 incident energy (0.024 eV). As the incident energy increases, so does the sticking probability, which reaches a constant value around 0.9 for incident energy above 0.6 eV[1]. In other words, there is an activation barrier for O_2 to react with Al(111). But unfortunately, density functional theory calculations have so far failed to reproduce such a barrier. On the calculated ground state surface, the chemisorption of O_2 on Al(111) is exothermic by 1.5-2.1 eV and barrierless[5,6,7,10].

Such a glaring discrepancy between experiment and theory has been the subject of many theoretical studies[5-12]. There are two possible explanations. The prevalent view attributes it to non-adiabatic effects, involving electronic excitation[8-10]. Barriers have indeed been found on the excited states. But to invoke such an explanation, one has to assume that the ground state surface is somehow inaccessible, which has been a subject of debate[11,12]. It is also possible that density functional theory, despite its impressive success for many surface reactions, fails for this particular problem[5]. Such a possibility is largely overlooked, and in any case, is not easy to prove due to the lack of a suitable computational model and the high computational cost involved. In this paper, we use Al_{13}^- as a cluster model for Al(111) and demonstrate that the long standing discrepancy is not due to electron excitation, but due to defects in previous calculations for treating charge transfer.

Mapping out the path for the $Al_{13}^-+O_2$ reaction is computationally demanding at a high accuracy level, due to the problem size. But such a model is very worthwhile for three reasons. First, with a highly symmetric icosahedron structure[13,14], Al_{13}^- has 20 equivalent surfaces, each of which contains three Al atoms arranged in an equilateral triangle, the same structure as on Al(111). It is therefore an ideal cluster model for Al(111). Second, it is experimentally well-established that Al_{13}^- is not very reactive towards O_2[18,19]. In fact, the trick to produce Al_{13}^-, after the generation of Al_n^- mixture by laser ablation, is to leak O_2 into the chamber, which purges away other clusters and leaves Al_{13}^- in abundance. Such inertness is similar to the activated chemisorption of O_2 on Al(111). Finally, Al_{13}^- is important in its own right. With 40 valence electrons, its configuration resembles a rare gas atom according to the Jellium model[15] and can be considered as a stable superatom with fascinating chemical properties[16,17]. Furthermore, the reactions between Al_n^-(n=10–20) and oxygen have been found to follow the conservation of spin selection rule very recently[20], and explained only by the variation in reaction energy. By focusing on

Al_{13}^-, our study will not only demonstrate the similarity between the $Al_{13}^-+O_2$ reaction and the O_2 chemisorption on Al(111), and in the process identify the defects of previous calculations, but also show that in the cluster reaction, the inertness of Al_{13}^- is kinetic, not thermodynamic.

2.2 Computational details

Two types of methods have been employed in the current study, density functional theory with a number of different functionals (B3LYP, BLYP, BHandHLYP[21-23], PBE[24,25], and PW91[26-28]), and Hartree-Fock based methods with electron correlations treated by configuration interaction (QCISD(T)), coupled cluster levels with single and double excitations (CCSD), and CCSD(T) in which triple excitations are included[29]. In DFT calculations, all geometry optimizations and corresponding energy calculations are carried out with 6-31+G* basis set, while for CCSD, CCSD(T) and QCISD(T) energy calculations 6-31G* basis set is used due to the limitation of computational cost. All calculations are carried out with the Gaussian 03 package[30].

2.3 Results and discussions

2.3.1 Reaction path for Al_{13}^- with O_2

The structures and reaction paths are first explored using the B3LYP functional with a 6-31+G* basis set. The icosahedral structure is identified as the most stable structure and the optimized distance between two neighboring Al atoms in Al_{13}^- is 2.8 Å, in agreement with previous results[10]. As Al is not a transition metal, spin flipping due to spin-orbit coupling should not play a significant role in the initial reaction, and the system is constrained to the triplet state to account for the open shell on O_2. Similar to the surface reaction, there are three possible reaction paths for an O_2 molecule approaching to Al_{13}^- cluster. Oxygen can be adsorbed in (a) "hollow" position, i.e. between three Al atoms on the cluster; (b)"bridge" position, i.e. between two Al atoms on the cluster surface and (c) surface "top" position, i.e. directly on top of an Al atom on the cluster surface. To map out the most favorable reaction path, the distance between O_2 and Al_{13}^- is constrained to a specific value between 2.7 – 2.2 Å with a step size of 0.1 Å, while at each step the total energy is minimized by optimizing the geometry. It turns out that such calculations always lead to the reaction shown in Figure 2.1, with O_2 attacking a "top" site. Furthermore, there is no barrier for this path, and it leads to an intermediate structure labeled as LM1, with the total energy lowered by 18.4 kcal/mol. When the energy is calculated at the coupled cluster level, the reaction energy is revised up to around 9.7 kcal/mol, in good agreement with the value of 9.8 kcal/mol reported before[20].

These results pose a difficulty. Experimentally, Al_{13}^- is known to be less reactive than other anionic Al_n^- clusters. To explain the stability of Al_{13}^-, Burgert et al. suggested [20] that there is a barrier for the triplet O_2 to be converted into the singlet state, and therefore the intermediate structure could easily dissociate back to Al_{13}^- and O_2. A similar argument was proposed previously to account for the adsorption of O_2 on Si(100) [32], but was later demonstrated to be inadequate, because a triplet O_2 can be trapped on Si(100) in a deep potential well and spin-conversion was a guaranteed eventuality[31]. The same is actually true for the Al_{13}^-+O_2 system. As shown in Figure 2.1, by staying on the triplet state, LM1 can be transformed further to a much more stable structure LM2. The barrier is a tiny 0.4 kcal/mol, while the overall reaction energy is exothermic by 46.4 kcal/mol. The logical conclusion is that a triplet O_2 reacts with Al_{13}^- easily and produces a product so stable that spin conversion is assured and does not matter. Similar to the reaction of O_2 on Al(111), there is an obvious discrepancy between theory and experiment.

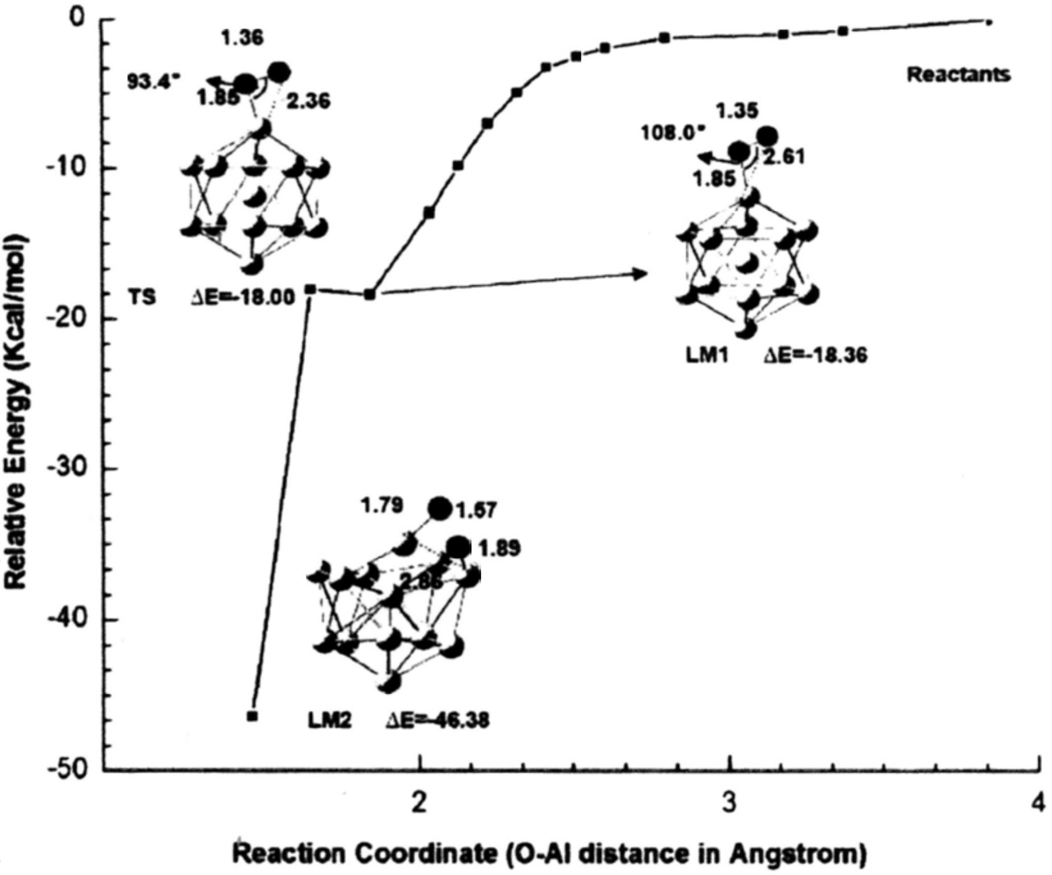

Figure 2.1 The B3LYP/6-31+G* calculated potential energy surface curve for the triplet O_2 attacking a top Al atom of Al_{13}^-. The reaction coordinate is the Al–O distance, and the O_2 molecule approaches Al_{13}^- as the Al–O distance decreases. The triplet O_2 is chemically adsorbed on Al_{13}^- without any activation barrier, forming the intermediate structure LM1. And LM1 can be further converted to the more stable intermediate LM2 after traversing an activation barrier of only 0.36 kcal/mol.

2.3.2 Charge transfer and self-interaction error

The discrepancy between experiment and theory has been attributed to the non-adiabatic effect which involves electronic excitation in previous investigations[8-10]. Here we provided another explanation which includes charge transfer.

At a separation of 4.0 Å, the natural population charge on O_2 is an insignificant amount of -0.02. This is not surprising since at this distance the calculated orbital energy for the partially filled O_2 π orbital is -1.31 eV, while the energy for the highest occupied orbital on Al_{13}^- is -2.29 eV. There is little electron transfer from Al_{13}^- to O_2, and a small number of -0.02 is basically a round-off error. Electron transfer becomes more significant as the O_2–Al_{13}^- distance decreases, reaching -0.40 at 2.4 Å, and -0.74 in LM1. For such a cluster reaction, electron excitation should not play a significant role while the charge transfer is really important.

It is known that in treating chemical problems involving charge transfer[33-36], one must be careful with the self-interaction error (SIE). The origin of SIE has been introduced in Chapter One. For systems with fractional electron number, the term for the classical electrostatic repulsion between electrons can not be properly canceled by the exchange-correlation term, due to the defect of the exchange-correlation functional used in DFT calculation. DFT calculations can not give correct energy calculation results as well as some other properties in treating reactions involving charge transfer. The common trend is that the energy along the reaction coordinate is underestimated, and the amount of electron transfer is overestimated. Previous studies have demonstrated that such an error can be partially corrected by mixing the Hartree-Fock exchange term into the exchange functional, and a larger fraction would make the self interaction error smaller[34].

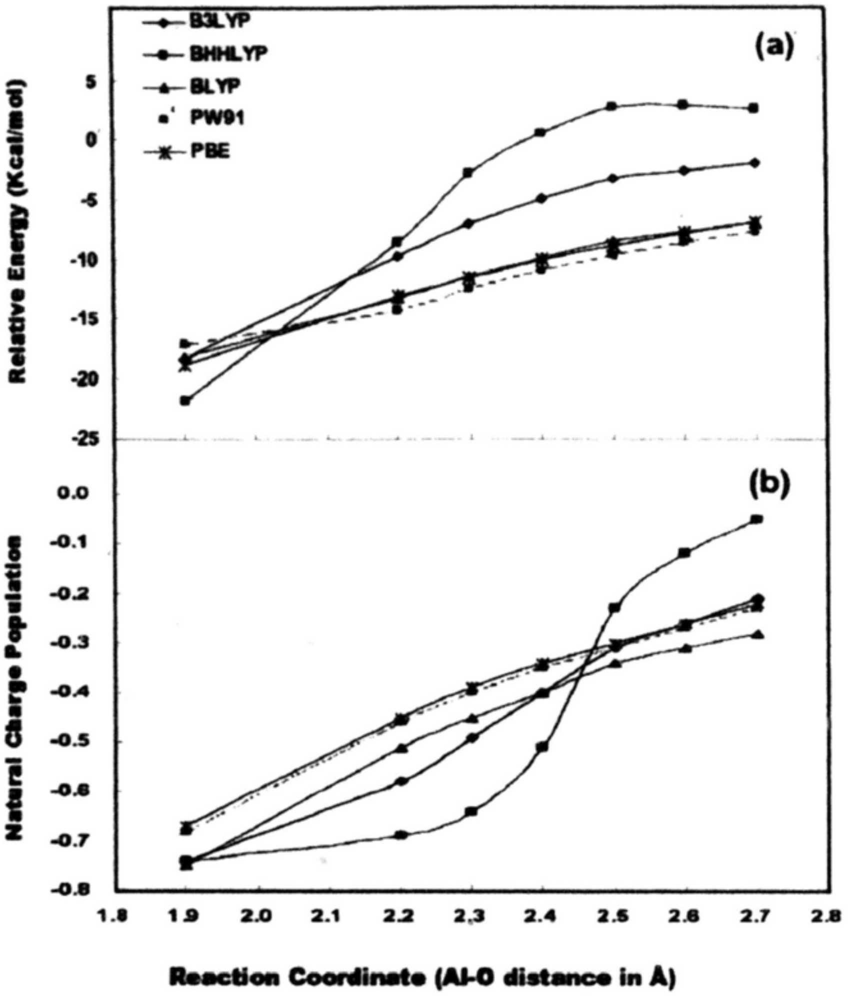

Figure 2.2 (a) Potential surface energy scan calculated by three pure functionals (BLYP, PW91, PBE), and two mixed functional, (B3LYP and BHHLYP, with 20% and 50% Hartree-Fock exchange respectively); (b) The charge population versus to the Al-O distance. The reaction coordinate is the distance between the approaching oxygen atom and the top Al atom.

We have repeated the calculation of reaction path with a number of different exchange correlation functionals, as shown in Figure 2.2. The three pure gradient corrected functionals (BLYP, PW91, and PBE), produce similar results. When 20 percent Hartree-Fock exchange is included in the exchange term, as in B3LYP, the energy is raised along most of the points on the reaction path by around 5 kcal/mol. When the percentage of Hartree-Fock exchange is raised to 50% in the BHHLYP calculation, the energy is raised further, and in the range of 2.4–2.7 Å for the Al–O distance the energy is above zero, which is relative to the total energy at infinite Al_{13}^- and O_2 separation. A transition structure is also located at this level, and the calculated reaction barrier is 2.9 kcal/mol, with an Al–O distance at 2.58 Å.

Also shown in Figure 2.2(b) is the charge on O_2, as calculated from the natural population analysis, plotted against the Al–O distance. Again, with 50% Hartree-Fock exchange, the charge on O_2 is almost zero at 2.7 Å, and drops into the negative only for Al–O distance between 2.4–2.5 Å, which indicates charge transfer to the O_2 molecule and the beginning of Al–O bonding interaction. The curves obtained by the three pure functionals are almost linear, and even at 2.7 Å, the charge transferred to O_2 is already around -0.2. Obviously, the charge transfer from Al_{13}^- to O_2 takes place much earlier due to the self-interaction error with such pure functionals, which underestimate the total energy along the reaction path. In fact, even at an Al–O distance of 4 Å, the charge on O_2 is already -0.1. This is similar to the previously reported observation of charge transfer from Al(111) to O_2 at large separation[10-12], which was taken as evidence that non-adiabatic effects must be important in the reaction process. The comparison between the mixed and pure functional results demonstrates that it is actually due to the defects in pure functionals.

Ideally, one should obtain a reaction path calculated by post-Hartree-Fock methods to verify our analysis. However, with 52 valence electrons in the $Al_{13}^-+O_2$ system, the computational cost for doing structural optimization and for locating a transition structure with millions configurations is exorbitantly high. Here, we adopt a compromise, by doing single point energy calculations, using the coupled cluster method with single and double excitation (CCSD) and with a 6-31G* basis set, on the geometries obtained from density functional theory calculations along the reaction paths.

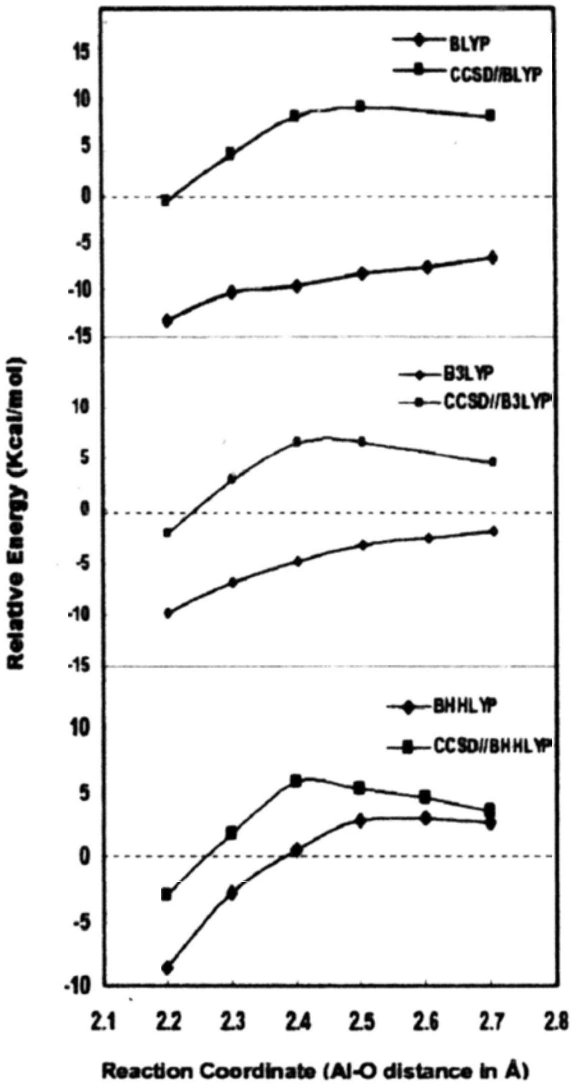

Figure 2.3 Potential energy surface scan calculated by different functionals, pure (BLYP), 20% mixed (B3LYP) and and 50% mixed (BHHLYP), and by single point coupled cluster calculations along the reaction path. The barriers found by the coupled cluster calculations are 9.1, 6.7, and 5.8 kcal/mol respectively, from top to bottom.

As shown in Figure 2.3, the coupled cluster method raised the energy value along the reaction paths, by more than 10 kcal/mol for the pure functional (BLYP), but by only 5 kcal/mol for the 50% mixed functional (BHHLYP). A reaction barrier is predicted for Al–O distance between 2.4–2.5 Å, although the value is dependent on the functional used. The errors in the optimized geometry should be the least when calculated by the 50% mixed functional, and the barrier obtained by coupled cluster correction at 5.8 kcal/mol is indeed the lowest among the three curves, which can be taken as the lowest upper bound for the barrier. The barrier of 2.9 kcal/mol obtained by the search for transition structure with the 50% mixed functional (without coupled cluster correction) is the lower bound.

2.3.3 Post-Hartree-Fock calculation results for $Al_{13}^{-}+O_2$ reaction

In addition to CCSD, some other post-Hartree-Fock calculations, such as CCSD(T) and QCISD(T), are also carried out. As shown in Figure 2.4, both CCSD(T) and QCISD(T) gave quit similar results on the calculated PES. The activation barriers calculated by CCSD(T) and QCISD(T) are 9.2 and 10.1 kcal/mol respectively. The energies released for the formation of LM1 are 9.7 and 10.3 kcal/mol for CCSD(T) and QCISD(T) results, which is in agreement with the recent values reported by Bowman (the adsorption energy they get for CCSD(T) calculation is 0.36 eV which is equal to 9.8 kcal/mol) [20].

Compared with B3LYP, CCSD(T) and QCISD(T) calculations raised not only the activation barrier but also the reaction heat. B3LYP calculation gives no activation barrier for O_2 adsorption while CCSD(T) and QCISD(T) identify activation barrier about 10 kcal/mol. On the other hand, B3LYP calculation gave the adsorption heat of about -46 kcal/mol for LM2 but CCSD(T) and QCISD(T) calculations indicated that it was only about -30 kcal/mol. It can be concluded that B3LYP functional is not good for describing this specific system, it underestimate the activation barrier and overestimate the reaction heat.

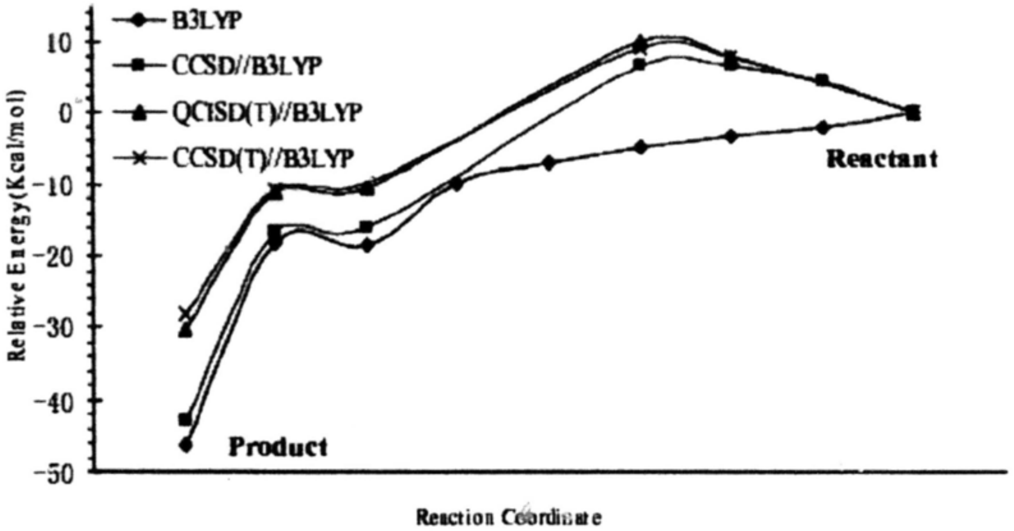

Figure 2.4 Potential energy surface curves calculated by B3LYP and some post-HF methods. All the post-Hartree-Fock calculations, including CCSD, CCSD(T) and QCISD(T), are single point energy calculations based on geometries which are optimized using B3LYP.

2.3.4 Potential energy surface for O_2 adsorption on Al_7^-

For comparison, we have also calculated the path for Al_7^-+O_2 reaction, following the same procedure. As shown in Figure 2.5, the calculated total energy drops without a barrier as the Al–O distance decreases along the curve calculated by the 50 % mixed functional, although there is a barrier of ~3 kcal/mol when the energy is corrected by coupled cluster method. The Al–O distance at the transition structure is 3.0 Å with a charge of -0.34 on O_2. This distance is significantly larger than the corresponding distance of 2.4 Å for Al_{13}^- and in line with the expectation that the electronic shell on Al_7^- is less stable than that on Al_{13}^- and the charge transfer to O_2

takes place earlier along the reaction path. It would be interesting to investigate systematically the presence or absence of such a barrier for other anionic aluminum clusters in light of the recent experimental results[20].

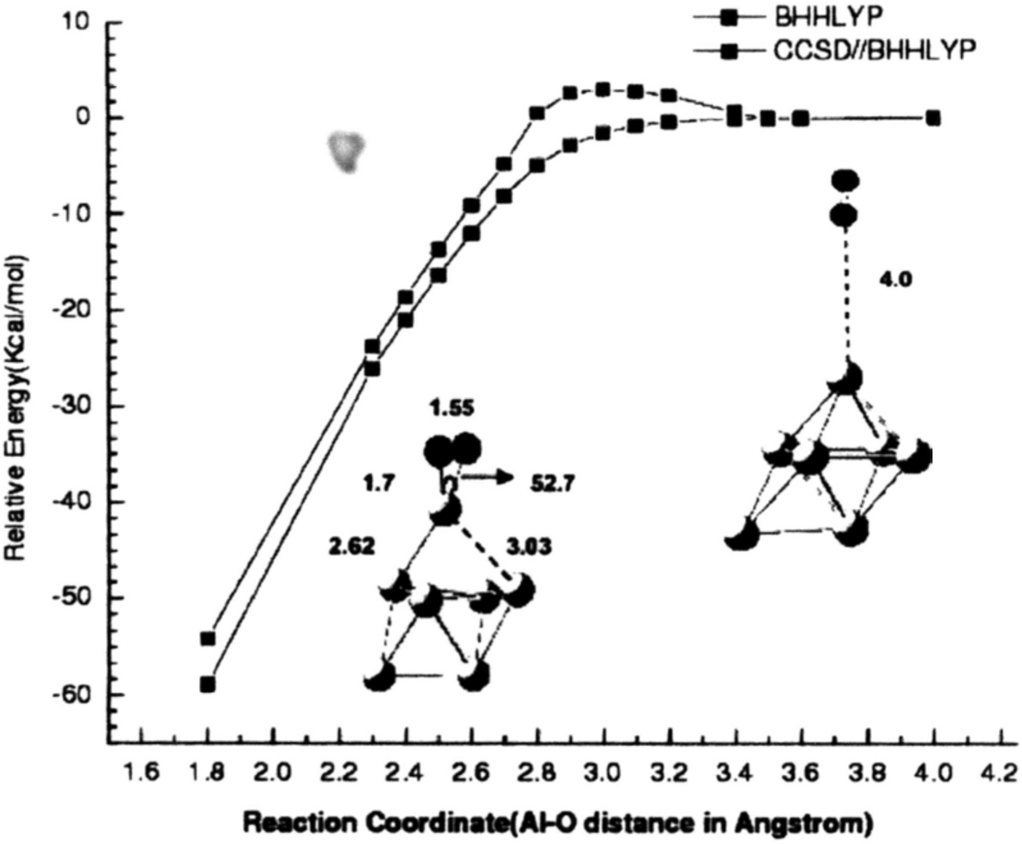

Figure 2.5 The potential energy surface for the triplet O_2 attacking a top Al atom of Al_7^-, as calculated by 50% mixed functional (BHHLYP) and the coupled cluster single point energy (CCSD//BHHLYP). The reaction coordinate is the Al–O distance.

2.4 Conclusion

The stability of Al_{13}^- is well-known, especially its chemical inertness towards oxygen. Our results indicate that the $Al_{13}^-+O_2$ reaction is actually exothermic, even on the triplet surface. Its chemical inertness is relative, and is due to the presence of a small barrier. Such a kinetic factor is also likely to be important in the reactions between oxygen and other aluminum clusters, since recent experimental observations have shown that the reaction rate is dependent on the spin state of the O_2 molecule (triplet or singlet) and the cluster size (even or odd).

Al_{13}^- is only a cluster model for Al(111) and the two are not expected to be exactly the same. For example, the protruding single atom on the Al_{13}^- cluster will be more active than for a regular site on Al(111); and relaxing the cluster gives it additional flexibility that is likely not present at the surface site. However, Al(111) is similar to Al_{13}^- in one crucial aspect, when O_2 is 3.0 Å above Al(111), the $2p\pi^*$ peak of O_2 is close to but still above the Fermi level. Electron transfer from Al(111) to O_2 occurs upon bonding interaction between oxygen and aluminum. Therefore, there should be a barrier for the initial oxidation of Al(111) by oxygen, which is not due to non-adiabatic effect. The presence of such a barrier in the Al_{13}^-+O_2 reaction resolves the long standing discrepancy between theory and experiment.

More importantly, the qualitative errors in previous calculations are due to self-interaction error in a pure functional. The two erroneous features in the previous studies on surface oxidation are reproduced in the calculation of Al_{13}^-+O_2 reaction: the reaction is barrierless, and there is substantial charge transfer to the O_2 molecule even at large Al_{13}^-/O_2 separation. Fixing such errors must be achieved by either post-Hartree-Fock treatment, or to a partial degree, by substantial mixing of Hartree-Fock exchange into a pure functional. This consideration could also be significant in other surface oxidation or catalysis.

It is interesting to notice that despite its stable electronic shell, the reaction between Al_{13}^- and O_2 is exothermic. The well-known chemical inertness of Al_{13}^- towards oxygen[18,19] is kinetic, due to the presence of a barrier when the charge is transferred from Al_{13}^- to O_2 through chemical bonding. Such kinetic factors should be an important consideration in the reactions of aluminum and other metal clusters.

2.5 Reference

[1] Osterlund L.; Zoric I.; Kasemo B. *Phys. Rev. B* **1997**, 55, 15452.

[2] Komrowski A. J.; Sexton J.; Kummel Z. A. C.; Binetti M.; Weisse O.; Hasselbrink E. *Phys. Rev. Lett.* **2001,** 8724, 246103 .

[3] Brune H.; Wintterlin J.; Trost J.; Ertl G.; Wiechers J;. Behm R. J. *J. Chem. Phys.* **1993**, 99, 2128.

[4] Schmid M.; Leonardelli G.; Tscheliessnig R., Biedermann A.; Varga P. *Surf. Sci.* **2001**, 478, L355.

[5] Honkala K.; Laasonen K. *Phys. Rev. Lett.* **2000, 84,** 705.

[6] Yourdshahyan Y.; Razaznejad B.; Lundqvist B. I.; *Solid State Comm.* **2001**, 117, 531.

[7] Yourdshahyan Y.; Razaznejad B.; Lundqvist B. I. *Phys. Rev. B* **2002,** 65, 075416.

[8] Hellman A.; Razaznejad B.; Yourdshahyan Y.; Ternow H.; Zoric I.; Lundqvist B. I. *Surf. Sci.* **2003**, 532, 126.

[9] Ciacchi L. C.; Payne M. C. *Phys. Rev. Lett.* **2004,** 92, 176104.

[10] Behler J.; Delley B.; Lorenz S.; Reuter K.; Scheffer M. *Phys. Rev. Lett.* **2005,** 94, 036104.

[11] Behler J.; Reuter K.; Scheffer M. *Phys. Rev. Lett.* **2006,** 96, 079802.

[12] Fan X. L.; Lau W. M.; Liu Z. F. *Phys. Rev. Lett.* **2006,** 96, 079801.

[13] Rao B. K.; Jena P. *J. Chem. Phys.* **1999,** 111, 1890.

[14] Schultz N. E.; Staszewska G.; Staszewski P.; Truhlar D. G. *J. Phys. Chem. B* **2004,** 108,4850.

[15] Knight W. D.; Clemenger K.; Deheer W. A.; Saunders W. A.; Chou M. Y.;

Cohen M. L. *Phys. Rev. Lett.* **1984**, 52, 2141.

[16] Bergeron D. E.; Castleman A. W.; Morisato T.; Khanna S. N. *Science* **2004**, 304, 84.

[17] Bergeron D. E.; Roach P. J.; Castleman A. W.; Jones N.; Khanna S. N. *Science* **2005**, 307, 231.

[18] Leuchtner R. E.; Harms A. C.; Castleman A. W. *J. Chem. Phys.* **1989**, 91, 2753 .

[19] Leuchtner R. E.; Harms A. C.; Castleman A. W. *J. Chem. Phys.* **1991**, 94, 1093.

[20] Burgert R.; Schnockel H.; Grubisic A.; Li X.; Stokes S. T.; Bowen K. H.; Gantefor G. F.; Kiran B.; Jena P., *Science* **2008,** 319, 438.

[21] Becke A. D. *J. Chem. Phys.* **1993, 98,** 5648.

[22] Becke A. D. *Phys. Rev. A* **1988, 38,** 3098 ().

[23] Lee C. T.; Yang W. T.; Parr R. G. *Phys. Rev. B* **1988**, 37, 785.

[24] Perdew J. P.; Burke K.; Ernzerhof M. *Phys. Rev. Lett.* **1996**, 77, 3865.

[25] Perdew J. P.; Burke K.; Ernzerhof M. *Phys. Rev. Lett.* **1997**, **78,** 1396.

[26] Perdew J. P.; Burke K.; Wang Y. *Phys. Rev. B* **1996**, 54, 16533.

[27] Perdew J. P.; Chevary J. A.; Vosko S. H.; Jackson K. A.; Pederson M. R.; Singh D. J.; Fiolhais C. *Phys. Rev. B* **1993,** 48, 4978.

[28] Perdew J. P.; Chevary J. A.; Vosko S. H.; Jackson K. A.; Pederson M. R.; Singh D. J.; Fiolhais C. *Phys. Rev. B* **1992,** 46, 6671.

[29] Pople J. A.; Headgordon M.; Raghavachari K.; *J. Chem. Phys.* **1987**, 87, 5968.

[30] M. J. *et al.*. Frisch, *Gaussian03* (Gaussian, Inc., Pittsburgh, PA, 2003).

[31] Fan X. L.; Zhang Y. F.; Lau W. M.; Liu Z. F. *Phys. Rev. Lett.* **2005**, 94, 016101.

[32] Kato K.; Uda T.; Terakura K. *Phys. Rev. Lett.* **1998,** 80, 2000.

[33] Ruiz E.; Salahub D. R.; Vela A. *J. Phys. Chem.* **1996**, 100, 12265.

[34] Zhang Y. K.; Yang W. T.; *J. Chem. Phys.* **1998,** 109, 2604.

[35] Karpfen A.; *J. Phys. Chem. A* **2000,** 104, 6871.

[36] Grafenstein J.; Kraka E.; Cremer D. *J. Chem. Phys.* **2004**, 120, 524.

Chapter Three

Dynamic Factors in the Reactions between the Magic Cluster Al_{13}^- and HCl/HI

3.1 Introduction

Al_{13}^- is a well-known magic cluster, among the many types of metal clusters that have been extensively studied as nano-scale intermediates between metal atoms and bulk metals[1-4]. It has a highly symmetric icosahedral structure, with one central atom and 12 equivalent Al atoms forming 20 equilateral triangle[5,6]. While the central Al atom is situated in a bonding environment similar to the cuboctahedral geometry in the bulk aluminium, each triangle resembles the surface structure of Al(111), making Al_{13}^- an interesting molecular model for both the Al bulk and the Al surface[1]. Studies on reactions with Cl_2 and HCl measured by Fourier Transform Ion Cyclotron Resonance (FT-ICR) mass spectrometry have identified intermediate products in real time and provided invaluable insights into the oxidation and dissolution of bulk metals[7,8]. The electronic structure of Al_{13}^- is also remarkable. With its nearly spherical geometry, the atomic cores in Al_{13}^-, including both the metal nuclei and inner shell electrons, produce a spherical jellium potential. The 40 valence electrons in Al_{13}^- can be filled as $1s^2 1p^6 1d^{10} 2s^2 1f^{14} 2p^6$, in shell closure, which makes it "magic" with remarkable stability[9,10]. Al_{13}^- is therefore a super-atom, and potentially a building block for nano-structures[11-14]. The stability of the Al_{13}^- electronic shells means a high electron affinity for neutral Al_{13} comparable to that for chlorine and fluorine atoms, and in bonding with iodine Al_{13}^- indeed behaves like a super-halide atom[15-16].

In reactivity, Al_{13}^- is also unique in being less reactive than other aluminium clusters. The best known example was in the case of exposure to oxygen. When doses of oxygen were leaked into a flow tube, most other Al_n^- were purged, while the signal for Al_{13}^- became dominant[4,17,18], which was again attributed to the stability of Al_{13}^- as predicted by the Jellium model. However, we have recently demonstrated that the reaction between Al_{13}^- and O_2 was considerably exothermic and thermodynamically quite favorable, and the reason for the stability of Al_{13}^- towards oxygen exposure was kinetic, due to the presence of a reaction barrier[19]. True to the expectation of Al_{13}^- as a molecular model for the Al surface,[1] the identification of this barrier resolved a long standing puzzle in the initial chemisorption of O_2 on Al(111): a barrier was identified in experiment[20-23] but not in any theoretical calculations on the ground state potential surface[24-29]. It turned out that in the slab model based density functional theory (DFT) calculations, the typical exchange-correlation functionals failed to properly treat the electron transfer involved in the chemisorption due to self-interaction errors. But by using Al_{13}^- as a molecular model, this error could be clearly identified by both post-Hartree-Fock treatment and by the inclusion of a larger percentage of Hartree-Fock exchange integrals into the mixed exchange-correlation functional[19].

Many other examples of size-dependent reactivities for aluminium clusters and their halide derivatives have been identified in recent studies, although theoretical calculations have for the most part been focused on the thermodynamic stability[7,8,15,18,30-34]. The dynamic aspect of such reactions, such as the presence of a barrier in the $Al_{13}^-+O_2$ reaction, has not yet been fully explored, despite its obvious importance for understanding the chemistry of these nano-intermediates. In this regard, the reaction between Al_{13}^- and HX (HX=HCl or HI) provides an interesting problem. Experimentally, it has been observed that the Al_{13}^{-}+HCl reaction must be promoted by the application of radio frequency pulses, while in contrast, HI reacted readily with Al_{13}^{-}[7]. The product $Al_{13}HX^{-}$ (X=Cl or I), trapped and observed in an FT-ICR mass spectrometer was an intermediate with a large amount of internal energy. In this report, we will demonstrate two dynamic factors that affecting the Al_{13}^{-}+HX reaction and the dissociation of $Al_{13}HX^{-}$, by first principles calculations. First, there is a barrier for both the Al_{13}^{-}+HCl and Al_{13}^{-}+HI reactions. And, second, there is an interesting dynamic process of H migration within $Al_{13}HX^{-}$, which can be considered as a molecular model for the hydrogen diffusion on metal surfaces. The formation and dissociation of $Al_{13}HX^{-}$ therefore provide an example of the dynamic factors that could play an important role in understanding the reactivities of super-atoms like Al_{13}^{-}.

3.2 Computational Details

Optimized structures and energetic values were calculated with the GAUSSIAN 03 package[35]. In the Density Functional Theory (DFT) calculations, two types of functionals were used, B3LYP and BHHLYP. For Al, H and Cl atoms, structural optimization was performed with a 6-31++G** basis set, while single point energies was calculated with a larger basis set of 6-311++G(3df,2p). For iodine atom, the core shells were treated as an effective core potential (ECP), with structural optimization performed with a 6-31G basis set, to which a polarization d function with an exponent of 0.279 and diffuse s and p functions with exponents of 0.0569 and 0.033 were added[36,37]. For single-point energy calculations, the valence basis set for iodine was further augmented by two d functions with exponent values of 0.584 and 0.146 and 1 f function with an exponent of 0.441[36,37]. The nature of an optimized stationary structure was confirmed by the calculation of its vibrational frequencies. For the reaction step between Al_{13}^- and HX, the transition barrier was also calculated at the CCSD level, using the 6-31++G** basis set and the geometry optimized by B3LYP method.

To investigate the hydrogen migration in $Al_{13}HX^-$, we used the DFT based ab initio molecular dynamics (AIMD) method, as implemented in the VASP program[38-41]. The exchange-correlation energy was calculated by the gradient corrected PW91 functional[42], with a plane wave expansion for valence orbitals, and Vanderbilt ultrasoft pseudopotentials for atomic core shells[43-45]. A cluster was put into a periodic box with a size of 15*13*13 Å^3 to minimize the interaction between neighboring cells. Only the Γ-point was sampled in the k-space, while the cutoff energy was 250 eV. An AIMD simulation for a cluster was started with its optimized structure for 20000 steps. The time step was 0.5 fs. The temperature was set to either 500 or 1000 K, as controlled by a Nóse-Hoover thermostat[46,47].

3.3 Results and Discussions

3.3.1 Precursor state and reaction barrier

As shown in Figure 3.1, there were actually two features on the interaction curve between Al_{13}^- and HX: the presence of a "physisorbed" precursor state without chemical bonding interaction between Al_{13}^- and HX, and the presence of a reaction barrier leading to the dissociation of HX and its "chemisorption" on the surface of Al_{13}^-. The barrier for the Al_{13}^-+HCl was higher than that for Al_{13}^-+HI, which indicated an important kinetic reaction factor in the experimental observation that the application of radio frequency pulses was needed for the Al_{13}^-+HCl, but not for Al_{13}^-+HI[7].

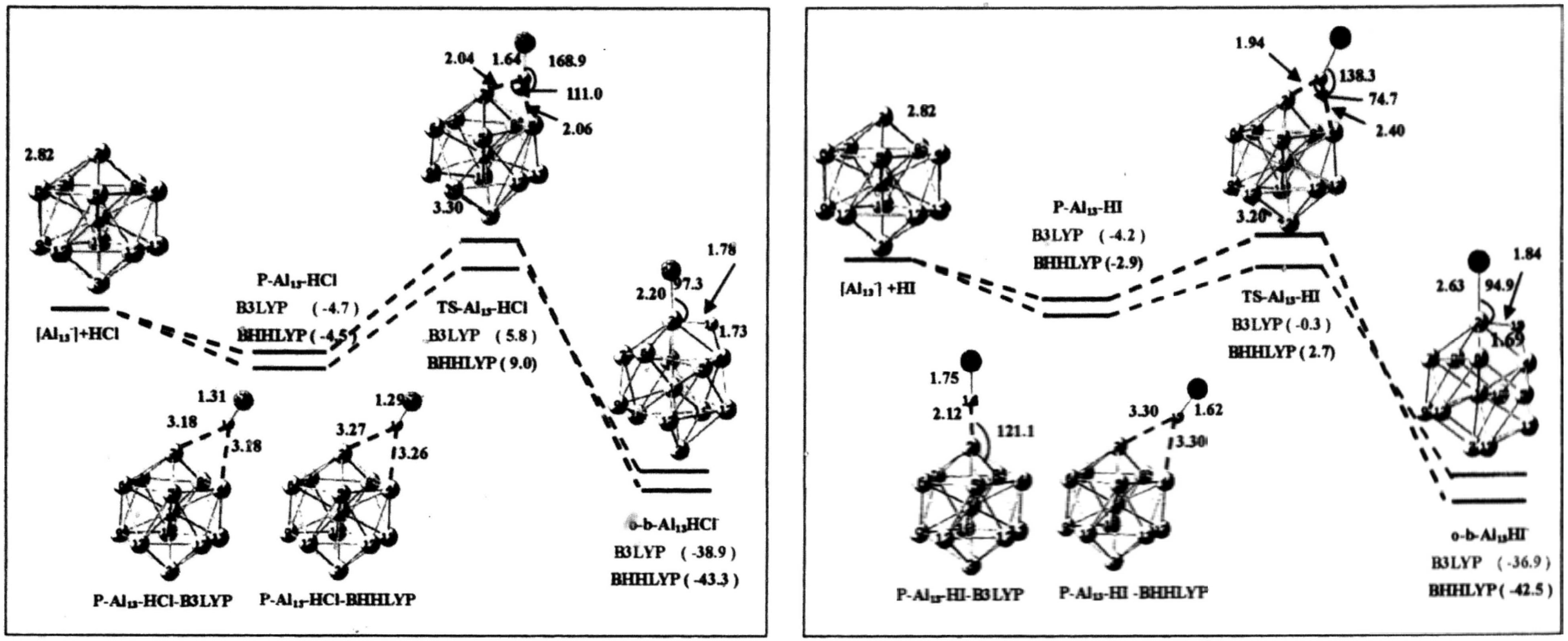

(a) (b)

Figure 3.1 The energy profile for the initial step in the reaction between Al_{13}^- and (a)HCl; (b)HI. The energies in kcal/mol were calculated at either the BHandHLYP/6-311++G(3df,2p)//BHandHLYP/6-31++G** level (black line) or the B3LYP/6-311++G(3df,2p)//B3LYP/6-31++G** level (red line). In the structural labels, we used P as the abbreviation for a precursor state, TS for a transition state, b for a bridge site (between two Al atoms), and o for ortho to indicate the position of H relative to the Cl or I atom. The activation barrier (BHHLYP) was 9.0 kcal/mol for HCl, and only 2.7 kcal/mol for HI. The indicated bond distances were in Å, and bond angles in degree.

In both the precursor state and the transition structure, it was the H end of the HX molecule sitting on a bridge site, i.e., between two Al-Al atoms. This was understandable since the H end of HX was positive and interacted more favorably with the Al_{13}^- anion. From the precursor state to the transition structure, the H...Al distance decreased while the H...X distance increased, which led to the concerted breaking of H...X bond. The produced X atom was bonded to one single Al atom, while the H atom was on a bridge site and bonded to two Al atoms.

For both HCl and HI, the barrier calculated by BHHLYP was higher than that by B3LYP. This was hardly surprising in light of our previous results on Al_{13}^-+O_2 reaction[19], since charge transfer was also involved in these two reactions. It was well-known that many functionals overestimated the extent of charge transfer and underestimated the barrier involved in the process, due to the self-interaction error, which could be partially corrected by mixing more Hatree-Fock exchange into the functional[48-51]. As expected, the barrier was underestimated more in the B3LYP values than in BHHLYP values. Due to the prohibitive computational cost, it was hard to optimize the geometry at post-Hartree-Fock levels. By using the geometry optimized by B3LYP and doing single point energy calculation at the CCSD/6-31++G** level, the barrier relative to well separated Al_{13}^- and HX was raised to 14.9 kcal/mol from 9.0 kcal/mol for HCl and 6.3 kcal/mol from 2.7 kcal/mol for HI. These CCSD values provided a measure of the upper bounds for these barriers. In the case of Al_{13}^-+HI reaction, a transition structure has been identified before with a pure PBE functional, but the barrier was negative relative to well separated Al_{13}^- and HI, and was obviously underestimated[31].

To understand the extent of charge transfer, we did population analysis on the reactants Al_{13}^- and HX, and on the intermediate product $Al_{13}HX^-$. The natural population results were a surprise, producing a negative charge of -1.82 on the central Al atom in Al_{13}^-. It meant that the central Al atom was a sink of negative charge, since not only the single charge on Al_{13}^- was on it, but also it draw further charges away from the other 12 Al atoms. Similar results were obtained for $Al_{13}HX^-$ and reported before for other derivatives[32,52]. Such a charge distribution was an artifact, based on natural bonding orbital analysis (NBO). Four lone pairs were identified on the central Al of Al_{13}^-, occupying one s and three p orbitals in the NBO results, but the occupation number was only 1.3 for each of the p orbitals and 0.9 for the s orbital, significantly lower than the number of 2 expected for a lone pair. Furthermore, out of a total of 85 valence orbitals, 8 non-Lewis orbitals were identified, which clearly indicated that the delocalized metal-metal interactions could not be adequately described by localized natural orbitals.

We also calculated the charge numbers by the Mulliken and the Atomic Polar Tensor (APT) methods. The Mulliken charge on the central Al, as listed in Table 3.1 for the product (o-bridge) $Al_{13}HCl^-$ was +0.29. However, a small change in the $Al_{13}HCl^-$ geometry induced a big change in the charge number, and for the isomeric structures discussed later produced charges on the central Al ranging from -1.4 to +2.8. It was well known that the Mulliken population numbers were sensitive to the basis functions, and the numerical instability was likely due to the fact that the central Al in $Al_{13}HCl^-$ was bonded to 12 Al atoms and a shift in the positions of the basis functions due to even small geometrical changes could induce dramatic change in the calculated population numbers. Only the APT method[53] produced reasonable results, with a charge between -0.4 to -0.6 on the central Al atom for Al_{13}^- and various $Al_{13}HCl^-$ isomers. On the other hand, all population analysis methods were in agreement regarding the transfer of charge to H and Cl in $Al_{13}HCl^-$, with even the H atom being negatively charged, as listed in Table 3.1.

Table 3.1 Charge population of (o-bridge) $Al_{13}HCl^-$ intermediate calculated by B3LYP/631++G** using mulliken population, natural bond order (NBO) analysis and atomic polar tensors (APT).

Atom	Mulliken Charge	NBO Charge	APT Charge
Al(central atom)	0.29	-1.72	-0.58
Al(bonded with H and Cl)	0.18	0.54	0.68
Al	-0.09	-0.03	-0.07
Al	0.01	0.10	-0.03
Al	0.08	0.14	0.02
Al(bonded with H)	-0.06	0.25	0.02
Al	0.03	0.09	-0.05
Al	-0.37	0.10	0.03
Al	-0.22	0.12	0.04
Al	-0.15	0.06	0.01
Al	0.19	0.13	-0.04
Al	-0.14	0.02	-0.05
Al	-0.15	0.09	-0.01
H	-0.10	-0.36	-0.18
Cl	-0.51	-0.56	-0.79

We have already discussed that the B3LYP barriers were lower due to the self-interaction error. For the optimized geometry, the BHHLYP and B3LYP parameters were similar to each other, except in one case, the precursor structure for Al_{13}^-+HI reaction shown in Figure 3.1. With BHHLYP, this structure was similar to the Al_{13}^-...HCl structure. But with B3LYP, the HI molecule was bound to a top Al atom, with an Al–H distance of 2.12 Å, much shorter than the distance of 3.3 Å obtained by BHHLYP. Population analysis indicated significant charge transfer to

HI in the B3LYP precursor structure. This was obviously an artifact due to self-interaction error in B3LYP that overestimated the extent of charge transfer, as also observed in our calculations on $Al_{13}^{-}+O_2$ reaction[19]. Not surprisingly, a similar Al_{13}^{-}...HI structure was reported before, obtained by the pure functional PBE[31].

3.3.2 Migration of H atom

Around 40 kcal/mol of energy was released in the Al_{13}^{-}+HX reaction, which was equivalent to heat the product $Al_{13}HX^{-}$ to a temperature around 1000 K. Although the signals for $Al_{13}HX^{-}$ can be observed in experiment, the hot $Al_{13}HX^{-}$ ions eventually dissociated through two channels: to form $Al_{12}H^{-}$ by the loss of AlCl, or to recover Al_{13}^{-} by the loss of HX[7]. To examine the thermal stability of $Al_{13}HX^{-}$ we performed AIMD simulations at a temperature of 500 and 1000 K, respectively. As shown by the snapshot structures in Figure 3.2 and Figure 3.3, the H atom did not have a fixed position during the AIMD simulation at 1000 K, as it moved along various sites: top site, with H bonded to one Al atom; bridge site, with H bonded between two Al atoms; and hollow site, with H sitting at the center of an Al3 triangle. This dynamic of hydrogen migration can again be understood by considering Al_{13}^{-} as an analog to metal surface. The diffusion of adsorbed H atoms on metal surfaces played a key role in controlling the rates of catalytic reactions, and in the growth of islands and epitaxial layers[54]. At low temperature, such diffusions were dominated by quantum tunneling, which added another dimension to this important problem[55,56]. In $Al_{13}HX^{-}$, we actually had a molecular model for such diffusions that could be measured in the gas phase.

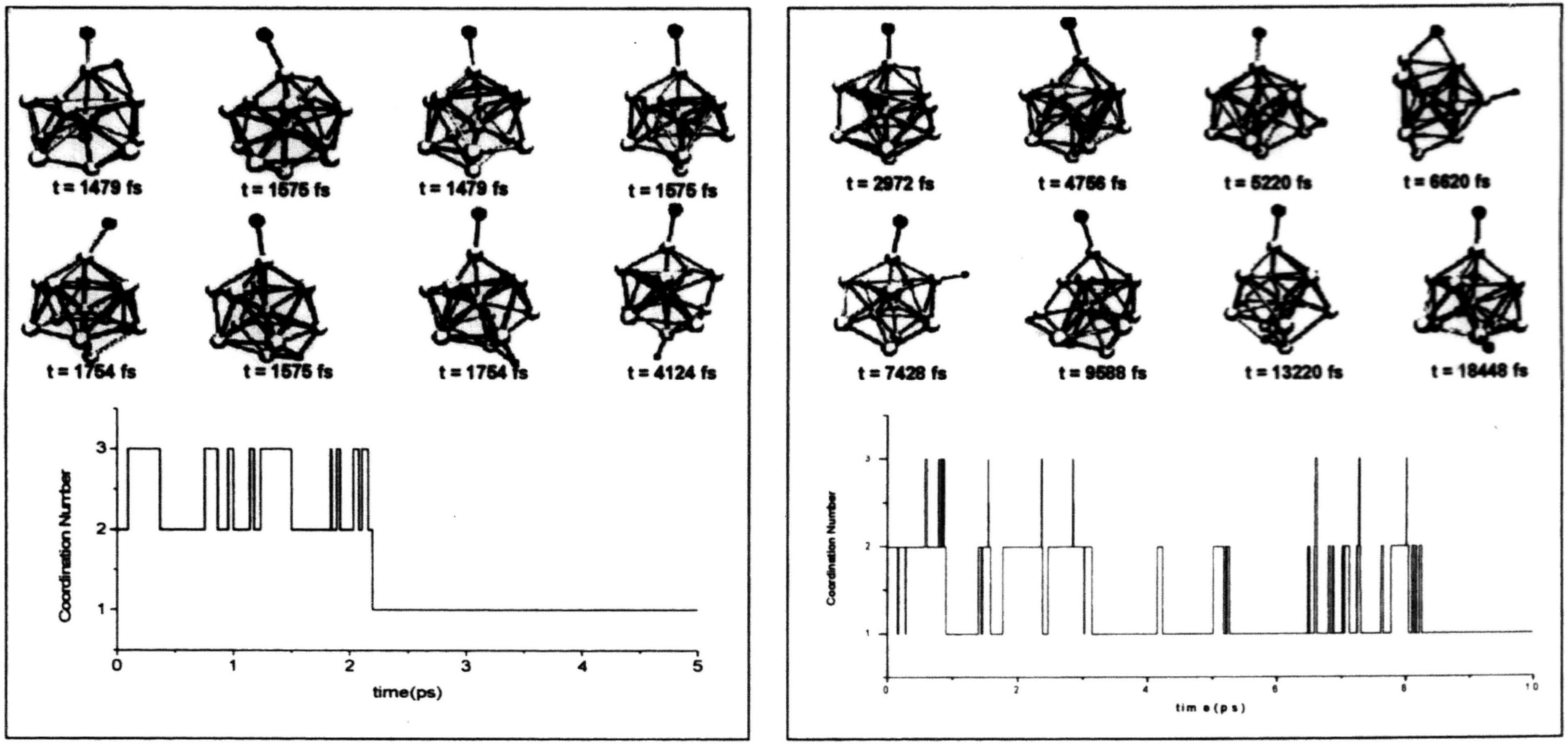

(a)

(b)

Figure 3.2 Snapshots for hydrogen migration and time evolution coordination numbers in $Al_{13}HCl^-$ at (a) 500K and (b) 1000K; and the corresponding time evolutions versus to the coordination number (CN) of H. The CN is defined as the number of Al atoms bonded to H where the Al-H distance is less than 2.2 Å.

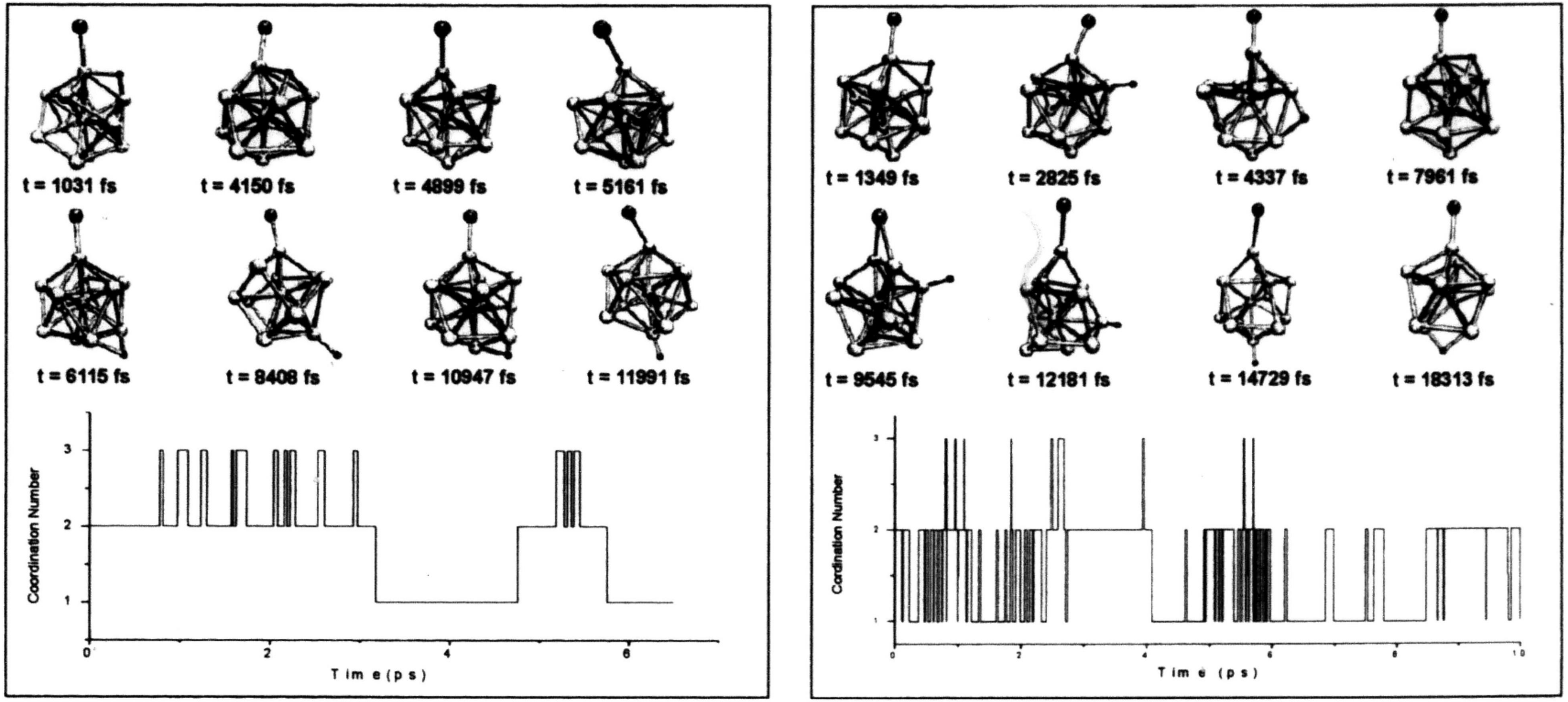

(a) (b)

Figure 3.3 Snapshots for hydrogen migration and time evolution coordination numbers in $Al_{13}HI^-$ at (a) 500K and (b) 1000K; and the corresponding time evolutions versus to the coordination number (CN) of H. The CN is defined as the number of Al atoms bonded to H where the Al-H distance is less than 2.2 Å.

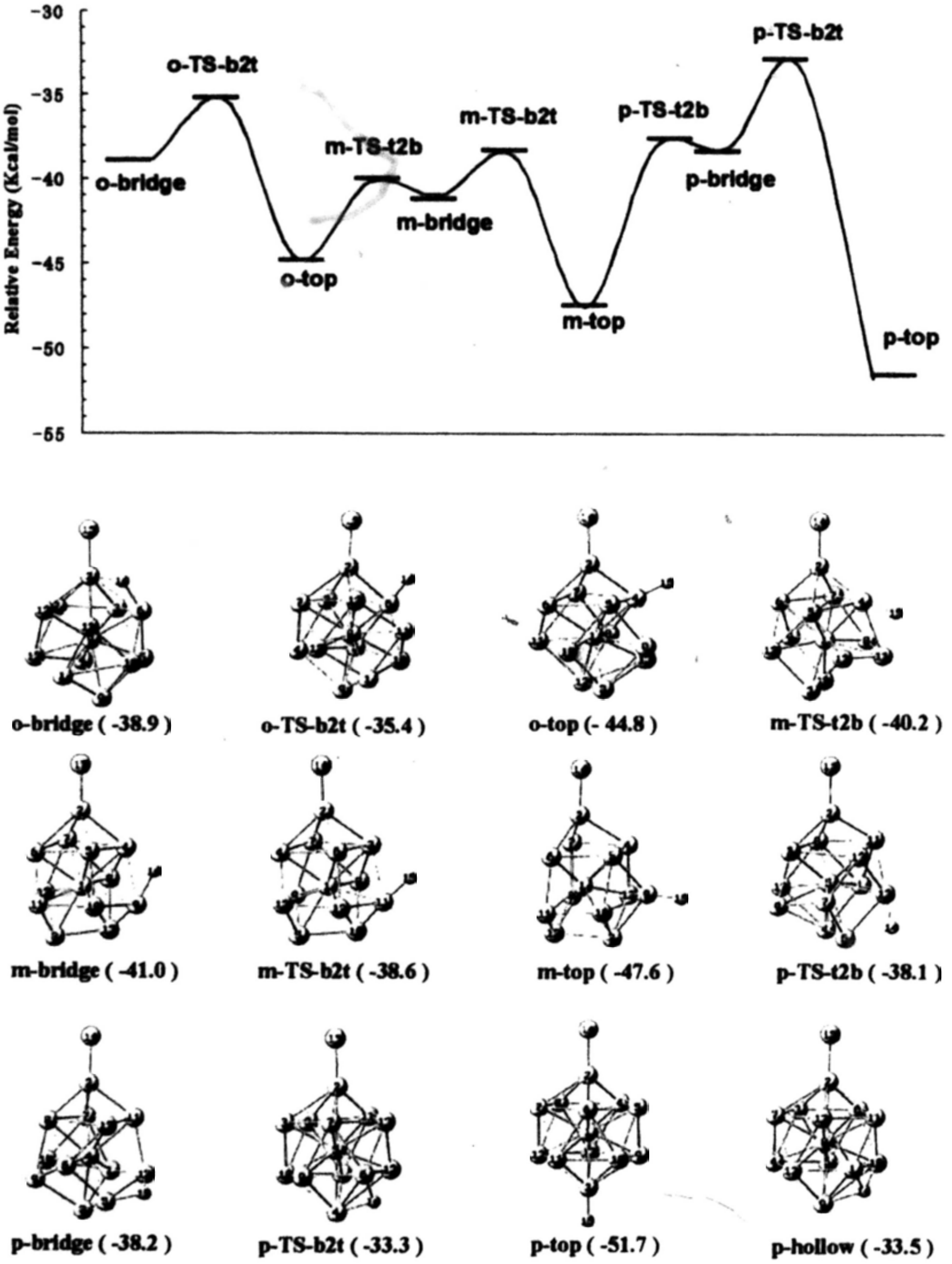

o-bridge (-38.9)
o-TS-b2t (-35.4)
o-top (- 44.8)
m-TS-t2b (-40.2)
m-bridge (-41.0)
m-TS-b2t (-38.6)
m-top (-47.6)
p-TS-t2b (-38.1)
p-bridge (-38.2)
p-TS-b2t (-33.3)
p-top (-51.7)
p-hollow (-33.5)

Figure 3.4 Energy profile for the migration of H atom in $Al_{13}HCl^-$, and the related structures. Numbers in parenthesis were energy values in kcal/mol relative to separated reactants, calculated at the B3LYP/6-311++G(3df,2p)//B3LYP/6-31++G** level.

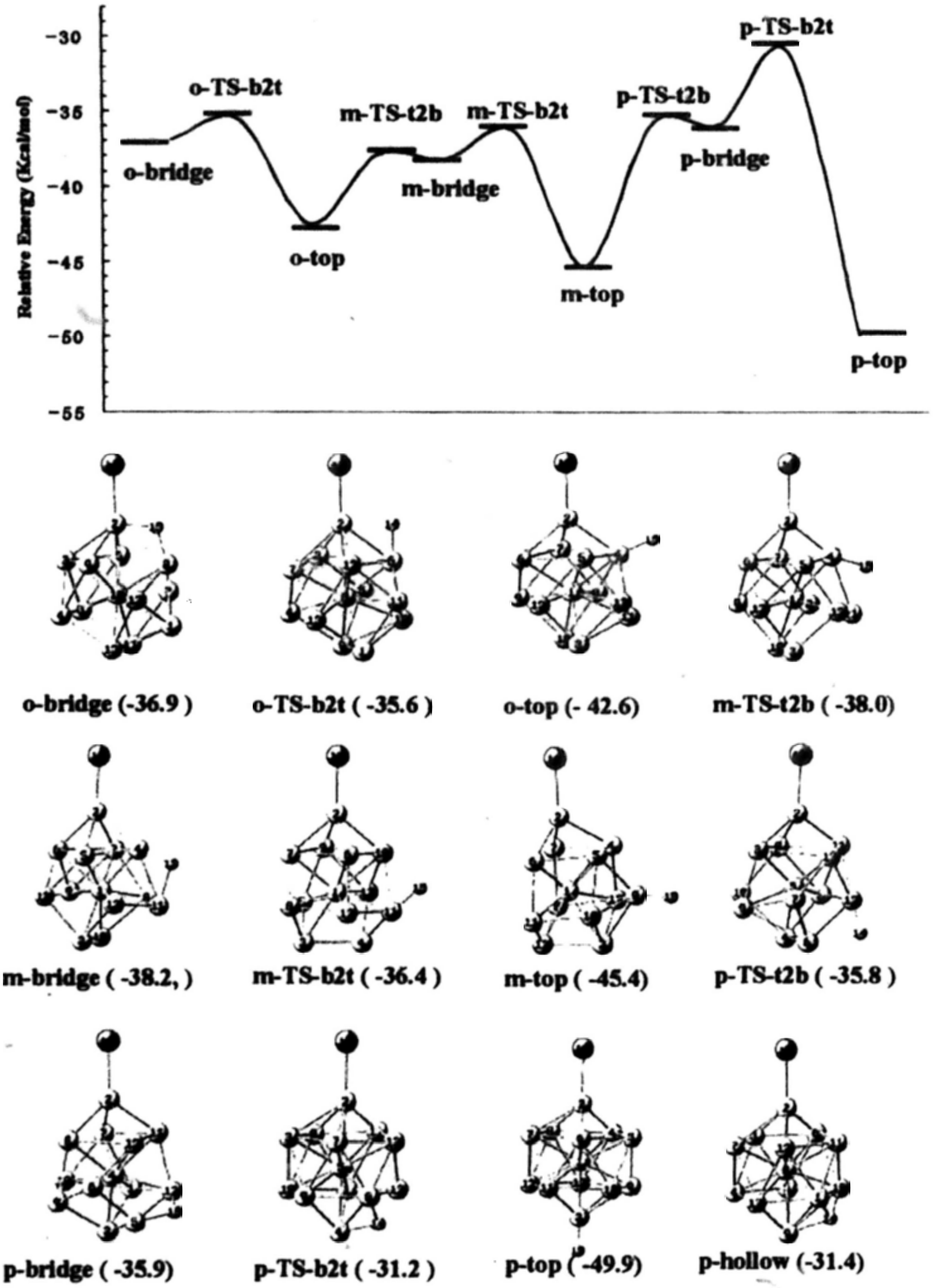

Figure 3.5 Energy profile for the migration of H atom in $Al_{13}HI^-$, and the related structures. Numbers in parenthesis were energy values in kcal/mol relative to separated reactants, calculated at the B3LYP/6-311++G(3df,2p)//B3LYP/6-31++G** level.

As shown in Figure 3.2 to Figure 3.5, there were many stable and transition structures in $Al_{13}HX^-$. All three types of sites, top, bridge, and hollow, have been observed before for H adsorption on Al(111) [57,58]. Within a cluster of $Al_{13}HX^{-}$, each type of these sites can be further characterized by the position of the H atom relative to the halogen atom X, as ortho, meta and para. The structures with H on a top site were the most stable (Figure 3.4 and Figure 3.5). In m-top and o-top structures, the Al_{13} unit was distorted from its ideal symmetric geometry, which indicated significant bonding interaction between the H atom and the specific Al atom and strong perturbation to the bonding among other Al atoms. A high symmetry (C_5 axis) was achieved only in the case of the p-top structure, which was also the most stable structure, since the Al_{13} unit was largely maintained in its original Al_{13}^{-} geometry.

The structures with H on a hollow site were the least favorable energetically. It was also interesting to notice that a H atom on a hollow site produced much less distortion to the symmetric Al_{13} unit than the m-top and o-top sites, while its bonding interaction was shared among three Al atoms. It indicated a weaker bonding interaction between H and Al atoms. The bridge site structures were between the top and hollow sites structures in terms of energy and of the distortion to the Al_{13} unit.

The p-hollow structure in $Al_{13}HCl^{-}$ was the highest in energy among all the structures shown in Figure 3.4 (-33.5 kcal/mol), and its energy difference from the most stable p-top structure (-51.7 kcal/mol) was 17.8 kcal/mol, which was considerably less than the energy produced in the formation of $Al_{13}HCl^{-}$. As shown in Figure 3.4 and Figure 3.5, many transition structures were also identified, and their energies were comparable to those for the bridge and hollow structures. However, it did not mean that bridge and hollow structures were less important in the hydrogen migration dynamics. They were often observed in our AIMD simulations. In one trajectory, simulated at 500 K and started with the initially formed o-bridge structure in Figure 3.2, the H atom proceeded through a number of bridge and hollow sites, and finally settled on the most stable p-top site, without ever passing through an intermediate (ortho or meta) top sites. Again, symmetry was an important consideration since significant distortion in the Al_{13} unit was required for the o-top and m-top structures. The simulated trajectory proceeded along a dynamic path in which the migration of H atom went through the bridge and hollow sites to the p-top site without much perturbation to the symmetry of the Al_{13} unit.

It was also interesting to notice that the barrier separating the o-top and m-top structures at 6.2 kcal/mol was considerably less than the barrier of 14.3 kcal/mol separating the m-top and p-top structures (Figure 3.4) again due to the fact that the Al_{13} unit was distorted in the m-top structure, but symmetric in the p-top structure. The hydrogen migration was therefore affected by dynamic factors, in addition to energetic factors. In addition, the migration of Cl atom was also observed at 1000 K, for which a transition structure was located by geometry optimization and the migration barrier was 19.1 kcal/mol for o-top $Al_{13}HCl^-$. In the AIMD trajectories, Cl migration was much less frequent than H migration due to the heavier mass of Cl.

For H migration in $Al_{13}HCl^-$, the BHHLYP and B3LYP results were in good agreement with each other as shown in Table 3.2. For the relative energy between various intermediates and the barriers separating them, the differences in the calculated values were typically within 2 kcal/mol for the top and bridge structures. This was not surprising, since the H migration process did not involve the kind of significant charge transfer in the initial Al_{13}^-+HCl reaction. The difference increased slightly to around 4 kcal/mol for hollow structures. In fact, all the hollow structures were identified as transition structures with one imaginary frequency in the BHHLYP calculations, although they were stable structures when the B3LYP functional was used.

Table 3.2 Structure parameters and corresponding relative energies for the top, bridge and hollow adsorption intermediates. The involved relative energies are based on B3LYP/6-311++G(3df,2p)//B3LYP/6-31++G** and BHandHLYP/6311++G(3df,2p)// BHandHLYP/6-31++G** calculation results. The mentioned RE refer to the energy relative to p-top intermediate. (unit: kcal.mol^{-1} for energy, angstrom for bond distance)

Intermediates	Al-Cl bond		Al-H bond		RE	
	B3LYP	BHHLYP	B3LYP	BHHLYP	B3LYP	BHHLYP
p-top	2.18	2.16	1.59	1.57	0.0	0.0
m-top	2.19	2.17	1.60	1.58	4.1	2.3
o-top	2.19	2.17	1.59	1.58	6.9	6.2
p-bridge	2.19	2.17	1.83 1.75	1.83 1.73	13.5	15.4
m-bridge	2.19	2.17	1.84 1.75	1.83 1.74	10.7	10.6
o-bridge	2.20	2.18	1.79 1.73	1.89 1.70	12.8	14.7
p-hollow	2.20	2.18	2.10 1.90 1.90	2.17 1.86 1.86	18.2	22.1
m-hollow	2.20	2.18	1.95 1.94 1.94	1.94 1.93 1.91	17.0	21.6
o-hollow	2.20	2.18	1.97 1.96 1.94	1.96 1.95 1.79	14.0	17.6

3.3.3 The dissociation of $Al_{13}HX^-$

The dissociation of $Al_{13}HX^-$ was determined by the balance of two channels, the loss of AlX to form $Al_{12}H^-$ versus the loss of HX back to Al_{13}^-, which was an important consideration in understanding the experimental results[7]. The HX loss channel passed through the same transition structure in the formation of $Al_{13}HX^-$ (see

Figure 3.1), while the AlX loss channel was an exothermic dissociation without a transition structure with dissociation energy shown in Table 3.3. The HX loss channel must also pass through the intermediate o-bridge $Al_{13}HX^-$. In the case of o-bridge $Al_{13}HCl^-$, the activation energy was 52.3 kcal/mol for HCl loss, and 42.0 kcal/mol for AlCl loss, both calculated by the BHHLYP functional. In the case of o-bridge $Al_{13}HI^-$, the activation energy was 45.2 kcal/mol for HI loss, and 43.5 kcal/mol for AlI loss. Therefore with the reaction barrier included into consideration, the AlCl loss channel was favored over the HCl loss channel by 10 kcal/mol for $Al_{13}HCl^-$, while the AlI loss channel was also favored for $Al_{13}HI^-$, although the difference in activation energy between the two channels was only 1.7 kcal/mol.

This picture was slightly changed when B3LYP functional was employed. For the AlX loss channel, the reaction energies calculated by B3LYP and BHHLYP methods were in very good agreement with each other, within 2 kcal/mol. (Table 3.3) However, the activation energy calculated by B3LYP method was 44.7 kcal/mol for the loss of HCl in $Al_{13}HCl^-$ and 37.2 kcal/mol for the loss of HI in $Al_{13}HI^-$ (see Figure 3.1), both lowered by 8 kcal/mol compared to the BHHLYP values, since B3LYP method underestimated the barrier for charge transfer, and the B3LYP calculated reaction energy was also lower. But even with the B3LYP values for $Al_{13}HCl^-$, the barrier for the loss of HCl was still slightly higher than that for the loss of AlCl. It was in the case of $Al_{13}HI^-$, that the AlI loss channel was predicted as more favorable than the HI loss channel by the B3LYP values.

More importantly, hydrogen migration had a big effect on the dissociation of $Al_{13}HX^-$. The HX loss channel was only accessible through the o-bridge structures. But with the large amount of energy deposited during the formation of $Al_{13}HX^-$, the o-bridge structures were present for only a small fraction of the time, as H migrated among various adsorption sites. For all the other structures, only AlX loss channel was accessible. In other words, AlX loss channel was significantly favored by the entropy factor, due to the extensive hydrogen migration. The dissociation energies, as listed in Table 3.3, were correlated with the stability of each structure. For example, the largest dissociation energy was required for the most stable p-top structure, and the dissociation energy for bridge structures was generally smaller than that for the top structures.

Table 3.3 Dissociation energies for top(t), bridge(b) and hollow(h) adsorption intermediates. Energies are calculated by B3LYP/6-311++G(3df,2p)// B3LYP/6-31++G** and BHandHLYP/6-311++G(3df,2p)//BHandHLYP/6-31++G** methods. (unit: kcal.mol^{-1})

intermediate		Dissociation energies	
		B3LYP	BHHLYP
t-$Al_{13}HCl^-$	o-$Al_{13}HCl^-$	48.8	48.0
	m-$Al_{13}HCl^-$	48.5	48.1
	p-$Al_{13}HCl^-$	50.9	51.2
b-$Al_{13}HCl^-$	o-$Al_{13}HCl^-$	42.9	44.6
	m-$Al_{13}HCl^-$	46.0	48.6
	p-$Al_{13}HCl^-$	42.0	41.9
t-$Al_{13}HI^-$	o-$Al_{13}HI^-$	50.3	49.6
	m-$Al_{13}HI^-$	49.9	49.7
	p-$Al_{13}HI^-$	52.8	53.1
b-$Al_{13}HI^-$	o-$Al_{13}HI^-$	44.6	42.6
	m-$Al_{13}HI^-$	47.4	46.8
	p-$Al_{13}HI^-$	43.4	43.4

3.4 Conclusion

We demonstrated that Al_{13}^-+HCl reaction has similar reaction mechanism with HCl reaction on Al(111) surface. The kinetic energy required to promote the reaction in experiment was due to the presence of a reaction barrier. Furthermore, the hydrogen in the $Al_{13}HX^-$ intermediate could move from one site to another, in analogy to the diffusion of hydrogen on metal surfaces. These dynamic factors make Al_{13}^- a fascinating model to probe the dynamic aspect of surface reactions, which should be an important consideration in the reactivity of other metal clusters.

One the other hand, Al_{13}^- reaction with HCl has its own characteristics, which is different from Al(111) surface. The HCl adsorption on Al_{13}^- cluster results into large distortion due to the relaxation of the cluster. However, little distortion can be observed for Al(111) surface due to the constraint of boundary conditions.

3.5 Reference

[1] Burgert, R.; Schnockel, H. *Chem. Comm.* **2008**, 2075-2089.

[2] Jarrold, M. F.; Bower, J. E.; Kraus, J. S. *J. Chem. Phys.* **1987**, 86, 3876-3885.

[3] Kaya, K.; Fuke, K.; Nonose, S.; Kikuchi, N. *Zeitschrift Fur Physik D-Atoms Mol. and Clusters* **1989**, 12, 571-573.

[4] Leuchtner, R. E.; Harms, A. C.; Castleman, A. W. *J. Chem. Phys.* **1991**, 94, 1093-1101.

[5] Rao, B. K.; Jena, P. *J. Chem. Phys.* **1999**, 111, 1890-1904.

[6] Schultz, N. E.; Staszewska, G.; Staszewski, P.; Truhlar, D. G. *J. Phys. Chem. B* **2004**, 108, 4850-4861.

[7] Burgert, R.;Stokes, S. T.; Bowen, K. H.; Schnockel, H. *J. Am. Chem. Soc.* **2006**, 128, 7904-7908.

[8] Burgert, R.;Schnockel, H.; Olzmann, M.; Bowen, K. H. *Angewandte Chemie-Int. Edition* **2006**, 45, 1476-1479.

[9] Knight, W. D.; Clemenger, K.; Deheer, W. A.; Saunders, W. A.; Chou, M. Y.; Cohen, M. L. *Phys. Rev. Lett.* **1984**, 52, 2141-2143.

[10] Martin, T. P.; Bergmann, T.; Gohlich, H.; Lange, T. *Chem. Phys. Lett.* **1990**, 172, 209-213.

[11] Castleman, A. W.; Khanna, S. N. *J. Phys. Chem. C* **2009**, 113, 2664-2675.

[12] Gong, X. G.; Sun, D. Y.; Wang, X. Q. *Phys. Rev. B* **2000**, 62, 15413-15416.

[13] Khanna, S. N.; Jena, P. *Chem. Phys. Lett.* **1994**, 219, 479-483.

[14] Khanna, S. N.; Jena, P. *Phys. Rev. Lett.* **1992**, 69, 1664-1667.

[15] Bergeron, D. E.; Roach, P. J.; Castleman, A. W.; Jones, N.; Khanna, S. N. *Science* **2005**, 307, 231-235.

[16] Bergeron, D. E.; Castleman, A. W.; Morisato, T.; Khanna, S. N. *Science* **2004**, 304, 84-87.

[17] Leuchtner, R. E.; Harms, A. C.; Castleman, A. W. *J. Chem. Phys.* **1989**, 91, 2753-2754.

[18] Burgert, R.;Schnockel, H.; Grubisic, A.; Li, X.; Stokes, S. T.; Bowen, K. H.; Gantefor, G. F.; Kiran, B.; Jena, P. *Science* **2008**, 319, 438-442.

[19] Yuan, Q. H.; Li, J. B.; Fan, X. L. Lau, W. M.; Liu, Z. F. *Phys. Rev. B* submitted,.

[20] Osterlund, L.; Zoric, I.; Kasemo, B. *Phys. Rev. B* **1997**, 55, 15452-15455.

[21] Komrowski, A. J.; Sexton, J. Z.; Kummel, A. C.; Binetti, M.; Weisse, O.; Hasselbrink, E. *Phys. Rev. Lett.* **2001**, 8724, 246103.

[22] Brune, H.; Wintterlin, J.; Trost, J.; Ertl, G.; Wiechers, J.; Behm, R. J. *J. Chem. Phys.* **1993**, 99, 2128-2148.

[23] Schmid, M.; Leonardelli, G.; Tscheliessnig, R.; Biedermann, A.; Varga, P. *Surf.*

Sci. **2001**, 478, L355-L362.

[24] Honkala, K.; Laasonen, K. *Phys. Rev. Lett.* **2000**, 84, 705-708.

[25] Yourdshahyan, Y.; Razaznejad, B.; Lundqvist, B. I. *Solid State Comm.* **2001**, 117, 531-535.

[26] Yourdshahyan, Y.; Razaznejad, B.; Lundqvist, B. I. *Phys. Rev.* B **2002**, 65, 075416.

[27] Hellman, A.; Razaznejad, B.; Yourdshahyan, Y.; Ternow, H.; Zoric, I.; Lundqvist, B. I. *Surf. Sci.* **2003**, 532, 126-131.

[28] Ciacchi, L. C.; Payne, M. C. *Phys. Rev. Lett.* **2004**, 92, 176104.

[29] Behler, J.; Delley, B.; Lorenz, S.; Reuter, K.; Scheffler, M. *Phys. Rev. Lett.* **2005**, 94, 036104.

[30] Roach, P. J.; Woodward, W. H.; Castleman, A. W.; Reber, A. C.; Khanna, S. N. *Science* **2009**, 323, 492-495. 12

[31] Kim, J. C.; Kim, K. H.; Jung, J.; Han, Y. K. *J. Comp. Chem.* **2008**, 29, 1626-1631.

[32] Sun, J.;Lu, W. C.; Zhao, L. Z.; Zhang, W.; Li, Z. S.; Sun, C. C. *J. Phys. Chem. A* **2007**, 111, 4378-4383.

[33] Jones, N. O.; Reveles, J. U.; Khanna, S. N.; Bergeron, D. E.; Roach, P. J.; Castleman, A. W. *J. Chem. Phys.* **2006**, 124, 154311.

[34] Bergeron, D. E.; Castleman, A. W.; Morisato, T.; Khanna, S. N. *J. Chem. Phys.* **2004**, 121, 10456-10466.

[35] Frisch, M. J. et *al. Gaussian 03, Revision A.1*; Gaussian, Incorporated: Pittsburgh, PA, **2003**.

[36] Wadt, W. R.; Hay, P. J. *J. Chem. Phys.* **1985**, 82, 284-298.

[37] Glukhovtsev, M. N.;Pross, A.; McGrath, M. P.; Radom, L. *J. Chem. Phys.* **1995**,

103, 1878-1885.

[38] Kresse, G.; Furthmuller, J. *Phys. Rev. B* **1996**, 54, 11169-11186.

[39] Kresse, G.; Hafner, J. Phys. Rev. *B* **1993**, 47, 558-561.

[40] Kresse, G.; Hafner, J. Phys. Rev. *B* **1994**, 49, 14251-14269.

[41] Kresse, G.; Furthmuller, *J. Comp. Mater. Sci.* **1996**, 6, 15-50.

[42] Perdew, J. P. Unified Theory of Exchange and Correlation Beyond the Local Density Approximation. In *Electronic Structure of Solids'91* ; Ziesche, P.; Eschrig, H., Eds.; Academic Verlag: Berlin, **1991**.

[43] Vanderbilt, D. *Phys. Rev. B* **1990**, 41, 7892-7895.

[44] Kresse, G.; Hafner, J. *Phys. Rev. B* **1993**, 48, 13115-13118.

[45] Kresse, G.; Hafner, J. *Phys. Rev. B* **1994**, 49, 14251-14269.

[46] Nosé, S. *J. Chem. Phys.* **1984**, 81, 511.

[47] Hoover, W. *Phys. Rev. A* **1985**, 31, 1695.

[48] Ruiz, E.; Salahub, D. R.; Vela, A. *J. Phys. Chem.* **1996**, 100, 12265-12276.

[49] Zhang, Y. K.; Yang, W. T. *J. Chem. Phys.* **1998**, 109, 2604-2608.

[50] Karpfen, A. *J. Phys. Chem. A* **2000**, 104, 6871-6879.

[51] Grafenstein, J.; Kraka, E.; Cremer, D. *J. Chem. Phys.* **2004**, 120, 524-539.

[52] Rao, B. K.; Khanna, S. N.; Jena, P. *Phys. Rev. B* **2000**, 62, 4666-4671.

[53] Cioslowski, J. *Phys. Rev. Lett.* **1989**, 62, 1469-1471.

[54] Ala-Nissila, T.; Ferrando, R.; Ying, S. C. *Adv. in Phys.* **2002**, 51, 949-1078.

[55] Sundell, P. G.; Wahnstrom, G. *Phys. Rev. Lett.* **2004**, 92, 155901.

[56] Sun, Y. C.; Voth, G. A. *J. Chem. Phys.* **1993**, 98, 7451-7458.

[57] Stumpf, R. *Phys. Rev. Lett.* **1997**, 78, 4454-4457.

[58] Go, E. P.; Thuermer, K.; Reutt-Robey, J. E. *Surf. Sci.* **1999**, 437, 377-385.

Chapter Four

New Insights on Hydrogen Desorption Dynamics from Hydrogenated Si(100) Surface

4.1 Introduction

The interaction of hydrogen with silicon surfaces has long been the subject of extensive experimental and theoretical research[1-6]. The great interest in the subject is partly due to the importance of H/Si in semiconductor chemistry[7], and more important is that hydrogen on silicon is a promising model system for studying general aspects of chemical reactions on covalent surfaces[8]. Although it is a simple system, investigations about its reaction mechanisms, especially desorption mechanisms, has been pursued for several decades. Studies were mainly focused on two aspects: the unexpected first order desorption kinetics; and the so-called "barrier puzzle"[7,9,10].

The "barrier puzzle" refers to the observation that desorbed molecules seemed not to follow reversely the same pathway as they took in adsorption. Experimentalists found that the sticking probability for the dissociative adsorption of H_2 on a clean Si(100) surface was very small at room temperature[11], suggesting a high adsorption barrier, but it increased dramatically with higher surface temperatures. On the other hand, the nearly thermally distributed kinetic energy of desorbing molecules led to the conclusion that the molecules transversed almost no adsorption barrier[9]. Despite much experimental and theoretical effort, there are still unresolved issues related to the microscopic mechanisms and the dynamics of desorption.

It is well-known that a clean Si(100) surface undergoes (2 × 1) reconstruction to produce parallel rows of dimers. With the addition of H atoms onto Si(100), the H/(Si100) surface system could take a periodic structure with a 2 × 1 (the unit cell has 2 Si atoms along silicon dimer direction and 1 Si atom vertical dimer direction), 3 × 1 (the unit cell has 3 Si atoms along silicon dimer direction and 1 Si atom vertical dimer direction), or 1 × 1 (the unit cell has 1 Si atom along silicon dimer direction and 1 Si atom vertical dimer direction) phase (Figure 4.1 (a)). In clean Si(100) surface, each surface Si atom has one dangling bond, and saturation of these dangling bonds with H atom leads to (2 × 1) monohydride surface. Further H adsorption breaks the Si-Si dimer bond and each surface Si is bonded with two H atoms, forming a (1 × 1) dihydride surface. There also exists an intermediate (3 × 1) phase in which rows of monohydride dimers are interplaced with rows of dihydrides.

The three H/Si(100) surfaces together with clean Si(100) surface can be converted mutually through the adsorption or desorption of hydrogen upon heating. The (1 × 1) dihydride surface (H/Si(100)-(1 × 1)) can be transformed to (2 × 1) monohydride surface (H/Si(100)-(2 × 1)), by desorbing a H_2 molecule from two adjacent dihydrides, which will be called "dihydride desorption" (see Figure 4.1(b)). The resulting monohydride surface can be further converted to clean Si(100) surface through a "monohydride desorption" (see Figure 4.1(b)) by desorbing another H_2

molecule from a single dimer. On a (3 × 1) surface, it has been suggested that H atoms could switch their positions and produce a configuration with two adjacent dihydrides, which makes it possible for the dihydride desorption on a (3×1) surface[12].

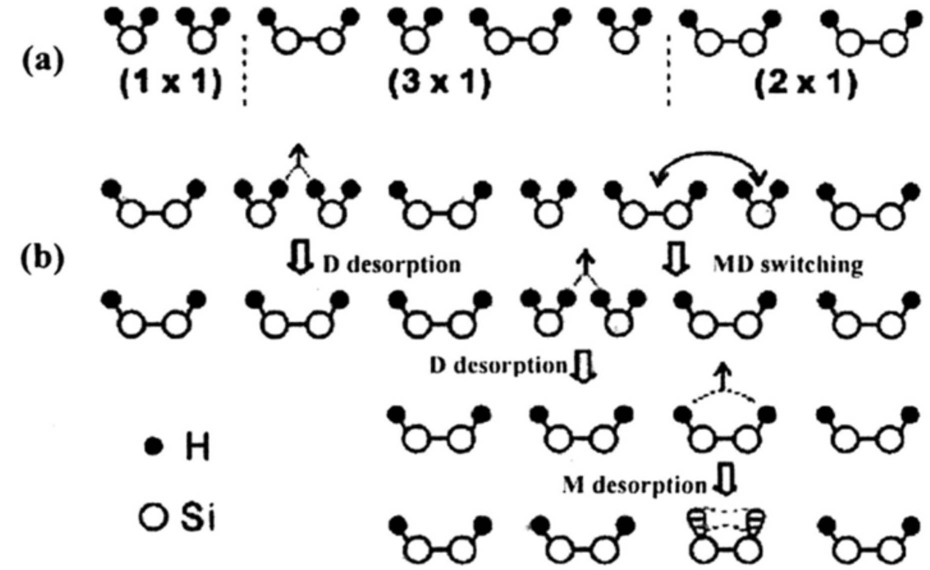

Figure 4.1 Schematic diagrams showing (a) side views of (1 × 1) dihydride, (2 × 1) monohydride, and (3 × 1) mixed monohydride-dihydride phases, (b) side views of atomic configurations involved in "dihydride(D) desorption", "monohydride(M) desorption" and "monohydride dihydride(MD) switching" reactions.

All three types of conversion processes have been observed in STM experiments[12]. But in temperature-programmed desorption (TPD) studies only two desorption peaks were identified[9,13], as shown in Figure 4.2. The peak around 680 K (β_2) corresponded to the dihydride desorption, converting two dihydride to a single monohydride dimer. The other peak around 790 K (β_1) corresponded to the monohydrides desorption, in which a monohydride surface was converted to a clean Si(100)-(2 × 1). Furthermore, the β_2 peak was identical for both the (1 × 1) and the

(3 × 1) surfaces, indicating that the barrier for the switching of H atoms between monohydride and dihydride structures on a (3 × 1) surface was lower than the dihydride desorption barrier and therefore did not play a significant role in the desorption kinetics.

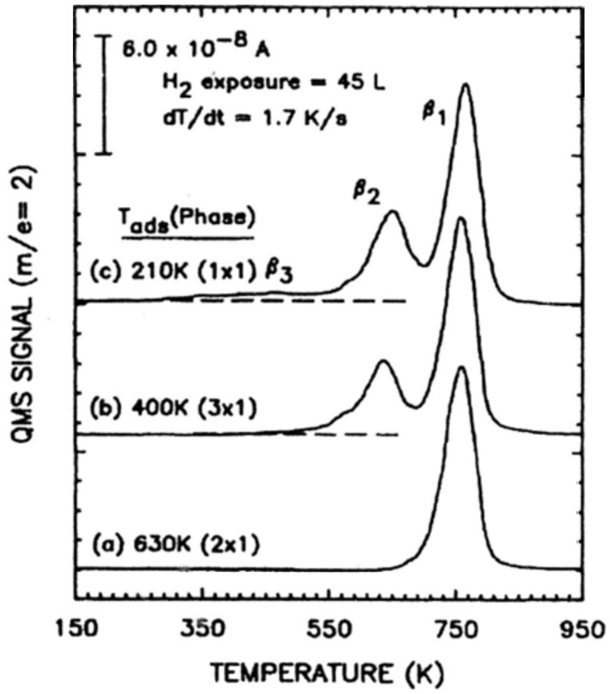

Figure 4.2 Temperature-programmed-desorption (TPD) spectra of H_2 desorption obtained from H-saturated Si(100) formed at different adsorption temperatures. (a) 630K (2 × 1), (b) 400K (3 × 1), (c) 210K (1 × 1). TPD spectra were taken with a heating rate of 1.7K/s after the crystal was cooled down to 130K. Data copy from reference [9].

The mechanism for the monohydride desorption has been a subject of debate, addressed in many theoretical studies[8,14-16]. Assuming that defects do not play a prominent role in a well prepared monohydride Si(100) surface, there are two types of mechanisms: 1) interdimer mechanism, with the desorbing hydrogen molecule formed by two hydrogen atoms from two adjacent silicon dimmers; 2) intradimer mechanism, with the hydrogen molecule formed by the two H atoms on a single silicon dimer)[14]. The intradimer mechanism was favored initially, due to the observation of naked Si dimers in STM experiments and the fact that it offered a straightforward explanation for the observed first-order desorption kinetics. However, later calculations demonstrated that the desorption barrier for the interdimer pathway was actually lower[17,18]. Moreover, strong experimental evidences in favor of the interdimer pathway were also reported[5,13]. By heating monohydride Si(100) surface with nanosecond laser, the STM images for the desorption sites showed a clear predominance of the interdimer processes[5]. The observation of the more stable naked Si dimer in previous TPD experiments was attributed to the diffusion of H atoms after interdimer desorption, since the diffusion barrier was lower than the desorption barrier. The interdimer desorption sites could only be observed after the pulsed and localized laser heating, which suppressed the H diffusion after desorption. It was also possible that both mechanisms played a role in the desorption, based on the fitting for the kinetic measurement[19].

In contrast to hydrogen desorption from monohydride surface where a first order desorption kinetics was observed, hydrogen desorption from dihydride surface follow a second-order kinetic behavior[20-22]. There were two different mechanisms proposed to explain this desorption behavior. The first one was the recombinative 1,2-elimination mechanism[1,23], in which each dihydride donated one hydrogen atom to recombinatively desorb from the surface concertedly. The other one was the l,l-elimination mechanism[20-22,24-25]. In this mechanism, two H atoms on a single silicon atom were desorbed and a bridge-structure intermediate was identified.

The mechanism for the switching between monohydride and dihydride on 3×1 surfaces has not been investigated to our best knowledge.

The silicon dimer on a clean Si(100) surface has often been treated as analogous to a double bond between two carbon atoms. However, recent works have shown that the chemistry of silicon surface had its unique aspects. For example, a [2+2] concerted addition, ruled out as symmetry forbidden according to the Woodward-Hoffman rule, was actually accessible on a surface silicon dimer due to the crossing of Fermi surface by electronic bands[26]. Also, in the addition of C_2H_2, the attack on the bond between a surface Si and a backbone Si[27] was actually more favorable than the addition to the dimer bond. After all, Si was not exactly the same as C. It was known that H occupied a bridge position in the most stable isomer for Si_2H_2, unlike C_2H_2[43]. In this chapter, we demonstrate that such a bridge structure also plays a significant role in the hydrogen desorption on hydrogenated Si(100) surface, and especially in the H switching process.

4.2 Computational details

First principle calculations on the total energy and electronic structure were carried out within density functional theory (DFT), using a planewave basis set and pseudopotentials for the atomic core regions, as implemented in the Vienna ab initio simulation package (VASP). The setup was similar to previous studies in our group on Si(100) reactions[26-28], with PW91 GGA (general gradient approximation) exchange-correlation functional, Vanderbilt ultrasoft pseudopotentials, and a cutoff energy of 300 eV for the planewave basis set. The Si(100)-2×1 and Si(100)-1×1 surfaces were modeled by a p(2 × 2) slab, with a unit cell of the size 7.7 ×7.7 × 17.50 Å^3 containing five Si layers and a vacuum region of 10 Å. The Si(100)-3×1 surface was modeled by a unit cell of the size 11.56 ×11.56 × 17.50 Å^3 which also contained five Si layers and a vacuum region of 10 Å. All the bottom silicon atoms were saturated by H atoms. The sampling for the Brillouin zone included a set of eight special k-points.

The minimum energy reaction path was mapped out by the Nudged Elastic Band method, developed by Jónsson and co-workers[29-31]. Vibrational frequencies were also calculated to verify the transition structures, using the dynamic matrix method.

4.3 Results and discussion

4.3.1 Intradimer monohydride desorption

We first investigated the intradimer desorption pathway at $\theta_H = 1.0$ML , with each surface Si atom bonded to one H atom. Unlike previous studies which found the intradimer desorption as a concerted reaction, we identified the intradimer desorption as a stepwise reaction (Figure 4.3). In the first step, the Si-Si σ bond in HSi-SiH unit was broken and one of the hydrogen atoms moved to a bridge position between two Si atoms, forming an intermediate (LM) structure with a 3-atomic-centers-2-electrons (3c-2e) Si-H-Si bond. This step must overcome a barrier of 1.48eV, with an overall energy change of 1.4eV. This bridge intermediate was unstable, as it can be readily reversed back to the react reactant (R). It could also lead to desorption of hydrogen molecule, after overcoming an energy barrier of 1.09eV energy. The desorption product (P) was 2.0eV higher in energy than the initial reactant(R). The two reaction barriers added to 2.49eV, which was close to previous DFT slab model calculation results[19,32-36].

Intradimer desorption pathway at θ_H=0.5ML, with only half of the surface Si-Si dimers saturated with hydrogen atoms, was also explored. The desorption pathway was similar to that for the 1.0ML surface, as shown in Figure 4.4, although energetics were slightly different. The first activation barrier was 1.55eV and the bridge intermediate was only 1.27eV higher than the reactant. The total activation barrier was 2.32eV, which was slightly lower than the value of 2.49eV for the 1.0 ML surface.

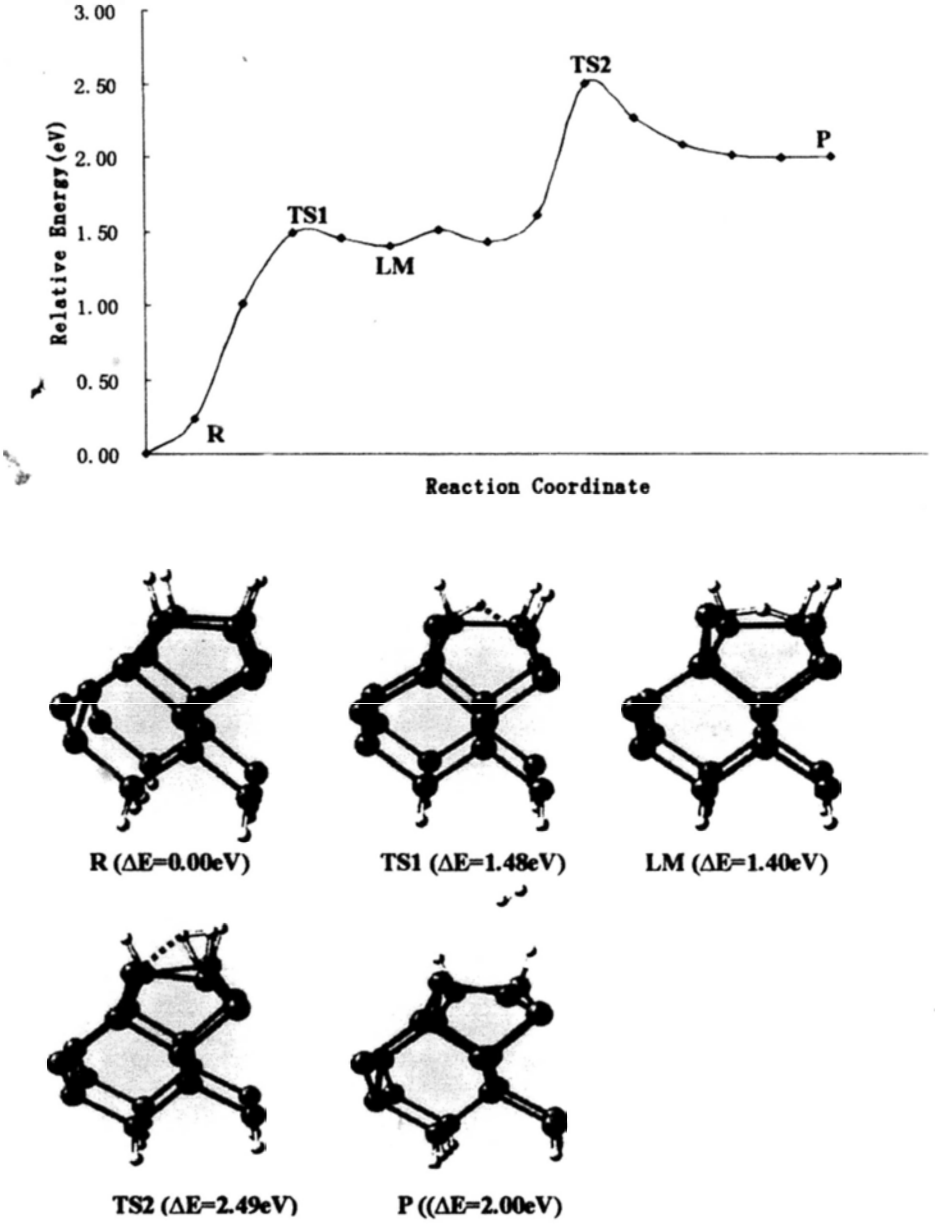

R (ΔE=0.00eV)

TS1 (ΔE=1.48eV)

LM (ΔE=1.40eV)

TS2 (ΔE=2.49eV)

P ((ΔE=2.00eV)

Figure 4.3 Desorption channel for intradimer at high coverage (1.0ML). This desorption can be viewed as a stepwise reaction and an intermediate (labled as LM) with short life-time has been formed. The Si-Si σ bond in HSi-SiH unit was broken and one of the hydrogen atoms moved to the neighbor silicon atom, forming an intermediate structure with 3c-2e (Si-H-Si bridge) bond. The bond break of the Si-Si σ bond and the formation of the Si-H-Si 3c-2e leave a lone pair electrons on one silicon atom. The formation of LM needs overcome an activation barrier about 1.48eV and with reaction heat about 1.40eV. This LM can be further activated to desorption product (labeled as P) with 1.09eV energy.

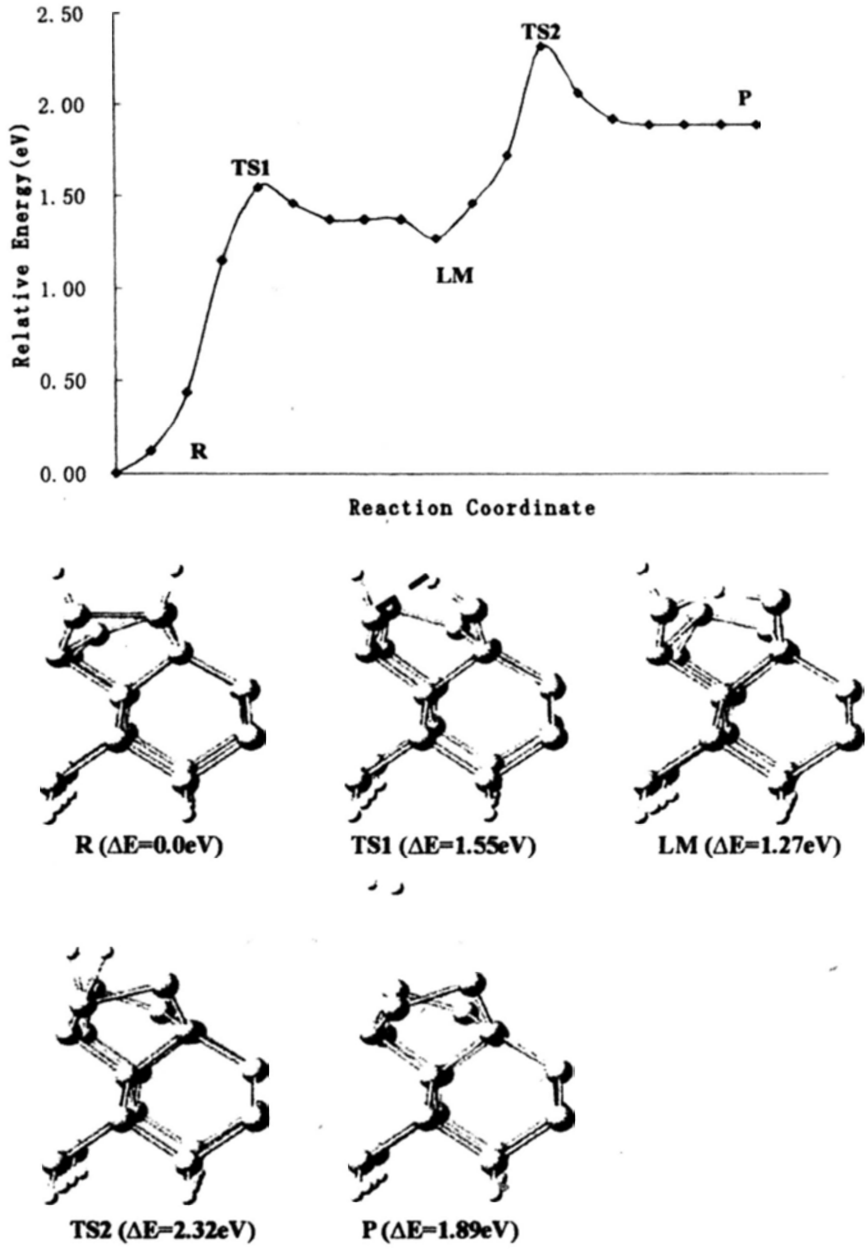

R (ΔE=0.0eV) TS1 (ΔE=1.55eV) LM (ΔE=1.27eV)

TS2 (ΔE=2.32eV) P (ΔE=1.89eV)

Figure 4.4 Desorption channel for intradimer at low coverage (0.5ML). This desorption process is similar to that of intradimer at high coverage (1.0ML) but the activation barrier is slightly different. The first activation barrier is 1.55eV and the total activation barrier is 2.32eV.

4.3.2 Interdimer monohydride desorption

Interdimer desorption pathway at high coverage (1.0ML) shown in Figure 4.5 has been identified by previous studies as the most favorable, with the lowest activation barrier in all suggested channels. The desorption barrier found in our calculations was 2.20 eV, similar to previous calculation results [19,32-36]. For the reverse adsorption process, there was no barrier, and therefore a desorbed hydrogen molecule should have nearly zero translational energy, in agreement with experimental observations very well. For the adsorption process, the two dangling bonds on the adjacent silicon dimers obviously facilitated the dissociation of hydrogen.

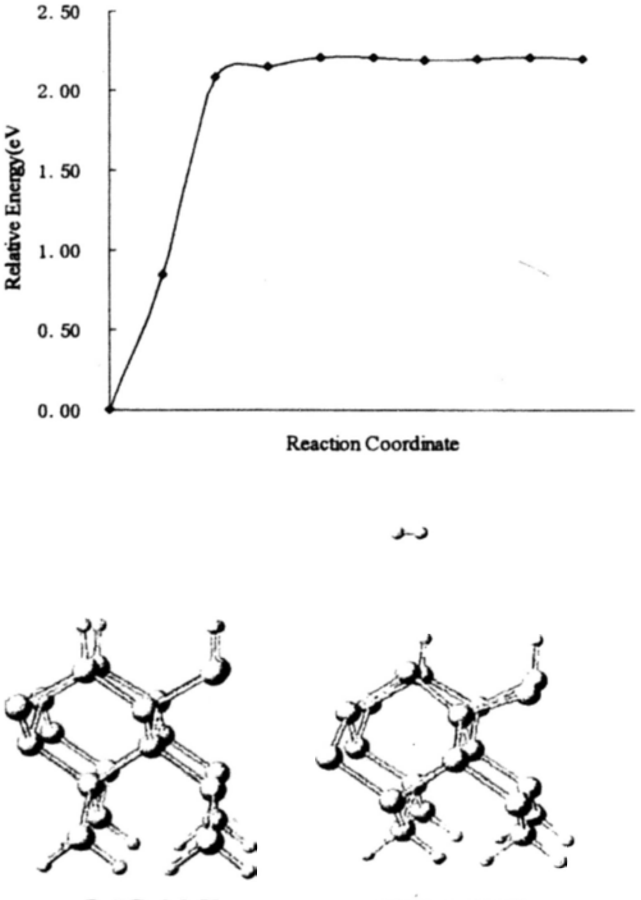

R (ΔE=0.0eV)   P (ΔE=2.20eV)

Figure 4.5 Desorption channel for 4H inter-dimer at high coverage (1.0ML). Two neighbor hydrogen atoms on different dimmers recombinatively desorbed with 2.0eV energy. There is no transition state can be found in this desorption channel, which is in consistent with the experimental measured low kinetic energy for the desorbed hydrogen molecule.

2H interdimer desorption shown in Figure 4.6 was the next desorption step following the 4H interdimer desorption. It had a desorption barrier of 1.92eV, and raised the energy by 1.72eV. Our calculated barrier was slightly larger than the value of 1.79eV reported by Shi *et al* [19].

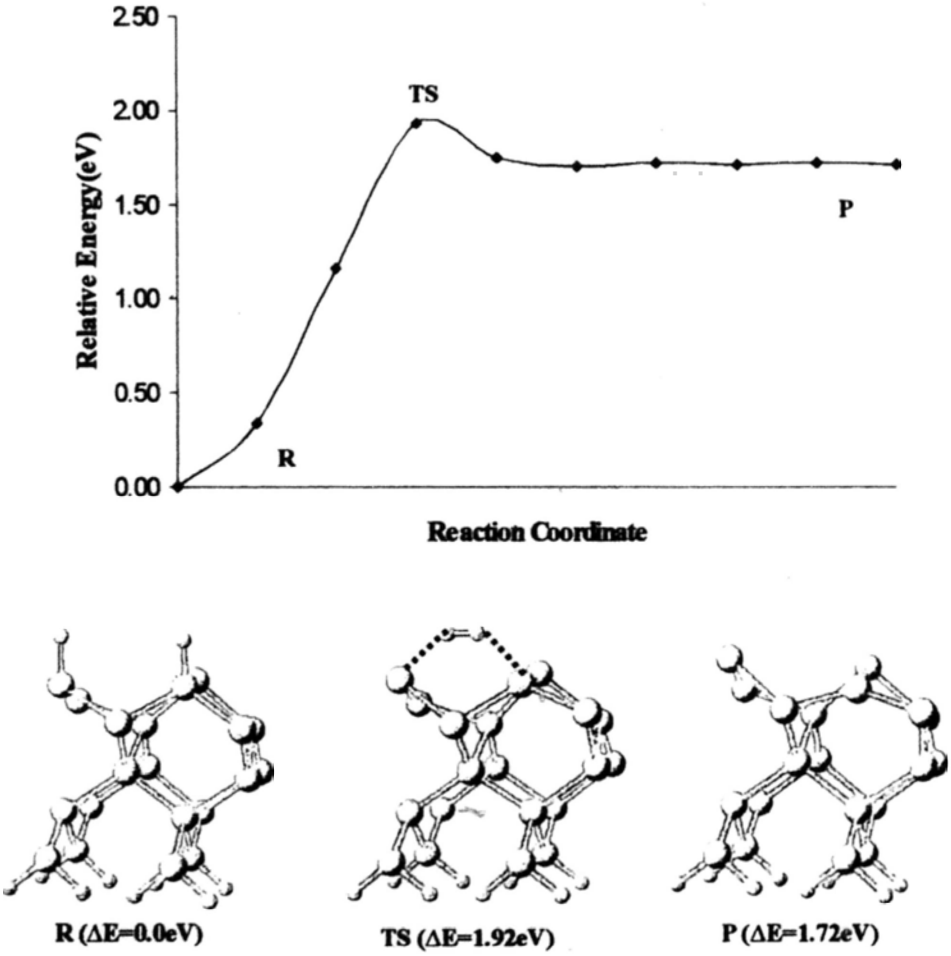

R (ΔE=0.0eV) TS (ΔE=1.92eV) P (ΔE=1.72eV)

Figure 4.6 Desorption channel for 2H inter-dimer at low coverage (0.5ML). This desorption is a concerted process with an activation barrier of 1.92ev and reaction heat of 1.72eV.

4.3.3 H diffusion on Si(100)

Several studies have been previously reported on the activation barrier for the diffusion of H-atom on Si(100)[37]. It was demonstrated that the diffusion barrier was much lower than desorption barriers, which were listed in Table 4.1 for comparison with our results. We found the hydrogen diffusion from 2H* to 2H as a stepwise reaction (see Figure 4.7). The first intra-row barrier was 1.68eV and the second intradimer barrier was 1.36eV. It can be seen that considerable heating was required for hydrogen diffusion although its barrier was lower than the desorption barriers. That's why hydrogen desorption on H/Si(100)-2×1 was a first order reaction. On metal surface, the H diffusion was much easier and H desorption was typically a second order reaction.

Table 4.1 Calculated barrier heights for hydrogen-atom diffusion.

Method	Barrier height(kcal/mol)		reference
	intradimer	intrarow	
GVB-CI-cluster	58	46	[38]
LDA-slab	30	30	[39]
BP-slab	32	32	[40]
Force field-slab	36	38	[41]
Becke3-LYP-cluster	43	55	[37]
This paper	31	39	This work

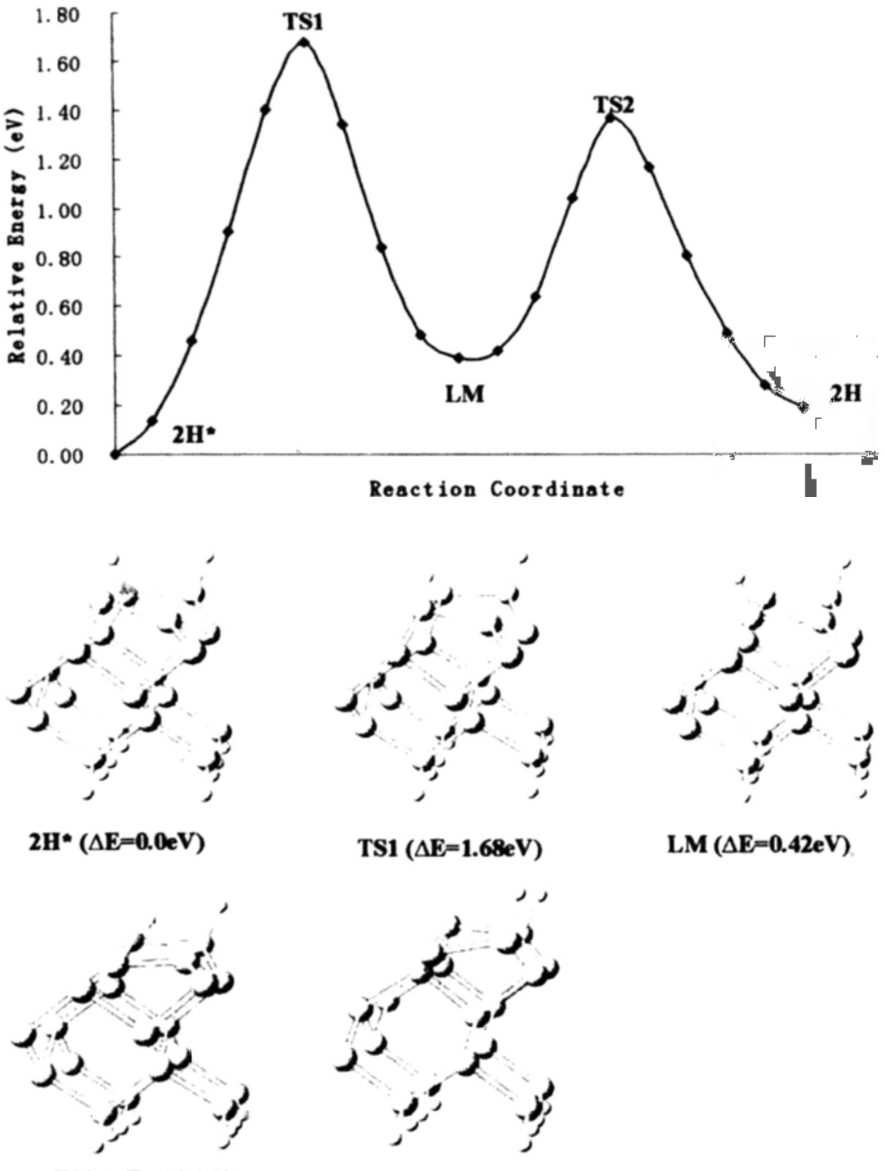

2H* (ΔE=0.0eV) TS1 (ΔE=1.68eV) LM (ΔE=0.42eV)

TS2 (ΔE=1.36eV) 2H (ΔE=0.19eV)

Figure 4.7 Process for hydrogen diffusion from 2H* to 2H. The diffusion process involves two activation barriers which are 1.68eV and 1.36eV respectively. Since the hydrogen desorption from 2H* intradimer channel needs an activation barrier of 2.32eV and desorption from 2H inter-dimer needs only 1.92eV, the hydrogen diffusion from 2H* to 2H is relatively easy to be occurred.

4.3.4 switching between monohydride and dihydride

Although the H/Si(100)-3×1 structure and the H/Si(100)-3×1→H/Si(100)-2×1 rearrangement have been identified by STM observations[12], the mechanistic details of such a transition is still not well understood. Here we provide such mechanistic description for the H/Si(100)-3×1→H/Si(100)-2×1 restructuring based on our first principles calculations. It involved two processes: the surface rearrangement from DMD (D for dihydride and M for monohydride) to DDM; and the hydrogen desorption from DD structure. The DMD→DDM rearrangement potential energy surface was shown in Figure 4.8, together with the geometries for transition, intermediate and product structures. The rearrangement process was a stepwise reaction. The first step was the breaking of the Si-Si bond of the monohydride dimer coupled with the formation of a Si-H-Si bridge structure, with an activation barrier of 1.34eV. The bridge intermediate could be further transformed to P by overcoming another barrier of 0.34eV. The calculated barrier was in consistent with the experimental measured barrier around 1.43eV[15]. And the identified intermediate has been observed by STM-tip induced atomic process. Irradiation of the H/Si(100)-3×1 surface with electrons from an STM tip induced hydrogen atom desorption and produced single dangling bonds, mostly at monohydride sites, in agreement with our calculations [42,44].

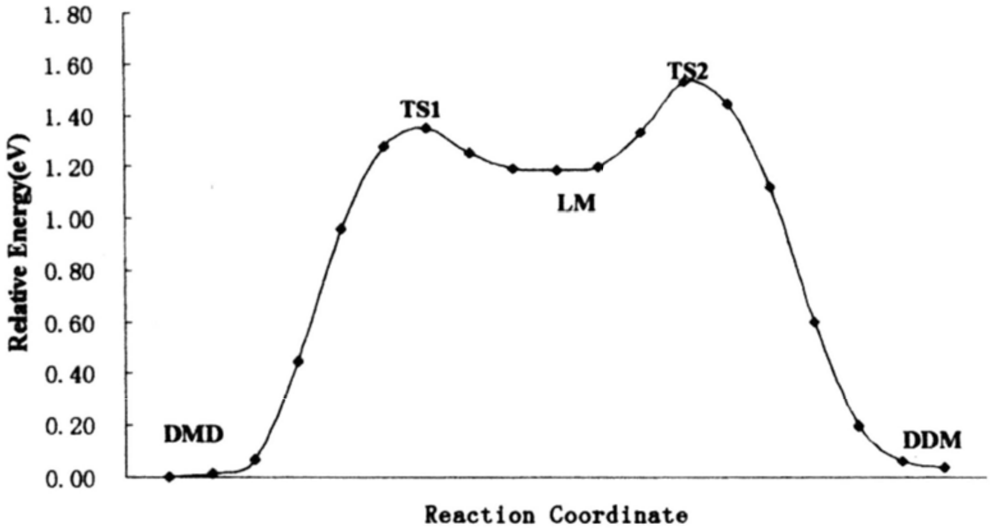

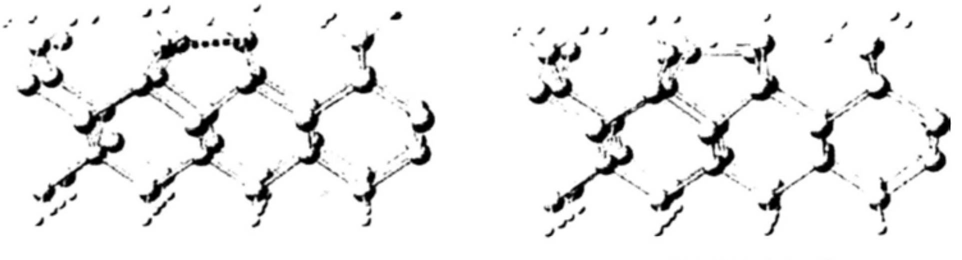

TS1 (ΔE=1.34eV) LM (ΔE=1.18eV)

TS2 (ΔE=1.52eV) DDM (ΔE=0.04eV)

Figure 4.8 Monohydride dihydride switching process on Si(100)-3×1 surface. One hydrogen atom in the M(monohydride) unit is first activated to the intermediate(LM) with an activation barrier of 1.34eV. The dangling bond in the LM can further interact with the neighbor dihydride(D) unit, forming the rearrangement product DDM by overcoming an activation about 0.34eV.

4.3.5 dihydride desorption

For hydrogen desorption from dihydride surface, 1,2-elimination and

1,1-elinimation mechanisms were proposed. Here we reexamined the two desorption mechanisms by calculating the potential energy surface (PES) curves for the two reaction paths. Figure 4.9 shows stepwise 1,1-elemination desorption pathway. In the first step, one hydrogen atom on the SiH_2 unit (doubly occupied Si atom) moves to a bridging position between the two neighboring Si atoms, elongating the Si-H bond and pushes the two hydrogen atoms (labeled in red) on the neighbor SiH_2 unit away from their original sites. After the two red hydrogen atoms were forced to be desorbed as hydrogen molecule, an intermediate labeled as LM was formed. This intermediate could be easily converted to the final product (monohydride) in the second step. The calculated total barrier for this desorption pathway was 1.84 eV, in agreement with the experimental value ~2.0 eV[21-22,24]. The total reaction is exothermic and the calculated energy released is 0.07eV.

1,2-recombinative desorption pathway was a concerted reaction and the calculated PES was shown in Figure 4.10. The calculated barrier was 2.35eV, which was 0.51eV higher than 1,1-elimination and kinetically less favorable.

Comparison between the two desorption mechanism indicated that it was the 1,1-elimination mechanism that plays role in the dihydride surface desorption. Our calculation results are in good agreement with Vittadini's[25]. And the most important is, the intermediate (bridge-structure) we identified in the dihydride surface desorption is similar to what we found in monohydride surface desorption. It is the first time that a common intermediate for monohydride and dihydride surface desorption has been reported.

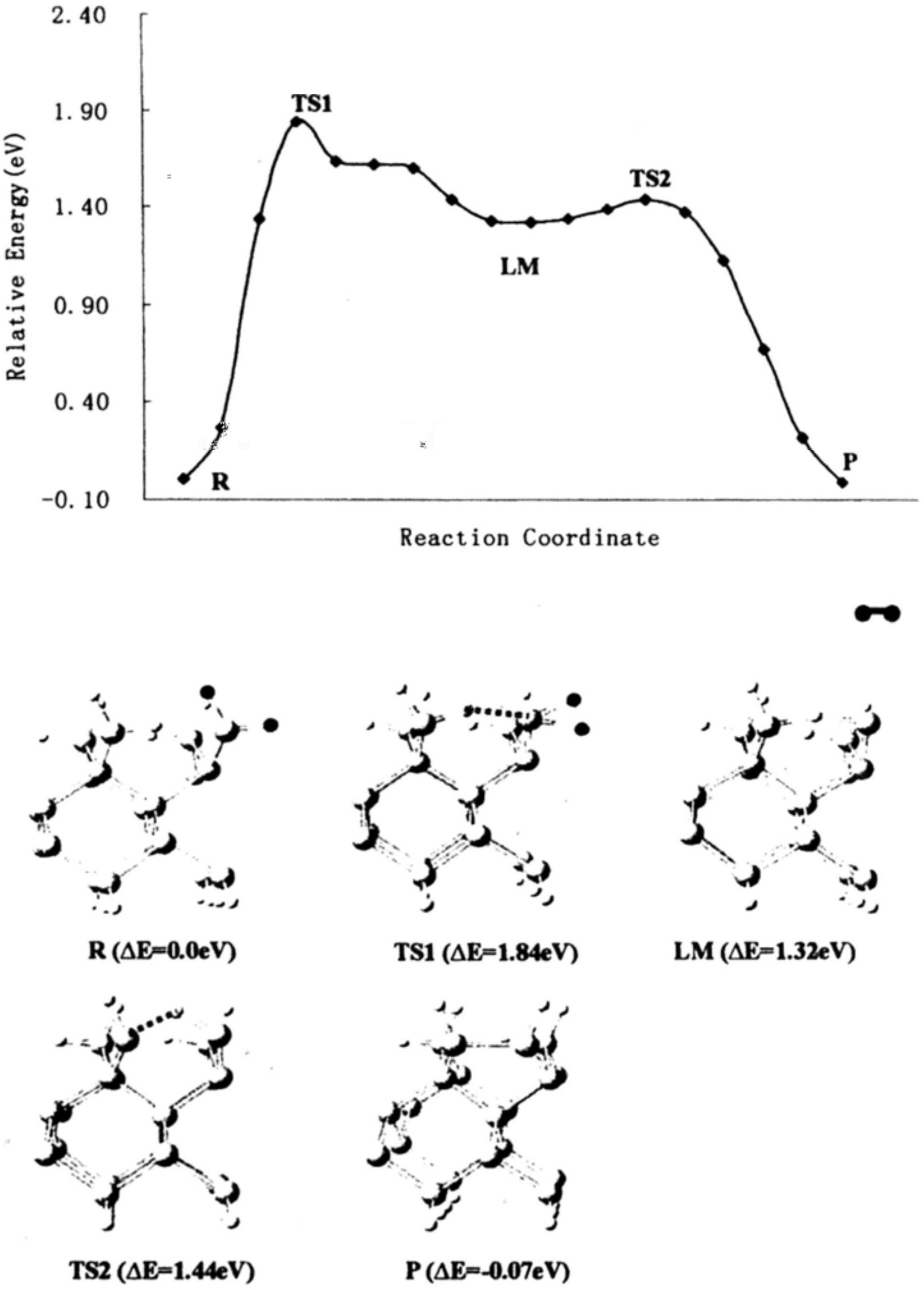

R (ΔE=0.0eV)
TS1 (ΔE=1.84eV)
LM (ΔE=1.32eV)
TS2 (ΔE=1.44eV)
P (ΔE=-0.07eV)

Figure 4.9 Stepwise desorption channel for hydrogen desorption from Si(100) -1×1 surface. In this channel, a hydrogen atom in one D unit approaches to the Si atom in neighbor D unit and drive the two hydrogen atoms in this unit to leave. Also an intermediate with single dangling bond is formed and this LM is easily transformed to the final product P because of the very low activation barrier.

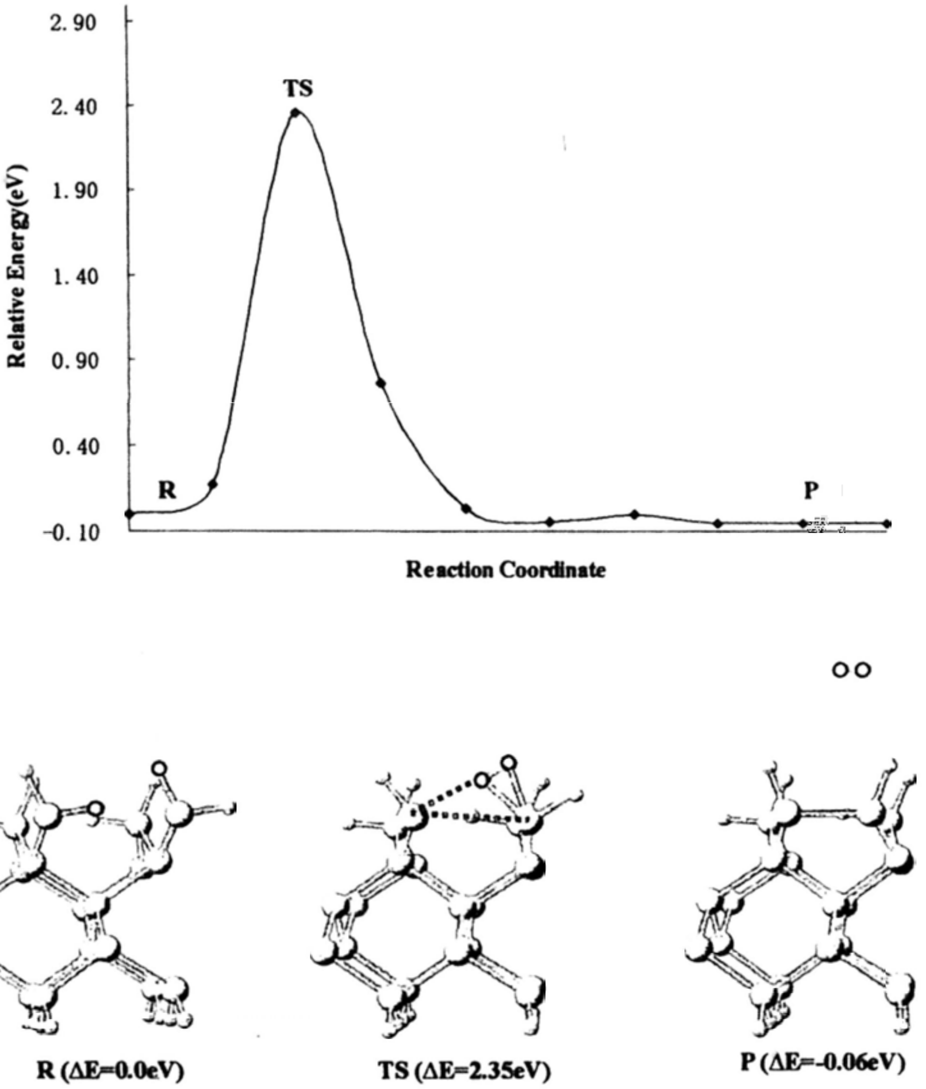

R (ΔE=0.0eV) TS (ΔE=2.35eV) P (ΔE=-0.06eV)

Figure 4.10 Concerted desorption channel for hydrogen desorption from Si(100)-1×1 surface. In this channel, each dihydride unit donates one hydrogen atom, going through a concerted transition state (labeled as TS) and finally get the product P. This desorption channel needs overcome an activation barrier about 2.35eV, which is 0.51eV higher than that of the first stepwise one.

4.3.6 Bonding analysis for the H bridge structure

Our calculations on hydrogen desorption from different H/Si(100) surfaces found a common intermediate which had a bridged H and dangling bond on one of the Si atom (see figure 4.11(c)). Such a bridge intermediate has been reported before, but its significance in hydrogen desorption has not been fully explored, and neither has its bonding nature been analyzed.

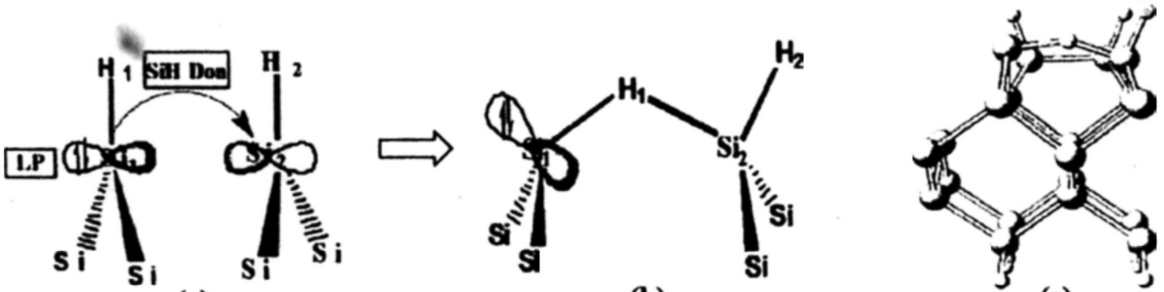

(a) (b) (c)

Figure 4.11 Bonding analysis for the formation of intermediate

To investigate the bonding characteristics of the intermediate, we did B3LYP/6-311++G(3df,2p) calculation on a Si_9H_{17} cluster, which served as a model for the H/Si(100)-2×1 surface dimer in a Natural Bonding Orbital (NBO) analysis.

Since the Si-H bond was stronger than the Si-Si σ bond, it was actually easier to break the Si-Si σ bond upon heating. Upon such an event, it was energetically more favorable to put the two electrons in this broken bond to one SiH, producing an ion pair $SiH^-\ldots SiH^+$ rather than a diradical $SiH\bullet\cdots SiH\bullet$ [43]. This process produced a lone pair on SiH^- and an empty p orbital on SiH^+. (see Figure 4.11(a)) Both a Si-H bonding orbital and the electron lone-pair on SiH^- (Si1-H1) can serve as donors to the empty p orbital on SiH^+ (Si2-H2) to lower the energy. Previous investigations found that stabilization came from the donor-acceptor interactions of Si-H→p was stronger than that of lone-pairs (lp) →p because the lone pair orbital had mainly s-character and hydrogen was more electronegative than Si[43]. The Si-H bonds were better donors than the lone-pair. Therefore, the Si1-H1 donor orbital and the empty p orbital of the Si2H2 fragment were tilted toward each other, and at the same time the

H2 atom in Si2H2 moved away from the bridging hydrogen atom, which led to the bridge structure shown in Figure 4.11(b).

Our NBO analysis indicated that there was an electron lone-pair on Si1-H1, which had its main contribution from the 3s orbital of Si1. For Si2, two types of bonds were found: a typical covalent bond Si2-H2 and a dative bond Si2-H1 with a Wiberg bond index of 0.6, in agreement with our expectation.

It is therefore not surprising that the bridge structure is often found in the desorption paths identified, both in previous study and in our current report. They could be formed at a temperature lower than that required to trigger the desorption of hydrogen.

The special electronic structure has already been found in some small hydrogenated silicon clusters. Calculations show that Si_2H_2 gas molecule has several unusual equilibrium geometries as shown in scheme 1[43]. The doubly bridged structure A and singly bridged structure B are more stable than the linear structure E, demonstrating the possibility of our identified intermediate.

Scheme 1

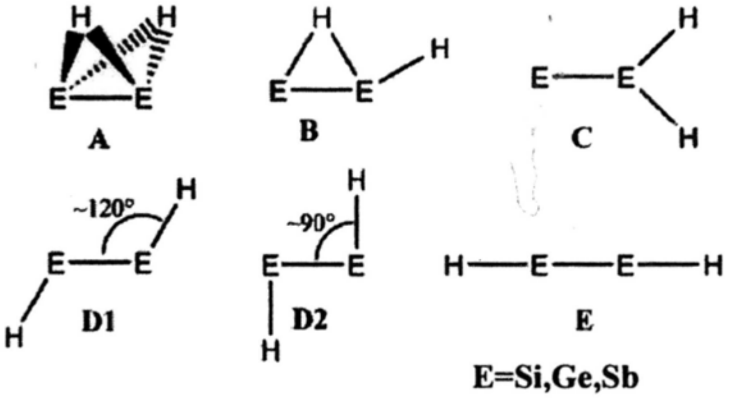

***data copy from reference [43]**

4.3.7 Comparison with experiments

The atomic-scale desorption of hydrogen atoms from the H/Si(001)-(2 × 1) surface using the tip of STM as an atomic size electron source has attracted considerable interest in recent years[44-57]. It has been demonstrated that, by generating strong electric fields using voltage pulses, bonds can be broken with the STM[44-45,52-57]. When the energy of the incident electrons in the STM tip exceeds the threshold of Si-H bond electronic excitation (~6 eV), an single electron is excited from the bonding Si-H σ bonding to the corresponding antibonding σ* orbital and thus leading to local bond-breaking[44-45,52-54]. The desorption yield is ~2.4×10^{-6} H-atoms/electron and is independent of the current. More interestingly, excitation of the Si-H bond with electron energies below the electronic excitation threshold and even below the Si-H bond strength (~3eV) can still lead to H desorption[44,52-53]. The yield, however, is several orders of magnitude lower than that produced by electronic excitation and is a strong function of the tunneling current. The observation has been attributed to the desorption mechanism which involves multiple-vibrational excitation of the Si-H species through inelastic tunneling[42,44,58-59]. However, several studies have reported significantly different results[44,48,53], leaving the local-field effects on the inelastic process unclear. Here we proposed a new mechanism to explain the H desorption below the threshold energy.

According to bonding analysis described in section 4.3.6, the H bridged intermediate has a single dangling bond, which is similar to Si-H bond broken structure. We did STM images simulations for the two structures and the calculated results demonstrated that there was little difference between the two simulated STM images, as shown in Figure 4.12. And what's more, the formation of the H bridged intermediate has a barrier of only ~1.5 eV (see Figure 4.3), which is much lower than the Si-H bond strength (3 eV). When the sample bias voltage is applied to a specific Si-H bond, the $(SiH)_2$ dimer is expected to be excited to H bridged intermediate with a single dangling bond. It has been found that single dangling bonds induced by STM tip can be observed at a sample bias of +2.5 V with the tunneling current of 10 nÅ. Previous studies[44-45,52-54] suggested these single dangling bonds were resulted from the Si-H bond breaking, however, we thought that these single dangling bonds were caused by the formation of H bridged structure. Reasons for our arguments will be introduced in the following paragraphs.

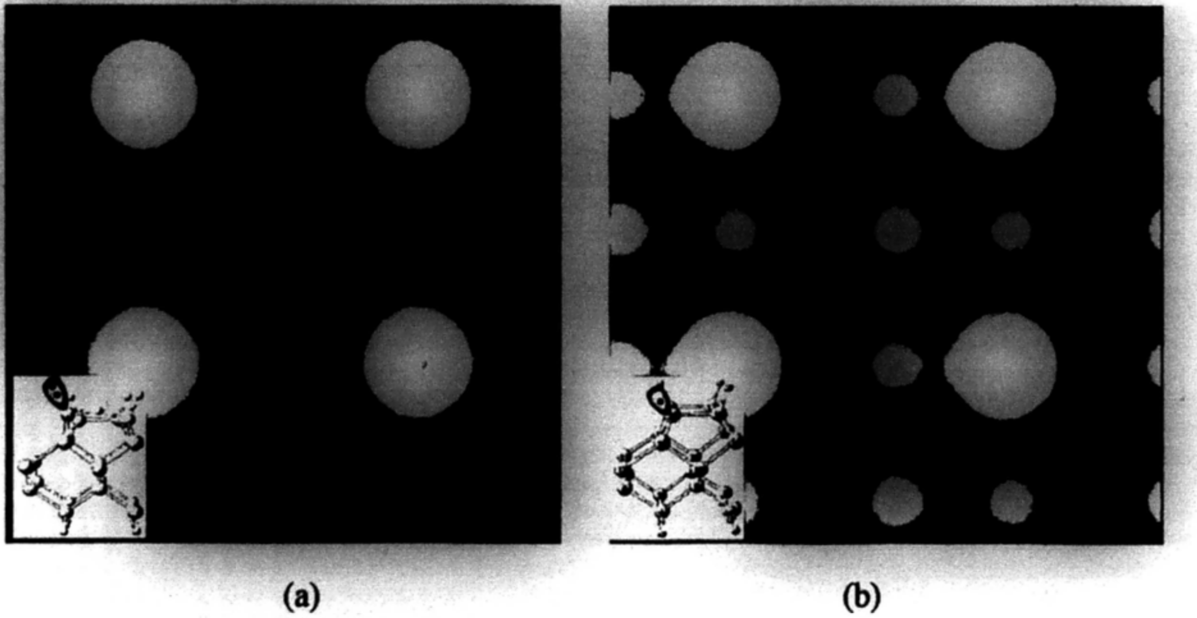
(a) (b)

Figure 4.12 Simulated STM images of electron filled states at -2.0 eV below Fermi surface for (a) H-bridged structure, (b) Si-H bond broken structure. The insets show the corresponding electronic structures.

Firstly, the barrier for the formation of H bridged intermediate is very low (~1.5eV). When the energy of the incident electrons in the STM tip is below the threshold, $\sigma \rightarrow \sigma^*$ excitation is hard to occur but H bridged structure can be easily formed. Although the intermediate is also easily to revert to its initial state, the continuous excitation from the STM tip can assure the probability of existence. The single dangling bonds had been observed when sample bias voltage was at +3V[52] and +2.5V[44,53].

Secondly, site selectivity was detected in the desorption of H from H/Si(100)-(3×1) surface[42]. H/Si(100)-(3×1) surface has alternative rows of monohydride (SiH) and dihydride (SiH_2) units. In case of high e-beam current density, all H is desorbed and the system reverts to the Si(100)-(2×1) structure. If the current density is low, the selectivity of individual H desorption events can easily be seen. Examination of the location of the H desorption-produced dangling bonds showed that they were all located on top of monohydride units[42]. If the single dangling bonds are caused by the bond broken of Si-H bond, there should be equal probability to observe single dangling bonds on both monohydride sites and dihydride sites[60]. Moreover, since thermal desorption of H_2 has a lower desorption temperature from the dihydride[15], it is strange that H desorption by vibrational excitation has the opposite site-selectivity from that of thermal desorption. The formation of H bridged structure can explain this site-selectivity very well because such bridge structure can be formed only at monohydride sites. Here, for the first time we provided a quite good explanation for this site-selectivity. Moreover, according to our mechanism, H desorption below threshold energy is hard to occur on H/Si(111) surface due to the absence of $(SiH)_2$ dimer. In experiment, desorption on H/Si(111) surface was only found to occur at electron energies higher than ~6 eV, and the desorption was attributed to the electronic excitation of the Si-H bond[61-62]. This observation further supported that H desorption below threshold energy was through the H bridged intermediate.

Thirdly, experiments found that the H desorption yield below threshold energy is temperature dependent. A cryogenic UHV scanning tunneling microscope has been used to study the electron stimulated desorption of hydrogen and deuterium from Si(100) surfaces at 11 K[42]. Above ~5 eV, desorption yields for H and D are temperature independent, and strong isotope effect is observed, as seen previously at room temperature. In contrast, a very strong temperature effect was observed in the energy regime below 4 eV, where hydrogen was a factor of ~300 easier to desorb at 11K than at 300 K. Furthermore, at 11 K, deuterium could also be observed to desrob in the low energy regime, which could not be achieved at 300 K. This large temperature dependence had been explained by a model that involved multiple vibrational excitation and took into account the increase of the Si-H vibrational lifetime at low temperature[42]. According to our arguments, the yield of the H bridged intermediate is responsible for the observed "H desorption" yield. The yield of the H bridged intermediate is actually controlled by the lifetime of the intermediate, and the lifetime is determined by the balance of the formation rate and reversion rate. At high temperature (300K), the reversion rate is high due to the relatively low reversion barrier(~0.1eV), thus the lifetime of the intermediate is short, resulting into the low "H desorption" yield. But at low temperature (11K), the reversion rate becomes slower and the lifetime of the intermediate becomes longer, resulting into a higher "H desorption" yield. So, we attributed the increase of desorption yield to the increase of lifetime for the H bridged intermediate at low temperature, while references[39-43,52] took into account the increase of the Si-H vibrational lifetime.

There is also the question that under what kind of conditions could this bridge intermediate lead to desorption? In other words, could the intradimer desorption pathway through the bridge intermediate play a role? Our calculations demonstrated that intradimer desorption pathway was a stepwise reaction, and two sequential excitations were needed to desorb one hydrogen molecule. On the other hand, the energy barrier of each step was significantly less (1.50eV and 1.10eV respectively) than the barrier for the 4H interdimer path (2.2eV). When the surface was excited with high density electron current and multiple excitations became possible, the intradimer desorption path should be accessible. Such experimental results have been reported in previous studies[44,52]. Figure 4.13 listed the STM image of Si dangling bonds written at different basis voltage, which is carried out by Avouris in 1996[52]. From the two figures, we can clearly see that at high sample bias voltage and low current(Figure 4.13(a)), only single dangling bonds can be observed. While at low sample bias voltage and high current (Figure 4.13(b)), double dangling bonds on Si dimer can be also observed except for the single dangling bonds, demonstrating the intra-dimer desorption process. Similar experimental results have also been observed by Shen et al. in 1995[44].

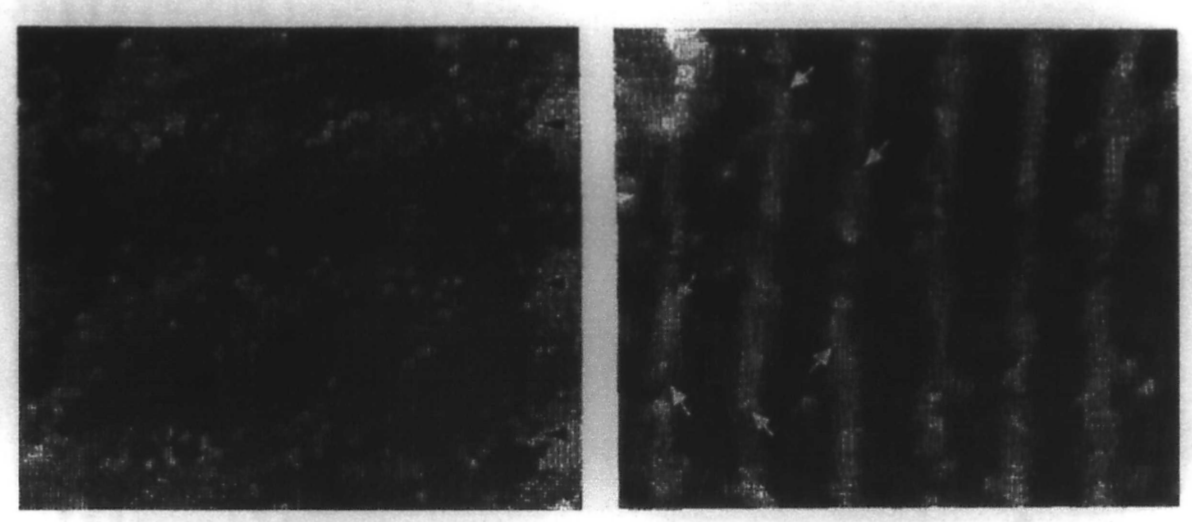
(a) (b)

Figure 4.13 STM image of a pattern of Si dangling-bond lines, written at a sample bias voltage of (a) Vs = + 8 V and a current of I = 0.01 nA. The line dose was kept low, Q = 1 × 10^{-6} C.cm^{-1}, so that individual dangling-bonds can be clearly seen. (b) Vs = + 3 V and a current of I = 4.5 nA. The electron line dose was Q=6 × 10^{-4} C.cm^{-1}. The arrows point to some of the areas where both H atoms in a Si dimer have been desorbed. Data copy from reference [51].

The meta-stable intermediate can also explain the isotope effect for desorption induced by STM tip. The isotope effect for desorption by STM tip has been found to be related with the sample bias voltage[45]. When the energy of the incident electrons was above the threshold energy for electronic exication, $\sigma \rightarrow \sigma^*$ excitation leads to H-desorption[44]. It was found that substitution of H by D led to a decrease of desorption yield by a factor of 50. This large isotope effect was shown to arise from the existence of efficient excitation-quenching channels and the influence of the mass of the atom on the excited state dynamics[42]. When the energy of the incoming electrons was below the threshold and the current was sufficiently high, H-desorption could still be observed and desorption rate was strongly dependent on the tunneling current.

Previous studies[42,44,58-59] suggested that multiple-vibrational excitations of the Si-H bond accounted for the desorption, and the isotope effect was caused by the different vibrational lifetime of Si-H and Si-D. It was assumed that the adsorbate vibrations is excited by inelastic tunneling electron and these vibrational energies were deposited in the vibration mode of the Si–H(D) bond. The Si-H(D) bond was expected to be broken when the stored energy was enough to desorb H atom. So the vibrational lifetime plays a critical role in this heating mechanism. However, our calculations demonstrated that a meta-stable intermediate was formed at energies below threshold and this intermediate could be further excited to desorb H_2 molecule by adsorbing another electron. Since multiple electron excitation is possible under the high current density, H_2 desorption through intra-dimer mechanism has probability. The observed bright spots on STM image can be classified as single dangling bonds and double dangling bonds, which we assigned them as H bridged intermediate and Si dimer respectively. Thus the isotope effect for desorption below threshold energy can be divided as isotope effect from H desorption and isotope effect from H_2 desorption. For H desorption isotope effect, kinetic isotope effect is important, for example, the thermal activation barrier for deuterium is higher than hydrogen due to its lower zero-point energy. This is confirmed by the observed dependence of the desorption yield on temperature[42]. For H_2 desorption isotope effect, the lifetime of the intermediate plays a big role. H bridged intermediate and

D bridged intermediate have different lifetime, resulting to isotope effect for $H_2(D_2)$ desorption.

4.4 Conclusion

Hydrogen desorption mechanisms on H/Si(100)-1×1, H/Si(100)-2×1, H/Si(100)-3×1 surfaces have been explored by theoretical calculations with slab model. The three surfaces have similar desorption mechanisms and the calculated barriers coincide with experimental values. Moreover, a common intermediate has been identified on the three surfaces. Using this intermediate, we explained very well some experimental results which are caused by STM tip-induced desorption. And we provided another point of view to understand the STM tip-induced desorption.

4.5 Reference

[1] Ciraci S.; Batra I. P. *Surf. Sci.* **1986**, 178, 80.

[2] Shane S. F.; Kolasinski K.W.; Zare R. N. *J. Chem. Phys.* **1992**, 97, 1520.

[3] Boland J. J. *Adv. Phys.* **1993**, 42, 129.

[4] Waltenburg H. N.; Yates J. T. *Chem. Rev.* **1995**, 95, 1589.

[5] Dürr M.; Hu Z.; Biedermann A.; Höfer U.; Heinz T. F., *Phys. Rev. Lett.* **2002, 88,** 046104.

[6] Boland J. J. *Phys. Rev. B.* **1991**, 44, 1383.

[7] Doren D.J. *Adv. Chem. Phys.* **1996**, 95, 1.

[8] Oura K.; Lifshits V. G; Saranin A.A.; Zotov A.V.; Katayama M. *Surf. Sci. Rep.*

1999, 35, 1.

[9] Cheng C.C ; Yates J.T. Jr. ; Phys. Rev. B. **1991**, 43, 4041 ; Kolasinski K.W.; et al. *Phys. Rev. Lett.* **1994**, 72, 1356.

[10] Gross A.; Bockstedte M.; Scheffler M. *Phys. Rev. Lett.* **1997**, 79, 701.

[11] Law J.T. *J. Chem. Phys.* **1959**, 30, 1568.

[12] Feng S.-S.; Lin C.-T.; Yang K.-M.; Lin D.-S.; Chiang T.-C. *Phys. Rev. Lett.* **2005**, 94, 196103.

[13] Dürr M.; Höfer U. *J. Chem. Phys.* **2004**, 121, 8058.

[14] Namiki A. *Progr. Surf. Sci.* **2006, 8**1, 337.

[15] Nachtigall P.; Jordana K. D. *J. Chem. Phys.* **1994**, 101, 8073.

[16] Brenig W.; Pehlke E. *Progr. Surf. Sci.* **2008**, 83, 263.

[17] Pehlke E. Phys. Rev. B, **2000,** 62, 12932.

[18] Okamoto Y. *J. Phys. Chem. B* **2002**, 106, 570.

[19] Shi J.; Chuan Kang H. *J. Chem. Phys.* **2005**, 123, 034701.

[20] Shane S. F.; Kolasinski K. W.; Zare R. N. *J. Chem. Phys.* **1992**, 97, 3704.

[21] Flowers M.C.; Jonathan N.B.H.; Liu Y.; Morris A. *J. Chem. Phys.* **1993**, 99, 7038.

[22] Ning B.M.H.; Crowell J.E. *Surface Sci.* **1993**, 295, 99.

[23] Gupta P.; Colvin V. L., George S. M. *Phys. Rev. B* **1988**, 37, 8234.

[24] Niida T.; Tsurumaki H.; Namiki A. *J. Chem. Phys.* **2006**, 124, 024715.

[25] Vittadini A.; Selloni A. *Chem. Phys. Lett.* **1995,** 235, 334.

[26] Fan X. L., Zhang Y. F., Lau W. M., Liu Z. F. *Phys. Rev. B* 2005, 72, 165035.

[27] Zhang Q.J.; Fan X.L.; Lau W.M.; Liu Z.F. *Phys. Rev. B* 2009, 79, 195303.

[28] Zhang Q.J.; Wang J.L.; Liu Z.F. *J. Phys. Chem. C.* **2007**, 111, 6365.

[29] Jónsson, H. *Annu. Rev. Phys. Chem.* **2000**, 51, 623-653.

[30] Henkelman, G.; Uberuaga, B. P.; Jónsson, H. *J. Chem. Phys.* **2000**, 113, 9901.

[31] Henkelman, G.; Jónsson, H. *J. Chem. Phys.* **2000**, 113, 9978.

[32] Filippi C. *Phys. Rew. Lett.* **2002, 89**, 16602.

[33] Kanai Y.; Tilocca A.; Seloni A.; Car R. *J. Chem. Phys.* **2004**, 121, 3359.

[34] Kratzer P.; Hammer B.; Nøskov J.K. *Phys. Rev. B* **1995**, 51, 13432.;

[35] Kratzer P.; Hammer B.; Nøskov J.K. *Chem. Phys. Lett.* **1994**, 229, 645.

[36] Pehlke E.; Scheffler M. *Phys. Rev. Lett.* **1995**, 74, 952.

[37] Nachtigall P.; Jordan K. D. *J. Chem. Phys.* **1995**, 102, 8249

[38] Wu C. J.; Carter E. A. *Phys. Rev. B.* **1992**, 46, 4651.

[39] Vittadini A.; Selloni A.; Casarin M. *Surf. Sci. Lett.* **1993**, 289, L625.

[40] Vittadini A.; Selloni A.; Casarin M. in *Proceedings of the 4th International Conference on the Formation of Semiconductor Interfaces*, edited by Langer B.; Lueth H.; Moeuch W.; Pollmann J. World Scientific, Singapore, **1994**, 146.

[41] Wu C. J.; Ionova I. V.; Carter E. A. *Phys. Rev. B* **1994**, 49, 13488.

[42] Avouris P.; Walkup R.E.; Rossi A.R.; Shen T.-C.; Abeln G.C.; Tucker J.R.; Lyding J.W. *Chem. Phys. Lett.* **1996**, 257, 148.

[43] Matthias L.; Andreas K.; Gernot F.; *J. Am. Chem. Soc.* **2005**, 127, 6290

[44] Shen T.-C.; Wang C.; Abeln G.C.; Tucker J.R.; Lyding J.W.; Avouris Ph.; Walkup R.E. *Science.* **1995**, 268, 1590.

[45] Shen T.-C. , Avouris P., *Surf. Sci.* **1997,** 390, 35-44

[46] Foley E. T.; Kam A. F.; Lyding J. W.; *Phys. Rev. Lett.* **1998,** 80, 1336.

[47] Thirstrup C.; Sakurai M.; Nakayama T.; Aono M.; *Surf. Sci,* **1998**, 411, 203.

[48] Stokbro K.; Ben Yu-Kuang Hu; Thirstrup C.; Xie X. C. *Phys. Rev. B* **1998**, 58, 8038.; *Phys. Rev. Lett.* **1998,** 80, 2618.

[49] Thirstrup C.; Sakurai M.; Nakayama T.; Strokbro K. *Surf. Sci.* **1999**, 424, L329.

[50] Doumergue P.; Pizzagalli L.; Joachim C.; Altibelli A.; Baratoff A. *Phys. Rev. B* **1999**, 59, 15910.

[51] Sakurai M., Thirstrup C.; Aono M. *Phys. Rev. B* **2000**, 62, 16167.

[52] Avouris Ph.; Walkup R.E.; Rossi A.R. et al. *Surf. Sci.* **1996**, 363, 368

[53] Soukiassian L.; Mayne A.J.; Carbone M.; Dujardin G. *Phys. Rev. B* **2003**, 68, 035303.

[54] Persson B.N.J.; Avouris Ph. *Surf. Sci,* **1997**, 390, 45.

[55] Shen T.C.; Steckel J.A.; Jordan K.D. *Surf. Sci.* **2000**, 446, 211

[56] Lyo I.-W.; Avouris Ph. *Science* **1991**, 253, 173; *Appl. Surf. Sci.* **1992**, 60/61, 426.

[57] Kobayashi A.; Grey F.; Snyder E.; Aono M. *Phys. Rev. B* **1994**, 49, 8067.

[58] Persson B.N.J.; Avouris Ph. *Chem. Phys. Lett.* **1995**, 242, 483.

[59] Chen Z.; Ong P.; Mylin A.K.; Singh V.; *Appl. Phys. Lett.* **2002**, 81, 3278

[60] Chabal Y.J.; Ragavachari K. *Phys. Rev. Lett.* **1985**, 54, 1055.

[61] Becker R.S.; Higashi G.S.; Chabal Y.J.; Becker A.J. *Phys. Rev. Lett.* **1990**, 65, 1917.

[62] Wintterlin J.; Avouris Ph. *J. Chem. Phys.* **1994**, 100, 687.